Overlapping Domain Decomposition Preconditioners for Multi-Phase Elastic Composites

Fraunhofer
ITWM

TECHNISCHE UNIVERSITÄT KAISERSLAUTERN

Dipl. Math. Marco Buck

Vom Fachbereich Mathematik der
Technischen Universität Kaiserslautern
zur Verleihung des akademischen Grades
Doktor der Naturwissenschaften
(Doctor rerum naturalium, Dr. rer. nat.)
genehmigte Dissertation

Datum der Disputation:
14. Juni 2013

1. Gutachter: Prof. Dr. Oleg Iliev,
2. Gutachter: Priv. Doz. Dr. Johannes K. Kraus

D 386

Abstract

The application behind the subject of this thesis are multiscale simulations on highly heterogeneous particle-reinforced composites with large jumps in their material coefficients. Such simulations are used, e.g., for the prediction of elastic properties. As the underlying microstructures have very complex geometries, a discretization by means of finite elements typically involves very fine resolved meshes. The latter results in discretized linear systems of more than 10^8 unknowns which need to be solved efficiently. However, the variation of the material coefficients even on very small scales reveals the failure of most available methods when solving the arising linear systems. While for scalar elliptic problems of multiscale character, robust domain decomposition methods are developed, their extension and application to 3D elasticity problems needs to be further established.

The focus of the thesis lies in the development and analysis of robust overlapping domain decomposition methods for multiscale problems in linear elasticity. The method combines corrections on local subdomains with a global correction on a coarser grid. As the robustness of the overall method is mainly determined by how well small scale features of the solution can be captured on the coarser grid levels, robust multiscale coarsening strategies need to be developed which properly transfer information between fine and coarse grids.

We carry out a detailed and novel analysis of two-level overlapping domain decomposition methods for the elasticity problems. The study also provides a concept for the construction of multiscale coarsening strategies to robustly solve the discretized linear systems, i.e. with iteration numbers independent of variations in the Young's modulus and the Poisson ratio of the underlying composite. The theory also captures anisotropic elasticity problems and allows applications to multi-phase elastic materials with non-isotropic constituents in two and three spatial dimensions. Moreover, we develop and construct new multiscale coarsening strategies and show why they should be preferred over standard ones on several model problems. In a parallel implementation (MPI) of the developed methods, we present applications to real composites and robustly solve discretized systems of more than 200 million unknowns.

Acknowledgements

Contents

CONTENTS

1

Introduction

1.1 Subject of the Thesis

Constantly growing demands on the range of application of todays industrial products require more and more frequently the development of innovative, highly-effective composite materials, specifically adapted to their field of application. To substantially reduce costs and time for the construction of prototypes and performing measurements on their properties, virtual material design provides essential support in the development process of new materials. Of special interest is the multiscale-analysis of particle reinforced composites as they combine positive features of their constituents such as e.g. light weight and high stiffness (e.g. nano-reinforced composites [38, 60]).

The composites typically enclose multiscale properties with highly oscillating material coefficients on multiple scales. Resolving the heterogeneities in the multi-phase composites on the finest scale when performing material simulations on the microstructures requires meshes with very fine resolutions and hence, it is of high computational cost. The structures are either obtained from microscale computed tomography (CT) images of real composites or they are virtually designed using GeoDict [43] as a tool to computer generate 3D-microstructure models based on macroscopic material parameters. Since the computational domain covers an excerpt of the microstructure which may originate from computed tomographies, Ω typically takes the form of a cuboidal domain (see e.g. Figure 1.1).

The system of partial differential equations (PDEs) in linear elasticity which governs the displacement field $\boldsymbol{u}$ of a body deformed under volume forces $\boldsymbol{f}$ reads for an isotropic

1. INTRODUCTION
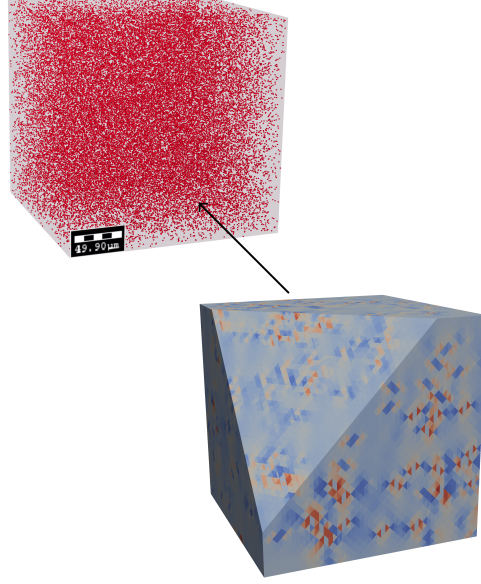
Figure 1.1: Composite material; matrix material (grey) and small inclusions (red); elastic strains computed at a portion of the overall composite

and homogeneous material in Ω,

$$\mu\Delta\boldsymbol{u} + (\lambda + \mu)\nabla(\nabla \cdot \boldsymbol{u}) = \boldsymbol{f},$$

where λ and μ are the Lamé parameters of the isotropic material. To find an approximate solution $\boldsymbol{u}^h$ of the PDE system, a finite element (FE) discretization on a regular mesh with mesh parameter h in three spatial dimensions is introduced. Using a discretization on Ω with vector-valued piecewise linear elements on a triangular mesh results in a sparse symmetric positive definite linear system $A\mathbf{u} = \mathbf{f}$ (cf. equation (2.1) and section 2.2.3 for more details). The linear system is in general very large and its solution cannot be computed using a direct solver, an iterative method needs to be applied. When solving the linear system iteratively, the number of iterations required to compute the solution $\boldsymbol{u}^h$ up to a predefined accuracy strictly depends on the condition number of the matrix A. An upper bound for the condition number of the arising linear system can be estimated to

$$\kappa(A) \leq C \sup_{x,y\in\Omega} \frac{\mu(x) + \lambda(x)}{\mu(y)} h^{-2}, \tag{1.1}$$

where λ and μ are the material parameters of the constituents of the composite. The constant C is independent of h, λ and μ and the coefficients typically contain large jumps within Ω (see e.g. Figure 1.1). As we are interested in analysing compressible materials, we may assume that $\lambda \ll \infty$. Performing simulations on these heterogeneous materials faces two important challenges, namely

(i) Local effects of the microstructures have an enormous effect to the materials overall behaviour (e.g. the stress concentration on material interfaces which may cause fracture) and need to be captured accurately. The latter requires to resolve the heterogeneities in the composite on the finest scale, which introduces very fine meshes with small mesh parameter h.

(ii) The multiscale character of the elastic composites introduces large jumps in the material parameters on multiple scales. In most applications, λ and μ vary over up to 9 orders of magnitude (e.g. nano-composites in [38, 60, 96]).

According to (i), (ii) and the bound in (1.1), the resulting linear system is in general very ill-conditioned. It requires preconditioners which, roughly speaking, remove the ill-conditioning due to mesh parameters and variations in the material coefficients.

In the scope of this thesis, we analyse and develop two-level overlapping domain decomposition preconditioners for the highly heterogeneous multiscale problems. The method introduces a set of overlapping subdomains which form a covering of the computational domain and a coarse mesh $\mathcal{T}_H$. It combines local corrections on the subdomains with a global correction on a coarse space spanned by a set of well-selected basis functions. The robustness of the overall method is mainly determined by the quality of the coarse basis. It is the goal of the thesis to (a) develop and apply two-level overlapping domain decomposition preconditioners which are robust w.r.t. the jumps in the material coefficients in the PDE as well as (b) their detailed analysis and the specification of robustness-measures which can be used to predict the quality of the coarse space and the overall method. Based on such measures, we develop coarsening strategies for the construction of robust coarse spaces in the context of the overlapping domain decomposition preconditioners. One of the main challenges is that coefficient variations appear on a very small scale such that they cannot be resolved by or aligned with a coarse grid. This circumstance requires the construction of coarse spaces of multiscale character which capture the small scale features of the specific heterogeneous problem.

1.2 State Of the Art

In this section, we give an overview of state of the art methods available in the context of solving and preconditioning the discrete linear elasticity systems. Beyond current developments in domain decomposition methods for scalar elliptic PDEs, we also provide a short overview of multigrid and multilevel methods and point out challenges when applying them to elasticity problems. Furthermore, we address the origin of multiscale methods and as well as their application in the development of robust preconditioners.

The common ground of efficient iterative solution methods for the linear systems which arise from a finite element discretization of PDEs is that the majority of their computation is performed on (grid-) levels coarser than the fine discretization. These methods can typically be assigned to the groups of (i) multigrid or multilevel methods (see e.g. [49, 80, 102]) or (ii) domain decomposition methods (see e.g. [79, 97]). For scalar elliptic PDEs but also for the elasticity system, such methods are developed and successfully applied to problems with varying PDE coefficients. Specifically, provided that the coefficient variations can be resolved by the coarse(st) grid, they allow a robust computation with iteration numbers independent of the PDE coefficients.

Classical algebraic multigrid methods (AMG) have been introduced for scalar elliptic PDEs in [10, 11, 12]. The coarser levels are constructed by considering exclusively the entries of the stiffness matrix itself. The interpolation operators - which transfer information between fine and coarse grids - are constructed such that the kernel of the differential operator is spanned by the basis functions on coarser levels. Since for scalar elliptic problems the kernel consists of constant functions, they can easily be preserved on coarser grids by constructing the coarse basis functions such that they sum up to one at any fine grid node. The increased kernel of the elasticity operator, which contains the set of *rigid body modes*, leads to one of the main difficulties when applying multigrid methods to linear elasticity problems. The dimension of the kernel is here larger than the spatial dimension of the underlying problem, additional information is required to ensure that the coarse basis functions preserve the rigid body rotations. Particularly, purely algebraic multigrid methods which require only the stiffness matrix as input may loose robustness when applied to elasticity problems. For such methods, however, the set of rigid body modes can often be provided as additional input. A detailed overview of classical algebraic multigrid methods and potential remedies for the

applications to elasticity problems are deeply discussed in [23], [6] and the references therein, and partially also in [104].

Another class of algebraic multigrid methods are **aggregation-based methods**. Aggregation methods were originally introduced in [99, 100] for scalar elliptic PDEs and first applied to the linear elasticity system in [101]. The method requires initially the stiffness matrix as well as the vectors which represent the rigid body modes in terms of the basis functions on the fine mesh. Then, aggregates are formed, i.e. non-overlapping unions of fine grid nodes. For any aggregate, the union of fine elements which touches at least one of the aggregates' nodes determines the support of a coarse basis function. The coarse basis functions can then be constructed by simply restricting the set of rigid body modes onto their local support.

Further robust methods for solving linear elasticity problems are available, including the **multilevel methods** studied in [64, 74] and [63]. A purely algebraic multigrid method for linear elasticity problems is constructed based on so called computational molecules. The construction of the coarse space requires access to the element matrices, and thus it falls into the framework of AMGe (cf. [13, 61]). Such an approach has been studied earlier for the scalar elliptic problems in [76]. The approach allows that the kernel of the operator can be extracted from local Neumann problems which are assembled over subsets of fine elements. Particularly, the rigid body modes can can be identified automatically and do not need to be provided beforehand.

Applications of a multigrid approach based on a finite difference discretization of the elasticity system can be found in [111]. The latter is developed for the efficient simulation of elasticity problems on complex geometries, though heterogeneous material coefficients are not the particular concern.

Another extensive class of methods for solving the discrete linear systems which arise from the discretization of PDEs are **domain decomposition** methods. The method decomposes the computational domain into local subdomains on which corrections are performed. Based on the particular structure of the subdomains, one typically distinguishes between overlapping and non-overlapping domain decomposition methods. Prominent examples for the latter are FETI-methods or the BDDC methods [65, 66, 67, 79, 86, 97]. For highly heterogeneous problems, these methods may face difficulties, e.g. when material jumps occur at interfaces between the non-overlapping

subdomains. Domain decomposition methods which apply the local corrections on overlapping subdomains are also referred to as (overlapping) Schwarz methods.

For the elasticity system, two-level overlapping domain decomposition preconditioners have a large literature [59, 90, 94] (see also [26, 27]). As mentioned before in the introduction, the two-level method combines local corrections on the overlapping subdomains with a global correction on a coarse space spanned by a set of well-selected basis functions. For the generation of coarse spaces, aggregation based methods are observed in [59] and also in [90] in combination with partition of unity coarse spaces. The early work in [94] also contains vector-valued linear coarse spaces. The common feature of all these works is that the coarse space contains the rigid body modes.

Using a vector-valued linear coarse basis on a coarse triangulation $\mathcal{T}_H$, a condition number bound for the additive Schwarz preconditioned linear system (cf. chapter 2.3.1) can be obtained by

$$\kappa(M_{\mathrm{AS}}^{-1}A) \le C \max_i \sup_{x,y\in\Omega_i} \left(\frac{\lambda(x) + \mu(x)}{\mu(y)} \right) \left(1 + \frac{\tilde{H}}{\delta} \right). \tag{1.2}$$

Here, $\tilde{H}$ stands for the diameter of the largest subdomain, which is often assumed to be of similar size as the characteristic mesh size of the coarse triangulation $\mathcal{T}_H$. The parameter δ stands for the smallest overlap width of the overlapping local subdomains. As we can see from the estimate in (1.2), the two-level preconditioner removes the ill-conditioning due to the mesh parameters h^{-2} of the estimate in (1.1) by showing a dependence on the ratio $1 + \frac{\tilde{H}}{\delta}$. Furthermore, if the material coefficients are resolved by the coarse mesh or if they vary only mildly within each subdomain, the estimates guarantees a sufficiently low condition number. Indeed, this circumstance applies also in a more general context. Provided that the coefficient variations can be resolved by the coarse mesh, each of the methods in [26, 27, 59, 90, 94] as well as the multigrid and multilevel methods in [63, 64, 74, 101] work robustly. However, when large variations appear on a very small scale, i.e. in the interior of coarse elements or within local subdomains, the estimate in (1.2) presumes only poor robustness and faces even a general weakness of many solvers.

The lack of robustness of most solvers when applied to multiscale problems where variations in the PDE coefficients cannot be resolved by a coarse mesh has been overcome

first in the development of robust coarse spaces for scalar second order elliptic PDEs

$$-\operatorname{div}(\alpha\nabla u) = f, \tag{1.3}$$

with e.g. α being a highly oscillating coefficient on multiple scales. Using a piecewise linear finite element triangulation on the fine mesh, the condition number estimate

$$\kappa(M_{\mathrm{AS}}^{-1}A^{\mathrm{s}}) \leq C \max_i \sup_{x,y\in\Omega_i} \left(\frac{\alpha(x)}{\alpha(y)}\right)\left(1 + \frac{\tilde{H}}{\delta}\right)$$

shows the dependence of the preconditioned system to the mesh parameters (see e.g. [97]) and the magnitude of the jumps. Again, $\tilde{H}$ stands for the diameter of the largest subdomain and δ stands for the smallest overlap width of the local subdomains. The estimate is sharp if a piecewise linear coarse space is used, but may be too pessimistic when coarse spaces are applied which are adapted to the multiscale features of the underlying problem.

In [45], sharper condition number bounds for the two-level additive Schwarz method are presented for scalar elliptic PDEs. Specifically, coefficient independent convergence rates are provided for a large class of heterogeneous problems, without the requirement that coefficient jumps are resolved by a coarse mesh. A condition number bound for the additive Schwarz preconditioned linear system on a piecewise linear discretization of the PDE in (1.3) is obtained to be of the form

$$\kappa(M_{\mathrm{AS}}^{-1}A^{\mathrm{s}}) \leq C\left(\pi(\alpha)\,\gamma(1)\left(1 + \frac{H}{\delta}\right) + \gamma(\alpha)\right), \tag{1.4}$$

where two robustness indicators $\pi(\alpha)$ and $\gamma(\alpha)$ were introduced as a measure for the coefficient robustness of the subdomain partitioning and the coarse space, respectively. While the *partitioning robustness indicator* $\pi(\alpha)$ can be bounded in general by choosing subdomains with a sufficiently large overlap, the *coarse space robustness indicator* $\gamma(\alpha)$ is of main importance and provides guidance in the construction of robust coarse spaces for the two-level method. It is proportional to the α-weighted H^1-seminorm, the energy of the basis functions.

Based on the estimate in (1.4), specific multiscale coarse spaces are constructed in [45] which don't need the requirement that the coarse mesh resolves the coefficient jumps.

1. INTRODUCTION

For the construction of robust coarse spaces, the multiscale finite element method is applied.

Originally, the **multiscale finite element method** was introduced in the upscaling framework. Since resolving the material jumps on the finest scale when performing simulations is of high computational cost, the idea of the multiscale finite element method is to capture small scale features of the multiscale problem on coarser grid-levels without accurately resolving all the small scale components. It has been successfully applied to scalar elliptic PDEs with highly oscillating coefficients on multiple scales. Different variations of the method can be found in [4, 5, 34, 53, 54, 55], including their analysis in the homogenization framework. A more recent approach for elliptic interface problems is given in [21] (see also [81]), as well as the generalized multiscale finite element method in [35]. Other variants of multiscale methods include e.g. the variational multiscale methods in [56, 58] and the heterogeneous multiscale methods in [106, 107]. For linear elasticity problems, applications of multiscale finite element methods are yet to be studied outside the scope of this thesis. An adaptive local-global multiscale finite element method for a 2D linear elasticity problem is applied in [81] by proposing an extension of the multiscale finite volume element method presented in [31] for two-phase flow problems. The method iteratively adapts the current multiscale basis functions by combining an oversampling approach locally and a coarse scale simulation globally. In [81], applications to a structural optimization problem in 2D linear elasticity are presented.

Coming back to the estimate in (1.4), multiscale finite element coarse spaces are constructed in [45] and their robustness properties are studied. Specifically, using a scalar oscillatory multiscale finite element coarse space, robustness is proven for any coefficient variation which occurs in the interior of coarse elements, but also for coefficient variations along coarse element boundaries if the high contrast regions can be characterized as a union of disjoint islands. Reasonable assumptions on the overlapping subdomains may be required. For the linear elasticity system, a condition number bound as in (1.4) is not available yet, but is developed and investigated in the scope of this thesis.
The pioneering results in [45] have also been applied by some of their authors to construct basis functions of minimal energy in [98], subject to pointwise constraints which ensure that the kernel of the PDE operator, i.e. the constant functions, are preserved.

It was shown before in [110] that coarse spaces constructed by an explicit energy minimization (cf. [78, 105]) share similarities with multiscale-FE basis functions in the sense that the basis functions are locally harmonic in the interior of coarse elements, which makes them applicable also in an upscaling framework. Their construction requires solving additional global problems whose solutions implicitly state the boundary conditions of the basis functions (cf. section 5.5).

Energy minimizing methods have been proposed first in [105] and [78] and were further studied in [98, 110]. In [83], the approach is generalized and applied to non-hermitian matrices. The method was motivated in [105] from experimental results of one-dimensional problems, where the method is equivalent to the multiscale finite element method. It is based on improving the approximation properties of the coarse space by reducing its dependence on the PDE coefficients. In [78], energy minimizing coarse spaces are presented also for isotropic linear elasticity in the context of smoothed aggregation, which allows small overlaps in the supports of neighboring basis functions. While the classical energy minimizing methods with pointwise constraints are often referred to as trace-minimization, another interesting method is proposed in [91] which constructs basis functions by minimizing their energy subject to a set of functional constraints. This approach is applied to scalar elliptic PDEs and the objective is to prove the approximation property in a weighted Poincaré inequality. By a proper choice of the functional constraints, mesh and coefficient independent condition number bounds can be obtained. Further variants of coarse spaces with a minimal energy property, including local variants, can be found in [26, 61, 69, 103].

The approach in [42] also applies the scalar multiscale finite element method for the construction of robust coarse spaces. In [41] and [42], local generalized eigenvalue problems are solved and an initially constructed coarse space is extended by the remaining eigenfunctions corresponding to positive eigenvalues which lie under a predefined threshold. The dimension of the coarse space is in general larger than that of the coarse spaces presented e.g. in [45]. Its exact dimension depends strictly on the particular problem as it is related to the coefficient distribution in the underlying material. It can be influenced by the partition of unity functions which are used to set up the generalized eigenvalue problems. If the initial partition of unity is chosen to be the scalar multiscale finite element basis, the enrichment of the coarse space is, in most applications, rather moderate. The approach in [41] and [42] is generalized from scalar elliptic PDEs to

abstract PDE operators in [32], including applications to Stokes and Brinkman equation. More recently, this approach is extended in [108] from a two-level to a multilevel (AMLI, see e.g. [102], [75]) method for general s.p.d. operators. A theoretical verification of the robustness of the method when applied to linear elasticity is also presented. The dimension of the coarse space when applied to multiscale elasticity problems is, however, yet to be fully addressed.

The **spectral methods** in [32, 41, 42, 108] are successfully applied to various highly heterogeneous problems in $2D$ even for the class of problems where multiscale finite element and energy minimizing coarse spaces fail to be fully robust. The high computational cost of solving local eigenvalue problems may face additional challenges for applications in three spatial dimensions.

In a more recent approach in [95], a spectral approach as in [41] is applied in the aggregation framework. Generalized eigenvalue problems are solved in the overlapping regions of the local subdomains. Applications to isotropic linear elasticity problems are given and robustness is also guaranteed for arbitrary coefficient variations. The dimension of the coarse space strongly depends on the coefficient distribution in the overlapping regions. A nice review on recent spectral methods and their relation can be found in [109]. Applications of the spectral methods in [32, 42, 108] in the algebraic multilevel context are provided in [33].

To investigate the robustness of the presented methods on a specific problem, a main criterion which we stated is if coefficient variations can be resolved by a coarse mesh or not. Here, we also mention the small class of *quasi-monotone* coefficient distributions (cf. [29]). Under the condition that quasi-monotonicity arguments can be applied, optimal condition number bounds are proven for scalar elliptic problems for particular coefficient distributions which are not resolved by a coarse grid. We refer to [86, 87] for an analysis in the two-level context and [92] for the context of multilevel methods.

1.3   Main Achievements of the Thesis

The main achievements of the thesis can be summarized as follows:

- Extension of the multiscale finite element method of Hou and Wu in [53] ("A multiscale finite element method for elliptic problems in composite materials and

porous media") from scalar elliptic PDEs to the PDE system of linear elasticity:

(i) Construction of multiscale finite element basis functions with vector-valued linear and oscillatory boundary conditions;

(ii) Application and analysis in the context of two-level overlapping domain decomposition preconditioners.

- Construction of energy minimizing coarse spaces for multiscale problems in linear elasticity:

(i) Providing a robust construction of the basis functions;

(ii) Application and analysis in the context of two-level overlapping domain decomposition preconditioners.

- Comprehensive convergence analysis for the two-level additive Schwarz preconditioned linear system with coefficient-explicit condition number bounds:

(i) Developed bounds are sharp also for multiscale problems where coefficients cannot be resolved by a coarse mesh;

(ii) Bounds provide guidance in the construction of robust coarse spaces for the two-level method.

- Parallel and memory saving MPI-implementation of the PCG-accelerated two-level additive Schwarz preconditioner with application to real multi-phase elastic composites.

1.4 Structure of the Thesis

The thesis is organized as follows. In *chapter 2* we state the equations of linear elasticity and their discretization with vector-valued piecewise linear finite elements on a fine triangulation. We also summarize the ingredients of the two-level additive Schwarz preconditioner in an abstract form. Furthermore, we introduce the fine and coarse meshes in 3D which are used in the numerical tests presented in the subsequent chapters. We state main requirements and properties of a robust multiscale coarse space and summarize classical Poincaré and Korn-type inequalities.

1. INTRODUCTION

In *chapter 3* we extend the multiscale finite element method (MsFEM) with linear boundary conditions as formulated by Hou and Wu in [53] to the PDE system of linear elasticity. Resolving the heterogeneities on the finest scale, we utilize the (vector-valued) linear multiscale-FE basis for the construction of robust coarse spaces in the context of two-level overlapping domain decomposition preconditioners. We motivate and explain the construction and show that the constructed multiscale coarse space contains all the rigid body modes. Furthermore, we numerically observe the properties of the derived coarse space in an upscaling framework. Therefore, we present experimental results showing the approximation errors of the multiscale-FE coarse space w.r.t. the fine-scale solution. Under the assumption that the material jumps are isolated, i.e. they occur only in the interior of the coarse grid elements, the numerical tests show uniform convergence rates independent of the contrast in the Young's modulus within the heterogeneous material.

In *chapter 4* we extend the scalar multiscale finite element method with oscillatory boundary conditions in [53] to the system of anisotropic linear elasticity. We derive the reduced system which governs the oscillatory boundary data in a general setting which allows their construction on triangular, tetrahedral, quadrilateral and hexahedral coarse meshes and explain the derivation of the oscillatory multiscale finite element basis on a tetrahedral mesh in detail. We apply the approach for the construction of robust coarse spaces in the context of two-level overlapping domain decomposition preconditioners for the multi-phase elastic composites. Numerical results are presented for isotropic materials showing that robustness w.r.t. coefficient variations in the PDE can be achieved even for the class of problems where inclusions of high stiffness cross or touch coarse element boundaries.

Chapter 5 is concerned with constructing energy minimizing coarse spaces for the finite element discretization of mixed boundary value problems for displacements in compressible linear elasticity. Motivated from the multiscale analysis of the highly heterogeneous composite materials, we construct basis functions on a tetrahedral coarse mesh which obey a minimal energy property subject to global pointwise constraints. These constraints ensure that the rigid body translations are contained exactly, while rigid body rotations are preserved approximately by the coarse basis. Following the

numerical examples in chapter 3, the application is again twofold. Resolving the heterogeneities on the finest scale, we utilize the energy minimizing coarse space for the construction of robust two-level overlapping domain decomposition preconditioners. Thereby, we do not assume that coefficient jumps are resolved by the coarse grid, nor do we impose assumptions on the alignment of material jumps and the coarse triangulation. We only assume that the size of the inclusions is small compared to the coarse mesh diameter. Numerical tests show uniform convergence rates independent of the contrast in the Young's modulus within the heterogeneous material. Furthermore, we numerically observe the properties of the energy minimizing coarse space in an upscaling framework by presenting results showing the approximation errors of the energy minimizing coarse space w.r.t. the fine-scale solution.

Based on and motivated from the numerical results in the previous chapters, we present a comprehensive convergence analysis in *chapter 6*, analysing two-level overlapping Schwarz domain decomposition methods for the vector-valued piecewise linear finite element discretizations of the elasticity system. The focus lies, indeed, in the application to compressible, particle-reinforced composites of multiscale character, with large jumps in their material coefficients. We present coefficient-explicit bounds for the condition number of the two-level additive Schwarz preconditioned linear system. Thereby, we do not require that the coefficients are resolved by the coarse mesh. The bounds show a dependence of the condition number on the energy of the coarse basis functions, the coarse mesh and the overlap parameters. Similar estimates have been developed for scalar elliptic PDEs by Graham, Lechner and Scheichl [45]. The coarse spaces to which they apply here are assumed to contain the rigid body modes and can be viewed as generalizations of the space of piecewise linear vector-valued functions on a coarse triangulation. The developed estimates provide a concept for the construction of coarse spaces which can lead to preconditioners which are robust w.r.t. discontinuities in the Young's modulus and the Poisson ratio of the underlying composite. To confirm the sharpness of the theoretical findings, we analyse the multiscale coarse spaces developed in the chapters before in the context of the developed energy bounds. The theory also captures the anisotropic case and allows applications to multiphase materials with anisotropic constituents in two and three spatial dimensions.

Chapter 7 describes a parallel implementation of the two-level additive Schwarz preconditioner with oscillatory multiscale-FE coarse space. The parallelization of the method is described in detail, numerical results are presented testing the scalability of the algorithm and the robustness of the preconditioner. Furthermore, the method is applied to real elastic composites which are discretized with more than 10^8 degrees of freedom.

In *chapter 8*, we summarize the presented work and draw final conclusions.

The analysis carried out within the framework of this thesis is partially contained in [15, 16, 17, 19] and in the technical report [18].

2

Problem Formulation

The main goal of the thesis is to develop and analyse preconditioners for multiscale problems which arise from the finite element discretization with vector-valued, piecewise linear elements in compressible linear elasticity.

In this chapter, we introduce the problem setting in detail and summarize further tools which are required to solve the equations governing the linear elastic material behaviour. We introduce the function spaces and their corresponding norms which are necessary for the formulation of the finite element method (FEM) in section 2.1. Then we proceed with the continuous formulation of the governing PDE system and the discretization on the fine grid in section 2.2. Furthermore, we shortly summarize the two-level overlapping Schwarz method in the additive version in section 2.3. Additionally, for the numerical tests presented in the following chapters, we introduce the precise structure of the underlying fine and coarse meshes in three spatial dimensions. Moreover, in section 2.4, we give a short outlook on the properties of the multiscale coarse spaces which we construct within the scope of this thesis in the chapters 3, 4 and 5. Important Poincaré and Korn inequalities are introduced and summarized in section 2.5, they are required for the analysis carried out in chapter 6. In section 2.6, we summarize some of the introduced notations to which we refer in the subsequent chapters for clarity purposes.

2.1 Function Spaces

We consider an open and bounded Lipschitz domain $\Omega \subset \mathbb{R}^d$, $d = 2, 3$. For simplicity, we may always assume that Ω admits a decomposition into shape-regular meshes (see Definition 2.3.2). For the considerations in the next chapters we require certain function spaces for vector-valued functions in $\mathbb{R}^d$. We introduce them based on their scalar counterparts. The space of square integrable functions on Ω is defined by [36]

$$L^2(\Omega) := \left\{ v : \Omega \to \mathbb{R} : \int_\Omega v^2 \, dx < \infty \right\},$$

and introduces a norm $\|u\|_{L^2(\Omega)} := \sqrt{(u, u)_{L^2(\Omega)}}$ when equipped with the inner product

$$(u, v)_{L^2(\Omega)} := \int_\Omega uv \, dx.$$

We say that $u = v$ in $L^2(\Omega)$ if $u(x) = v(x)$ for all $x \in \Omega$ outside a set of Lebesgue measure zero (cf. [1, 36]). The norm and scalar-product on the space of integrable functions in $L^2(\Omega)$ can be transferred in a straightforward manner to vector-valued functions $\boldsymbol{u} \in [L^2(\Omega)]^d$,

$$[L^2(\Omega)]^d = \left\{ \boldsymbol{v} = (v_1, \dots, v_d)^\top : v_i \in L^2(\Omega), \ i = 1, \dots, d \right\},$$

by

$$\|\boldsymbol{u}\|_{[L^2(\Omega)]^d} := \sqrt{(\boldsymbol{u}, \boldsymbol{u})_{[L^2(\Omega)]^d}}, \qquad (\boldsymbol{u}, \boldsymbol{v})_{[L^2(\Omega)]^d} := \int_\Omega \boldsymbol{u} \cdot \boldsymbol{v} \, dx = \sum_{i=1}^d \int_\Omega u_i v_i \, dx.$$

Finite element discretizations introduce a variational formulation which extend the concept of classical derivatives. Therefore, the framework of weak or distributional derivatives (see e.g. [1]) is applied.

Definition 2.1.1. (Weak derivative)*[1] Let $u \in \mathcal{D}'(\Omega)$ be a distribution and let $\alpha = (\alpha_1, \dots, \alpha_d)^\top$ be a multi-index. The weak derivative $D^\alpha u$ is defined such that*

$$\int_\Omega D^\alpha u \zeta \, dx = (-1)^{|\alpha|} \int_\Omega u D^\alpha \zeta \, dx \quad \forall \zeta \in C_0^\infty(\Omega),$$

where $|\alpha| = \sum_{i=1}^{d} \alpha_i$ and

$$D^\alpha u = \frac{\partial^{|\alpha|} u}{\partial x_1^{\alpha_1} \dots \partial x_n^{\alpha_n}}.$$

Based on Definition 2.1.1, the *Sobolev space* $H^1(\Omega)$ is defined by (cf. [1])

$$H^1(\Omega) := \left\{ u \in L^2(\Omega) \, : \, D^\alpha u \in L^2(\Omega) \ \forall \, |\alpha| \leq 1 \right\}.$$

The partial derivatives have to be understood in the sense of distributions according to Definition 2.1.1. Equipped with the scalar-product

$$(u, v)_{H^1(\Omega)} := (u, v)_{L^2(\Omega)} + (\nabla u, \nabla v)_{[L^2(\Omega)]^d} = \sum_{|\alpha| \leq 1} \int_\Omega \partial^\alpha u \, \partial^\alpha v \, dx,$$

the space $H^1(\Omega)$ defines a Hilbert-space [36], its norm is given by

$$\|u\|_{H^1(\Omega)} := \left(\sum_{|\alpha| \leq 1} \int_\Omega |\partial^\alpha u|^2 \, dx \right)^{1/2}.$$

For vector-fields in $\mathbb{R}^d$, the derived function space reads

$$[H^1(\Omega)]^d = \left\{ \boldsymbol{v} = (v_1, \dots, v_d)^\top : v_i \in H^1(\Omega), \ i = 1, \dots, d \right\}.$$

Then, $[H^1(\Omega)]^d$ is a Sobolev space, its scalar-product is inherited from $H^1(\Omega)$ and given by

$$(\boldsymbol{u}, \boldsymbol{v})_{[H^1(\Omega)]^d} := \sum_{i=1}^{d} (u_i, v_i)_{H^1(\Omega)} = (\boldsymbol{u}, \boldsymbol{v})_{[L^2(\Omega)]^d} + (\nabla \boldsymbol{u}, \nabla \boldsymbol{v})_{[L^2(\Omega)]^{d \times d}}.$$

The latter term also defines a semi-norm on $[H^1(\Omega)]^d$, with

$$|\boldsymbol{v}|_{[H^1(\Omega)]^d} := \int_\Omega \nabla(\boldsymbol{v}) : \nabla(\boldsymbol{v}) \, dx = \int_\Omega \sum_{i,j=1}^{d} |\partial_i v_j|^2 \, dx.$$

Having introduced the norms and function spaces required for the variational formulation of the finite element discretization, we proceed with stating the equations governing the linear elastic material behaviour.

2.2 Governing Equations and their Discretization

2.2.1 The Equations of Linear Elasticity

We shall assume that $\Gamma = \partial\Omega$ admits the decomposition into two disjoint subsets Γ_{D_i} and Γ_{N_i}, $\Gamma = \overline{\Gamma_{D_i} \cup \Gamma}_{N_i}$ and $\mathrm{meas}(\Gamma_{D_i}) > 0$ for $i \in \{1, \ldots, d\}$. We consider a solid body in Ω, deformed under the influence of volume forces $\boldsymbol{f}$ and traction $\boldsymbol{t}$. Assuming a linear elastic material behaviour, the displacement field $\boldsymbol{u}$ of the body is governed by the mixed boundary value problem (BVP) [9]

$$-\mathrm{div}\,\boldsymbol{\sigma}(\boldsymbol{u}) = \boldsymbol{f}\ \ \text{in } \Omega, \tag{2.1}$$

$$\boldsymbol{\sigma}(\boldsymbol{u}) = \boldsymbol{C} : \boldsymbol{\varepsilon}(\boldsymbol{u})\ \ \text{in } \Omega, \tag{2.2}$$

$$u_i = g_i\ \ \text{on } \Gamma_{D_i}, \quad i = 1, \ldots, d,$$

$$\sigma_{ij}n_j = t_i\ \ \text{on } \Gamma_{N_i}, \quad i = 1, \ldots, d,$$

where $\boldsymbol{\sigma}$ is the stress tensor, the strain tensor $\boldsymbol{\varepsilon}$ is given by the symmetric part of the gradient of displacements

$$\boldsymbol{\varepsilon}(\boldsymbol{u}) = \frac{1}{2}\left(\nabla\boldsymbol{u} + \nabla\boldsymbol{u}^\top\right),$$

$\boldsymbol{n}$ is the unit outer normal vector on Γ and $\sigma_{ij}n_j = (\boldsymbol{\sigma}\cdot\boldsymbol{n})_i$. The fourth order elasticity tensor $\boldsymbol{C} = \boldsymbol{C}(x), x \in \Omega$ describes the elastic stiffness of the material under mechanical load. The coefficients $c_{ijkl}, 1 \leq i, j, k, l \leq d$ may contain large jumps within the domain Ω. They depend on the parameters of the particular materials which are enclosed in the composite. The boundary conditions are imposed separately for each component $u_i, i = 1, \ldots, d$ of the vector-field $\boldsymbol{u} = (u_1, \ldots, u_d)^\top : \bar{\Omega} \to \mathbb{R}^d$.

Isotropic linear elasticity: Equation (2.1) is the general form of the PDE system for anisotropic linear elasticity, which simplifies when the solid body consists of one or more isotropic materials. In this case, equation (2.2) can be expressed in terms of the Lamé constants λ and μ, which are characteristic constants of the specific material. The stiffness tensor of an isotropic material is given by $c_{ijkl} = \lambda\delta_{ij}\delta_{kl} + \mu(\delta_{ik}\delta_{jl} + \delta_{il}\delta_{jk})$ and the stress is $\boldsymbol{\sigma}(\boldsymbol{u}) = \lambda\mathrm{tr}(\boldsymbol{\varepsilon}(\boldsymbol{u}))\boldsymbol{I} + 2\mu\boldsymbol{\varepsilon}(\boldsymbol{u})$.

Let us assume for the following consideration that Ω is divided into two disjoint subdomains Ω^1, Ω^2 such that $\bar{\Omega} = \bar{\Omega}^1 \cup \bar{\Omega}^2$. Let each domain Ω^β contain an isotropic material

with Lamé coefficients $(\lambda_\beta, \mu_\beta)$, $\beta = 1, 2$, i.e.

$$\lambda(x) = \begin{cases} \lambda_1, \ x \in \Omega^1 \\ \lambda_2, \ x \in \Omega^2 \end{cases} \quad \mu(x) = \begin{cases} \mu_1, \ x \in \Omega^1 \\ \mu_2, \ x \in \Omega^2. \end{cases}$$

Let $\Gamma_{\text{face}} := (\bar{\Omega}^1 \cap \bar{\Omega}^2) \setminus \partial\Omega$ denote the interface between the two materials. Under the condition of ideal adhesion, equation (2.1) is of the form

$$\mu\Delta\boldsymbol{u} + (\lambda + \mu)\nabla(\nabla \cdot \boldsymbol{u}) = \boldsymbol{f} \quad \text{in } \Omega\backslash\Gamma_{\text{face}}, \tag{2.3}$$

$$[\boldsymbol{u}] = 0, \quad [\boldsymbol{t}] = 0 \quad \text{on } \Gamma_{\text{face}}. \tag{2.4}$$

Here, $t_j(\boldsymbol{u}) = \sigma_{ij}n_j$ is the normal component of the stress where $\boldsymbol{n}$ is the unit normal to Γ_{face} pointing to Ω^2. The square brackets denote the jump along Γ_{face}. More precisely, $[\boldsymbol{u}(x_0)] = \boldsymbol{u}^2(x_0) - \boldsymbol{u}^1(x_0)$ where $\boldsymbol{u}^\beta(x_0) := \lim_{\Omega^\beta \ni x \to x_0} \boldsymbol{u}(x)$, $\beta = 1, 2$, is the one sided limit of the vector field $\boldsymbol{u}$ in $x_0 \in \Gamma_{\text{face}}$.

The Lamé coefficients can also be expressed in terms of the Young's modulus $E > 0$ and the Poisson ratio $\nu \in (-1, 1/2)$ by (cf. [8])

$$\lambda = \frac{E\nu}{(1 + \nu)(1 - 2\nu)}, \quad \mu = \frac{E}{2(1 + \nu)}. \tag{2.5}$$

Each pair (E, ν) or (λ, μ) characterizes the properties of an isotropic material. For completeness, we also give the relation

$$E = \frac{\mu(3\lambda + 2\mu)}{\lambda + \mu}, \quad \nu = \frac{\lambda}{2(\lambda + \mu)}.$$

Remark 2.2.1. *We should point out here that we only consider compressible linear elastic materials ($\nu < 1/2$), which allows a discretization with piecewise linear (H^1-conforming) finite elements. To circumvent the effect of locking or volume locking, reasonable discretizations are available when dealing with nearly incompressible materials. Such methods include non-conforming finite elements (cf. [37, 68]) or a mixed variational formulation by introducing an additional penalty term (cf. [9, 14, 36]). In our observations, we always assume that the Poisson ratio ν is bounded away from 1/2.*

2.2.2 Variational Formulation

Consider the Sobolev space $\mathcal{V} := [H^1(\Omega)]^d$ of vector-valued functions whose components are square-integrable with weak first-order partial derivatives in the Lebesgue space $L^2(\Omega)$. We define the subspace $\mathcal{V}_0 \subset \mathcal{V}$,

$$\mathcal{V}_0 := \left\{ \boldsymbol{v} \in [H^1(\Omega)]^d : v_i = 0 \text{ on } \Gamma_{D_i},\ i = 1, \ldots, d \right\}. \tag{2.6}$$

Additionally, we define the manifold

$$\mathcal{V}_g := \left\{ \boldsymbol{v} \in [H^1(\Omega)]^d : v_i = g_i \text{ on } \Gamma_{D_i},\ i = 1, \ldots, d \right\}. \tag{2.7}$$

We assume $\boldsymbol{f} \in \mathcal{V}_0'$ to be in the dual space of $\mathcal{V}_0$, $\boldsymbol{t} \in [H^{-\frac{1}{2}}(\Gamma_N)]^d$ is in the trace space and $c_{ijkl} \in L^\infty(\Omega)$ to be uniformly bounded. Additionally, we require the stiffness tensor $\boldsymbol{C}$ to be positive definite, i.e. it holds $(\boldsymbol{C} : \boldsymbol{\varepsilon}(\boldsymbol{v})) : \boldsymbol{\varepsilon}(\boldsymbol{v}) \geq C_0\, \boldsymbol{\varepsilon}(\boldsymbol{v}) : \boldsymbol{\varepsilon}(\boldsymbol{v})$ for a constant $C_0 > 0$. Note that for an isotropic material with the parameters λ and μ, this condition holds when $C_0/2 < \mu < \infty$ and $C_0 \leq 2\mu + d\lambda < \infty$. We define the bilinear form $a : \mathcal{V} \times \mathcal{V} \to \mathbb{R}$,

$$a(\boldsymbol{u}, \boldsymbol{v}) := \int_\Omega (\boldsymbol{C} : \boldsymbol{\varepsilon}(\boldsymbol{u})) : \boldsymbol{\varepsilon}(\boldsymbol{v})\, dx. \tag{2.8}$$

This form is symmetric, continuous, and coercive on the subspace $\mathcal{V}_0$. The coercivity, i.e.

$$\exists\, c_0 > 0\ :\ a(\boldsymbol{v}, \boldsymbol{v}) \geq c_0 \left\| \boldsymbol{v} \right\|_{[H^1(\Omega)]^d}\ \forall \boldsymbol{v} \in \mathcal{V}_0,$$

can be shown by using Korn's inequality (see section 2.5). Furthermore, we define the continuous linear form $F : \mathcal{V} \to \mathbb{R}$,

$$F(\boldsymbol{v}) := \int_\Omega \boldsymbol{f} \cdot \boldsymbol{v}\, dx + \int_{\Gamma_N} \boldsymbol{t} \cdot \boldsymbol{v}\, ds.$$

The weak solution of (2.1) is then given in terms of $a(\cdot, \cdot)$ and $F(\cdot)$ by $\boldsymbol{u} \in \mathcal{V}_g$, such that

$$a(\boldsymbol{u}, \boldsymbol{v}) = F(\boldsymbol{v}) \quad \forall \boldsymbol{v} \in \mathcal{V}_0. \tag{2.9}$$

Under the assumptions above, a unique solution of the weak formulation in equation (2.9) is guaranteed by the Lax Milgram lemma [9].

Lemma 2.2.1. (Lax Milgram) *Let $\mathcal{V}$ be a Hilbert space, let the bilinear form $a_{\mathcal{V}}$: $\mathcal{V} \times \mathcal{V} \to \mathbb{R}$ be continuous and coercive. Then problem (2.9) is well-posed and has a unique solution $\boldsymbol{u} \in \mathcal{V}_g$.*

2.2.3   Finite Element Discretization

We want to approximate the solution of (2.9) in a finite dimensional subspace $\mathcal{V}^h \subset \mathcal{V}$. Therefore, let $\mathcal{T}_h$ be a quasi-uniform triangulation of $\Omega \subset \mathbb{R}^d$ into triangular ($d = 2$) or tetrahedral ($d = 3$) finite elements with mesh parameter h and let $\bar{\Sigma}_h$ be the set of vertices of $\mathcal{T}_h$ contained in $\bar{\Omega}$. Furthermore, let $\bar{\mathcal{N}}_h$ denote the corresponding index set of nodes in $\bar{\Sigma}_h$. We denote the number of grid points in $\bar{\Sigma}_h$ by n_p. Let

$$\mathcal{V}^h := \text{span}\left\{ \varphi_k^{j,h} : \bar{\Omega} \to \mathbb{R}^d : j \in \bar{\mathcal{N}}_h, k = 1, \ldots, d \right\} \tag{2.10}$$

be the space of continuous, vector-valued piecewise linear functions on $\mathcal{T}_h$. Each such basis function is of the form

$$\varphi_k^{j,h} = (\varphi_{k1}^{j,h}, \ldots, \varphi_{kd}^{j,h})^\top, \quad \varphi_{kl}^{j,h}(x^i) = \delta_{ij}\delta_{kl}, \; i \in \bar{\mathcal{N}}_h, \; l \in \{1, \ldots, d\},$$

where δ_{ij} denotes the Kronecker delta. For the sake of simplifying the notation, we assume a fixed numbering of the basis functions to be given. To be more specific, we assume that there exists a suitable surjective mapping $\{\varphi_k^{j,h}\} \to \{1, \ldots, n_d\}$, $\varphi_k^{j,h} \mapsto (j, k)$. Here, $n_d = dn_p$ denotes the total number of degrees of freedom (DOFs) of $\mathcal{V}^h$. Note that this mapping automatically introduces a renumbering from $\{1, \ldots, n_p\} \times \{1, \ldots, d\} \to \{1, \ldots, n_d\}$. We introduce the discrete analogies to the space in equation (2.6) and the manifold in equation (2.7) by

$$\mathcal{V}_0^h : \quad = \quad \left\{ \boldsymbol{v}^h \in \mathcal{V}^h : v_i^h = 0 \text{ on } \Gamma_{D_i}, \; i = 1, \ldots, d \right\}, \tag{2.11}$$

$$\mathcal{V}_g^h : \quad = \quad \left\{ \boldsymbol{v}^h \in \mathcal{V}^h : v_i^h = g_i \text{ on } \Gamma_{D_i}, \; i = 1, \ldots, d \right\}. \tag{2.12}$$

We want to find $\boldsymbol{u}^h \in \mathcal{V}_g^h$, where $\boldsymbol{u}^h = \boldsymbol{w}^h + \boldsymbol{g}^h$, with $\boldsymbol{w}^h \in \mathcal{V}_0^h$ and $\boldsymbol{g}^h \in \mathcal{V}_g^h$. More precisely, we seek $\boldsymbol{u}^h = (u_1^h, \ldots, u_d^h)^\top$ with

$$u_k^h = \sum_{j=1}^{n_p} \mathrm{u}_{(j,k)} \varphi_k^{j,h}, \quad k = 1, \ldots, d,$$

2. PROBLEM FORMULATION

such that

$$a(\boldsymbol{w}^h, \boldsymbol{v}^h) = F(\boldsymbol{v}^h) - a(\boldsymbol{g}^h, \boldsymbol{v}^h) \ \ \forall \boldsymbol{v}^h \in \mathcal{V}_0^h.$$

We define the index set of degrees of freedom of $\mathcal{V}^h$ by $\mathcal{D}_h = \{(j,k) \in \mathbb{N} : j \in \bar{\mathcal{N}}_h, \ k = 1, \ldots, d\} = \{1, \ldots, n_d\}$ and introduce the subset

$$\mathcal{D}_{h,0} : \quad = \quad \left\{ (i,k) \in \mathbb{N} : i \in \bar{\mathcal{N}}_h, \ x^i \notin \Gamma_{D_k} \right\}.$$

Furthermore, we may introduce $\mathcal{D}_{h,\Gamma_D} := \mathcal{D}_h \backslash \mathcal{D}_{h,0} \neq \emptyset$. Using the symmetry of the stiffness tensor $\boldsymbol{C}$, the bilinear form in (2.8) applied to the basis functions of $\mathcal{V}^h$ reads

$$a(\varphi_k^{i,h}, \varphi_l^{j,h}) \quad = \quad \int_\Omega \boldsymbol{\varepsilon}(\varphi_k^{i,h}) : \boldsymbol{C} : \boldsymbol{\varepsilon}(\varphi_l^{j,h}) \, \mathrm{d}x. \tag{2.13}$$

We define $A \in \mathbb{R}^{n_d \times n_d}$, $f \in \mathbb{R}^{n_d}$ by

$$A_{(i,k)(j,l)} = \begin{cases} a(\varphi_k^{i,h}, \varphi_l^{j,h}) & \text{if } (i,k) \in \mathcal{D}_{h,0}, (j,l) \in \mathcal{D}_{h,0}, \\ a(\varphi_k^{i,h}, \varphi_k^{i,h}) & \text{if } (i,k) = (j,l) \in \mathcal{D}_{h,\Gamma_D}, \\ 0 & \text{otherwise} \end{cases}$$

and

$$f_{(j,l)} = \begin{cases} F(\varphi_l^{j,h}) - \displaystyle\sum_{(i,k) \in \mathcal{D}_{h,\Gamma_D}} a(\varphi_k^{i,h}, \varphi_l^{j,h}) g_k(x^i) & \text{if } (j,l) \in \mathcal{D}_{h,0}, \\ a(\varphi_l^{j,h}, \varphi_l^{j,h}) g_l(x^j) & \text{if } (j,l) \in \mathcal{D}_{h,\Gamma_D}. \end{cases}$$

Observe that common supports of basis functions $\varphi_k^{i,h}$ and $\varphi_l^{j,h}$ with $(i,k) \in \mathcal{D}_{h,0}$, $(j,l) \in \mathcal{D}_{h,\Gamma_D}$ do not have a contribution to the entries in A. They only contribute to the loadvector $\mathbf{f}$. This leads to the sparse linear system

$$A\mathbf{u} = \mathbf{f}, \tag{2.14}$$

with the symmetric positive definite (s.p.d.) stiffness matrix A. The symmetry of A is inherited from the symmetry of $a(\cdot, \cdot)$ while the positive definiteness is a direct consequence of the coercivity of the bilinear form in (2.8). Note that in the construction above, the essential degrees of freedom in $\mathcal{D}_{h,\Gamma_D}$ are not eliminated from the linear system. The degrees of freedom related to Dirichlet boundary values are contained in the linear system by strictly imposing $u_i^h = g_i^h$ on $\Gamma_{D_i}, i \in \{1, \ldots, d\}$, i.e. any row in A

related to a Dirichlet degree of freedom contains only a non-zero entry on the diagonal. The remaining Dirichlet degrees of freedom in the columns of A vanish as they are transferred to the right-hand side in (2.14).

2.2.4 The Assembling Process

In the following, we shortly summarize the assembling process for the linear system in (2.14). Using the symmetry of the strain- and the stress tensor

$$\boldsymbol{\varepsilon} = (\varepsilon_{ij})_{i,j=1}^d, \quad \boldsymbol{\sigma} = (\sigma_{ij})_{i,j=1}^d,$$

and $\boldsymbol{C}$, the entries of $\boldsymbol{\sigma}$ in (2.2) can be computed from $(\sigma_{11}, \sigma_{22}, \sigma_{12})^\top = \tilde{\boldsymbol{C}} \, (\varepsilon_{11}, \varepsilon_{22}, 2\varepsilon_{13})^\top$ $(d = 2)$ or $(\sigma_{11}, \sigma_{22}, \sigma_{33}, \sigma_{23}, \sigma_{13}, \sigma_{12})^\top = \tilde{\boldsymbol{C}} \, (\varepsilon_{11}, \varepsilon_{22}, \varepsilon_{33}, 2\varepsilon_{23}, 2\varepsilon_{13}, 2\varepsilon_{12})^\top$ $(d = 3)$. For instance, given an isotropic material, the stiffness tensor $\tilde{\boldsymbol{C}}$ in Voigt notation takes the form

$$\tilde{\boldsymbol{C}} = \begin{pmatrix} 2\mu + \lambda & \lambda & 0 \\ \lambda & 2\mu + \lambda & 0 \\ 0 & 0 & \mu \end{pmatrix} \quad \text{or} \quad \tilde{\boldsymbol{C}} = \begin{pmatrix} 2\mu + \lambda & \lambda & \lambda & & & \\ \lambda & 2\mu + \lambda & \lambda & & 0 & \\ \lambda & \lambda & 2\mu + \lambda & & & \\ & & & \mu & 0 & 0 \\ & 0 & & 0 & \mu & 0 \\ & & & 0 & 0 & \mu \end{pmatrix}$$

in $\mathbb{R}^d$, $d = 2$ or $d = 3$, respectively. For implementation purposes, we introduce the matrix B_i related to a node $x^i \in \bar{\Sigma}_h$ in two or three spatial dimensions by

$$B_i = \begin{bmatrix} \partial_1 \varphi^{i,h} & 0 \\ 0 & \partial_2 \varphi^{i,h} \\ \partial_2 \varphi^{i,h} & \partial_1 \varphi^{i,h} \end{bmatrix} \quad \text{or} \quad B_i = \begin{bmatrix} \partial_1 \varphi^{i,h} & 0 & 0 \\ 0 & \partial_2 \varphi^{i,h} & 0 \\ 0 & 0 & \partial_3 \varphi^{i,h} \\ 0 & \partial_3 \varphi^{i,h} & \partial_2 \varphi^{i,h} \\ \partial_3 \varphi^{i,h} & 0 & \partial_1 \varphi^{i,h} \\ \partial_2 \varphi^{i,h} & \partial_1 \varphi^{i,h} & 0 \end{bmatrix},$$

respectively, where $\varphi^{i,h}$ is the scalar nodal basis function on $\mathfrak{T}_h$ with $\varphi^{i,h}(x^j) = \delta_{ij}$, $x^j \in \bar{\Sigma}_h$ and $\partial_j = \partial/\partial x_j$, $j = 1, \ldots, d$. It holds $\tilde{\boldsymbol{\varepsilon}}(\varphi_l^{j,h}) = B_j 1^l$ where $\varphi_l^{j,h} = \varphi^{j,h} 1^l$ and $1^l = (1_1^l, \ldots, 1_d^l)^\top$, $1_k^l = \delta_{lk}$. One can write, at least for $(i,k), (j,l) \in \mathcal{D}_{h,0}$,

$$A_{(i,k)(j,l)} = 1^{k^\top} \int_\Omega B_i^\top \tilde{\boldsymbol{C}} B_j \, \mathrm{d}x \, 1^l. \tag{2.15}$$

2. PROBLEM FORMULATION

As usual for finite element methods, the stiffness matrix A and the loadvector $\mathbf{f}$ in equation (2.14) may be assembled by sums of elemental contributions, rather than entry by entry as in equation (2.15). For each $\tau \in \mathcal{T}_h$, we define the element submatrix

$$\tilde{A}^\tau = \int_\tau B_\tau^\top \tilde{C} B_\tau \, dx, \tag{2.16}$$

where the matrix B_τ contains the nodal matrices $B_{\tau_i}, i = 1, \ldots, n_\tau$ corresponding to the n_τ vertices of τ ($n_\tau = 3$ for $d = 2$ and $n_\tau = 4$ for $d = 3$),

$$B_\tau = [B_{\tau_1}, \ldots, B_{\tau_{n_\tau}}].$$

An adaption of $\tilde{A}^\tau$ is required if τ touches the global boundary where Dirichlet conditions are applied. In this case, the adaption in (2.16) reads

$$A^\tau_{(i,k)(j,l)} = \begin{cases} \tilde{A}^\tau_{(i,k)(j,l)} & \text{if } (i,k) \in \mathcal{D}_{h,0}, (j,l) \in \mathcal{D}_{h,0}, \\ \tilde{A}^\tau_{(i,k)(i,k)} & \text{if } (i,k) = (j,l) \in \mathcal{D}_{h,\Gamma_D}, \\ 0 & \text{otherwise.} \end{cases} \tag{2.17}$$

In a similar way, we define the elemental contribution of the load vector by

$$f^\tau_{(j,l)} := \begin{cases} F^\tau(\varphi_l^{j,h}) - \sum\limits_{(i,k) \in \mathcal{D}_{h,\Gamma_D}} A^\tau_{(i,k)(j,l)} g_k(x^i) & \text{if } (j,l) \in \mathcal{D}_{h,0}, \\ A^\tau_{(i,k)(j,l)} g_l(x^j) & \text{if } (j,l) \in \mathcal{D}_{h,\Gamma_D}. \end{cases} \tag{2.18}$$

To assemble the global stiffness matrix A as well as the right-hand side $\mathbf{f}$ in (2.14) element-wise, for each $\tau \in \mathcal{T}_h$, the following applies:

1. Assemble A^τ as in (2.16) and (2.17) and compute $\mathbf{f}^\tau$ following (2.18). The essential boundary conditions are taken into account.

2. Update the global stiffness matrix respectively force-vector by the computed elementary contributions.

The latter step here requires additional information. The element-matrices A^τ as well as the corresponding element right-hand side are computed based on a local ordering. Their values have to be added to the appropriate locations in the global counterparts. In practice, all the computations are performed on one reference element τ_{ref}. We provide more details below restricting to elements in 3D.

The Reference Element: The computations of the elemental contributions to the stiffness matrix as well as right-hand side on a tetrahedral element τ is computed for a specific reference element τ_{ref} (see Figure 2.1). The coordinates in the tetrahedral reference element are ξ_1, ξ_2, ξ_3. The reference element is defined by the set $0 \leq \xi_1, \xi_2, \xi_3 \leq 1$, $\xi_1 + \xi_2 + \xi_3 \leq 1$. The shape functions of the linear tetrahedron are given such that they are zero at one surface of the element and one at the opposite vertex, that is

$$
\begin{aligned}
N_1(\xi_1, \xi_2, \xi_3) &= \xi_1, \\
N_2(\xi_1, \xi_2, \xi_3) &= \xi_2, \\
N_3(\xi_1, \xi_2, \xi_3) &= \xi_3, \\
N_4(\xi_1, \xi_2, \xi_3) &= 1 - \xi_1 - \xi_2 - \xi_3.
\end{aligned}
$$

For each $\tau \in \mathcal{T}_h$, there exists a bijective continuously differentiable mapping F,

$$
\begin{aligned}
F : \tau_{\text{ref}} &\rightarrow \tau, \\
(\xi_1, \xi_2, \xi_3) &\mapsto (x_1, x_2, x_3) := (F_1(\xi_1, \xi_2, \xi_3), F_2(\xi_1, \xi_2, \xi_3), F_3(\xi_1, \xi_2, \xi_3)),
\end{aligned}
$$

where

$$
F_i(\xi_1, \xi_2, \xi_3) = \sum_{j=1}^{4} x_i^{N_j} N_j(\xi_1, \xi_2, \xi_3).
$$

Here, $x_i^{N_j}$ denotes the i-th component of the vertex x^{N_j} of τ, positioned at the node where the corresponding shape function N_j has value 1 in τ_{ref}. We compute $\tilde{A}^\tau$ in equation (2.16) by

$$
\tilde{A}_\tau^{\tau_{\text{ref}}} := \int_{\tau_{\text{ref}}} B_{\tau_{\text{ref}}}^T \tilde{C} B_{\tau_{\text{ref}}} J^{-1} \, \mathrm{d}\xi, \tag{2.19}
$$

where, $B_{\tau_{\text{ref}}} = [B_{N_1}, B_{N_2}, B_{N_3}, B_{N_4}]$ with

$$
B_{N_i} = \begin{bmatrix} \partial_1 N_i & 0 & 0 \\ 0 & \partial_2 N_i & 0 \\ 0 & 0 & \partial_3 N_i \\ 0 & \partial_3 N_i & \partial_2 N_i \\ \partial_3 N_i & 0 & \partial_1 N_i \\ \partial_2 N_i & \partial_1 N_i & 0 \end{bmatrix}.
$$
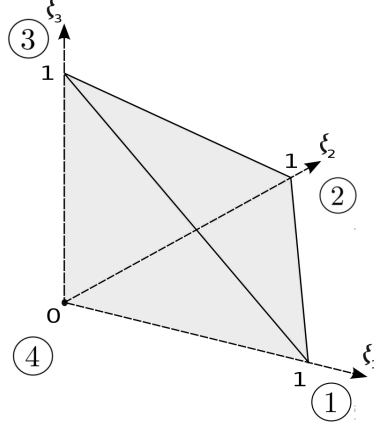
Figure 2.1: Reference tetrahedral element

Here, $\partial_j = \partial/\partial\xi_j$, $j = 1,\ldots,3$ and J stands for the Jacobian determinant of the transformation, given by

$$J = \det \begin{bmatrix} \partial_1 x_1 & \partial_2 x_1 & \partial_3 x_1 \\ \partial_1 x_2 & \partial_2 x_2 & \partial_3 x_2 \\ \partial_1 x_3 & \partial_2 x_3 & \partial_3 x_3 \end{bmatrix}. \tag{2.20}$$

More details on the assembling process in two and three spatial dimensions can be found in [57].

2.3 The Two-Level Method

We are interested in solving the linear system in equation (2.14) and hence, the construction of preconditioners for A which remove the ill-conditioning due to mesh-parameters and variations in the PDE coefficients. Specifically, we construct two-level Schwarz domain decomposition preconditioners in the additive version. As introduced before, the method involves corrections on local subdomains, combined with a global correction on a coarse grid. In this section, we summarize the additive Schwarz method in abstract form. Furthermore, we precisely introduce fine and coarse triangulations on a regular grid in 3D which we use in the subsequent chapters for the construction of different coarse spaces. The regular structure of both meshes allows the coarse elements to be formed by an agglomeration of fine elements.

2.3.1 Two-level Additive Schwarz

Let $\{\Omega_i, i = 1, \ldots, N\}$ be an overlapping covering of $\bar{\Omega}$, such that $\Omega_i \setminus \partial\Omega$ is open for $i \in \{1, \ldots, N\}$. $\Omega_i \setminus \partial\Omega$ is assumed to consist of the interior of a union of fine elements $\tau \in \mathcal{T}_h$. We introduce the notation

$$\mathcal{V}^h(\Omega_i) := \left\{ \boldsymbol{v}^h \in \mathcal{V}^h : \text{ supp}(\boldsymbol{v}^h) \subset \bar{\Omega}_i \right\}, \tag{2.21}$$

for the space of vector-valued piecewise linear functions which are supported in $\bar{\Omega}_i$. The notation can be applied to any subset $D \subset \bar{\Omega}$ in an obvious manner. Moreover, we denote the local index-set of degrees of freedom in $\mathcal{V}^h$ restricted to $D \subset \bar{\Omega}$ by

$$\mathcal{D}_h(D) := \left\{ (i, k) : \phi_k^{i,h} \in \mathcal{V}^h(D) \right\}, \tag{2.22}$$

where we assume a suitable local numbering of the global degrees of freedom to be given. For $i = 1, \ldots, N$, let R_i be the restriction matrix of a function in $\mathcal{V}^h = \mathcal{V}^h(\bar{\Omega})$ to $\mathcal{V}^h(\Omega_i)$. It is given by $(R_i)_{(j,l)(j',l')} = \delta_{(j,l)(j',l')}$, $(j, l) \in \mathcal{D}_h(\Omega_i)$, $(j', l') \in \mathcal{D}_h(\bar{\Omega})$ (more details can be found in [97]). We define the local submatrices of A corresponding to Ω_i by $A_i = R_i A R_i^\top$.

Additionally to the local subdomains, we need a coarse triangulation $\mathcal{T}_H$ of $\bar{\Omega}$ into coarse elements. Here, we assume again that each coarse element T consists of a union of fine elements $\tau \in \mathcal{T}_h$. We construct coarse basis functions whose values are determined on the coarse grid points in $\bar{\Omega}$ (excluding coarse DOFs on the Dirichlet boundaries), given by the vertices of the coarse elements in $\mathcal{T}_H$. The coarse space $\mathcal{V}_0^H \subset \mathcal{V}_0^h$ is constructed such that it is a subspace of the vector-field of piecewise linear basis functions on the fine grid. That is, each function $\phi^H \in \mathcal{V}_0^H$ omits a representation w.r.t. the fine scale basis. The *restriction matrix* R_H describes a mapping from the coarse to the fine space and contains the corresponding coefficient vectors of the coarse basis functions by row. The coarse grid stiffness matrix is then defined as the Galerkin product $A_H := R_H A R_H^\top$. With these tools in hand, the action of the two-level additive Schwarz preconditioner M_{AS}^{-1} is defined implicitly by

$$M_{\text{AS}}^{-1} = R_H^\top A_H^{-1} R_H + \sum_{i=1}^N R_i^\top A_i^{-1} R_i. \tag{2.23}$$

To accelerate convergence, the preconditioner in (2.23) can be applied to the linear system in (2.14) within a Krylov subspace method. The Preconditioned Conjugate Gradient (PCG) algorithm [44, 89] is well suited to symmetric problems.

Lemma 2.3.1. (PCG convergence) *Suppose we apply a s.p.d. preconditioner M to linear system $A\mathbf{u} = \mathbf{f}$ in (2.14). Then the iterates $\mathbf{u}^k$ computed in the k-th step of the PCG algorithm (Algorithm 7.1) satisfy the following bound*

$$\|\mathbf{u} - \mathbf{u}^k\|_A \ \leq \ 2 \left(\frac{\sqrt{\kappa(M^{-1}A)} - 1}{\sqrt{\kappa(M^{-1}A)} + 1} \right)^k \|\mathbf{u} - \mathbf{u}^0\|_A, \ \ k \geq 0,$$

where $\kappa = \lambda_{\max}/\lambda_{\min}$ is the ratio of the largest and smallest eigenvalue of $M^{-1}A$ and $\|\mathbf{u}\|_A^2 = \mathbf{u}^T A \mathbf{u}$.

That is, the number of iterations needed to solve the linear system iteratively with the PCG algorithm up to a given accuracy is proportional to $\sqrt{\kappa(M^{-1}A)}$.

2.3.2 Fine and Coarse Triangulation

We introduce the concepts of shape-regularity and quasi-uniform meshes following [36]:

Definition 2.3.1. (Mesh) *Let Ω be a domain in $\mathbb{R}^d$. A mesh is a union of a finite number n_{el} of compact, connected, Lipschitz sets τ_k with non-empty interior such that $\{\tau_k\}_{k=1}^{n_{\mathrm{el}}}$ forms a partition of Ω, i.e.*

$$\bar{\Omega} = \bigcup_{k=1}^{n_{\mathrm{el}}} \tau_k \quad and \quad \mathring{\tau}_k \cap \mathring{\tau}_l = \emptyset \quad for \ k \neq l.$$

The subsets τ_k are called elements and the set of elements $\mathfrak{T}_h := \{\tau_k\}_{k=1}^{n_{\mathrm{el}}}$ is referred to as mesh.

For $\tau \in \mathfrak{T}_h$, we denote by $h_\tau := \mathrm{diam}(\tau)$ and $\rho_\tau := \mathrm{diam}(B_\tau)$ the diameter of τ and B_τ, where B_τ is the largest circle (d=2) or ball (d=3) contained in τ.

Definition 2.3.2. (Shape regularity) *Let ρ_τ be defined as above. A family $\{\mathfrak{T}_h\}$ of meshes is said to be shape-regular if there exists σ_0 such that*

$$\forall h, \forall \tau \in \mathfrak{T}_h, \ \ \sigma_\tau := \frac{h_\tau}{\rho_\tau} \leq \sigma_0.$$

Definition 2.3.3. (Quasi-uniform) *A family $\{\mathcal{T}_h\}$ of meshes is said to be quasi-uniform if and only if it is shape-regular and there exists a constant c such that*

$$\forall h, \forall \tau \in \mathcal{T}_h, \ \ h_\tau \geq ch.$$

In the following, we introduce a quasi-uniform mesh which we consider for the numerical tests shown in the following chapters. However, none of the theoretical results developed in this thesis are restricted to the mesh introduced below. If not mentioned otherwise, they apply to any shape-regular triangulation.

Example of Fine Grid: Let the domain Ω be a 3D cube, i.e. $\bar{\Omega} = [0, L_x] \times [0, L_y] \times [0, L_z] \subset \mathbb{R}^3$ for given $L_x, L_y, L_z > 0$. The fine grid is constructed from an initial voxel structure which is further decomposed into tetrahedral finite elements [93]. More precisely, the set of grid points in $\bar{\Omega}$ is given by

$$\Sigma_h(\bar{\Omega}) := \Big\{ (x_i, y_j, z_k)^\top \in \mathbb{R}^3 : x_i = ih_x, \ y_j = jh_y, \ z_k = kh_z, \tag{2.24}$$
$$i = 0, \ldots, n_x, \ j = 0, \ldots, n_y, \ k = 0, \ldots, n_z \Big\},$$

where $n_x = L_x/h_x,, \ n_y = L_y/h_y, \ n_z = L_z/h_z$. For simplicity, we may assume that $L := L_x = L_y = L_z$ and $h := h_x = h_y = h_z$, and thus $n_h := n_x = n_y = n_z$. That is, the fine grid can be decomposed into $n_h \times n_h \times n_h$ grid-blocks, also referred to as voxels, of size $h \times h \times h$. We denote such a fine voxel by $\square_h^{ijk}$, $1 \leq i, j, k \leq n_h$. The triple (i, j, k) uniquely determines the position of the corresponding grid-block in $\bar{\Omega}$. Each voxel is further decomposed into five tetrahedral elements. The decomposition depends on the position of the specific voxel in $\bar{\Omega}$. To identify them, we introduce the notation $s^{ijk} := s(\square_h^{ijk}) = i + j + k$. We distinguish between two different decompositions, depending on the value of $s^{ijk} \bmod 2$. We follow the numbering of the 8 vertices of a block as given in Figure 2.2. If s^{ijk} is odd (see Figure 2.2 (a)), block $\square_h^{ijk}$ is decomposed into five tetrahedra which are defined by the set of their four vertices within each block,

$$\Big\{ \{1, 2, 4, 6\}, \{1, 3, 4, 7\}, \{1, 5, 6, 7\}, \{4, 6, 7, 8\}, \{1, 4, 6, 7\} \Big\}.$$

If s^{ijk} is even (see Figure 2.2 (b)), the decomposition of block $\square_h^{ijk}$ into the tetrahedra is done such that their vertices are given by

$$\Big\{ \{1, 2, 3, 5\}, \{2, 3, 4, 8\}, \{2, 5, 6, 8\}, \{3, 5, 7, 8\}, \{2, 3, 5, 8\} \Big\}.$$

With the given decomposition, a conformal triangulation of Ω into tetrahedral elements

(a)   (b)
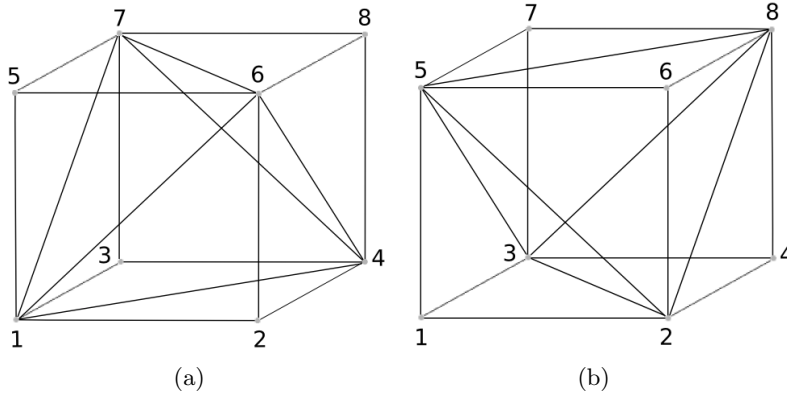
Figure 2.2: Decomposition of grid block into 5 tetrahedral elements

is uniquely defined, we denote this partition by $\mathfrak{T}_h$. $\mathfrak{T}_h$ is referred to as the fine grid triangulation, whereas the coarse grid triangulation, introduced in the following, is denoted by $\mathfrak{T}_H$.

Forming Coarse Elements by Agglomeration: The coarse elements $T \in \mathfrak{T}_H$ are constructed by an agglomeration of the fine elements. We construct a set of agglomerated elements such that each $T \in \mathfrak{T}_H$ is a simply connected union of fine grid elements $T = \bigcup_{i=1}^{n_T} \tau_i$, $\tau_i \in \mathfrak{T}_h$. Thus, for any two $\tau_i, \tau_j \in \mathfrak{T}_h \cap T$, there exists a connecting path of elements $\{\tau_k\}_k \subset T$ beginning in τ_i and ending in τ_j. Each fine grid element τ should belong to exactly one agglomerated element T. Due to the regular structure of the underlying fine grid, the agglomeration is done such that the coarse elements have the same tetrahedral form as the fine elements, and automatically form a coarser grid of equal structure. The table *AE_element* (cf. [102]) is used to store the fine elements which belong to an agglomerated (coarse) element. Given the fine triangulation $\mathfrak{T}_h$ of Ω, the agglomeration process proceeds as follows:

1. Given a fixed coarsening-factor c_f, compute the position of the coarse nodes to decompose the domain Ω into imaginary coarse voxels $\square_H^{ijk}$ of size $H \times H \times H$, where $1 \le i, j, k \le n_H \in \mathbb{N}$, $n_H = n_h/c_f$, and $H = c_f h$;

2. Build the *CB_element* table:
   For each $\tau \in \mathcal{T}_h$, obtain the position of τ in Ω and assign it to the belonging coarse block $\square_H^{ijk}$;

3. Build the *AE_element* table:
   For each coarse block $\square_H^{ijk} \subset \bar{\Omega}$ and each $\tau \subset \square_H^{ijk}$ (*CB_element*), obtain the position of τ in $\square_H^{ijk}$ and assign it to the belonging coarse tetrahedron;

In step 3 of the agglomeration process, we use again the mapping $s^{ijk} := s(\square_H^{ijk}) = i + j + k$ to identify the coarse tetrahedra into which a given block is decomposed. This partition automatically defines a set of coarse grid points, given by the vertices of the coarse elements. Specifically, they are given by

$$\Sigma_H(\bar{\Omega}) := \Big\{ (x_i, y_j, z_k)^\top \in \mathbb{R}^3 \, : \, x_i = iH, \, y_j = jH, \, z_k = kH,$$
$$i, j, k = 0, \ldots, n_H \Big\},$$

where $n_H = c_f h$ and $c_f = H/h \in \mathbb{N}$ denotes the coarsening ratio. We may write $\bar{\Sigma}_H := \Sigma_H(\bar{\Omega})$ for short. For any $D \subset \bar{\Omega}$, we denote by $\Sigma_H(D) := \bar{\Sigma}_H \cap D$ the set of nodes of $\mathcal{T}_H$ in D. The corresponding index-set of coarse nodes is defined by $\mathcal{N}_H(D)$. That is, $p \in \mathcal{N}_H(D)$ if and only if $x^p \in \Sigma_H(D)$. If $D = \bar{\Omega}$, we write $\bar{\mathcal{N}}_H = \mathcal{N}_H(\bar{\Omega})$ for short.

Note that the fine and coarse grid introduced above are quasi-uniform. It remains to show that a straightforward decomposition of a coarse block into coarse tetrahedral elements leads to the same result as forming the coarse tetrahedra by agglomerating fine elements. The proof of this concept is discussed below in more detail.

Alignment of Fine and Coarse Mesh

First, we demonstrate illustratively for one coarse tetrahedral element $T \in \mathcal{T}_H$ that it can be represented by a union of fine elements $\tau \in \mathcal{T}_h$. We restrict to the coarse element which is obtained from decomposing a coarse voxel $\square_H$ of size $H \times H \times H$ into five tetrahedra as described above, where $H = c_f h$ with c_f being the coarsening

factor. Particularly, referring to a decomposition as in Figure 2.2(a), we choose the element T with coarse vertices $\{1, 2, 4, 6\}$. We denote by $\mathcal{F}_{\text{int}}$ the interior face of T in $\Box_H := [0, H]^3$ which connects the three coarse nodes $\{1, 4, 6\}$ opposite to node 2 with coordinates $(H, 0, 0)^\top$. Then, T and $\mathcal{F}_{\text{int}}$ can be represented by

$$
\begin{aligned}
T &= \left\{ (x_1, x_2, x_3)^\top \in [0, H]^3 : 0 \leq (H - x_1) + x_2 + x_3 \leq H \right\}, \\
\mathcal{F}_{\text{int}} &= \left\{ (x_1, x_2, x_3)^\top \in [0, H]^3 : (H - x_1) + x_2 + x_3 = H \right\}.
\end{aligned}
$$

Given the fine mesh $\mathcal{T}_h(\Box_H) := \{ (ih, jh, kh)^\top \in [0, H]^3 : 0 \leq i, j, k \leq c_f \}$, we obtain the corresponding nodes in T and $\mathcal{F}_{\text{int}}$ by

$$
\begin{aligned}
\mathcal{T}_h(T) &= \left\{ x^{ijk} := (ih, jh, kh)^\top \in \mathcal{T}_h(\Box_H) : 0 \leq (c_f - i) + j + k \leq c_f \right\}, \\
\mathcal{T}_h(\mathcal{F}_{\text{int}}) &= \left\{ x^{ijk} := (ih, jh, kh)^\top \in \mathcal{T}_h(\Box_H) : (c_f - i) + j + k = c_f \right\}.
\end{aligned}
$$

For $\tau \in \mathcal{T}_h$, we denote by $\Sigma_h(\tau) := \bar{\Sigma}_h \cap \tau$ the set of vertices of τ. Let $\tau \in \mathcal{T}_h$ be such that there is a vertex $x^{i'j'k'} \in \Sigma_h(\tau)$ such that $x^{i'j'k'} \in T \setminus \partial T$ lies in the interior of the coarse element T. We want to show that any vertex $x^{ijk} \in \Sigma_h(\tau)$ lies in T and hence, $\tau \subset T$. W.l.o.g. we may assume that $x^{i'j'k'} \in \Sigma_h(\tau)$ is such that $(c_f - i') + j' + k'$ is minimal, that is we choose a vertex of τ which has shortest distance to the coarse node with coordinates $(H, 0, 0)^\top \in \Box_H$. Note that, by assumption, it holds $j' + k' - i' < 0$. To verify that τ lies fully in T we distinguish in our consideration between three different cases:

case 1: $j' + k' - i' \leq -3$: since $x^{i'j'k'} \in \Sigma_h(\tau)$ can only be connected to fine nodes of the form $x^{ijk} = x^{i' \pm 1\, j' \pm 1\, k' \pm 1}$ and due to $(j' + 1) + (k' + 1)(-i + 1)' \leq 0$, any node $x^{ijk} \in \Sigma_h(\Box_H)$ which is connected to $x^{i'j'k'}$ over an edge is contained in T.

case 2: $j' + k' - i' = -2$: then, we are in the situation of Figure 2.3 (b) and $x^{i'j'k'}$ can be connected to at least one of the coarse nodes x^{ijk} with $(i, j, k) \in \big\{ \{i' - 1, j' + 1, k'\}, \{i' - 1, j', k' + 1\}, \{i', j' + 1, k' + 1\} \big\}$ while the node x^{ijk} with $(i, j, k) = \{i' - 1, j' + 1, k' + 1\}$ does not share an edge with $x^{i'j'k'}$. Note that this situation occurs if and only if $i' + j' + k' \bmod 2 = 0$ (for an illustration compare also Figure 2.4).

case 3: $j' + k' - i' = -1$: then, we are in the situation of Figure 2.3 (a) and the other vertices of τ are given by $\{i' - 1, j', k'\}, \{i', j' + 1, k'\}$ and $\{i', j', k' + 1\}$. Note that this situation occurs if and only if $i' + j' + k' \bmod 2 = 1$ (for an illustration compare also Figure 2.4).

For the latter two cases we used that $(c_f - i') + j' + k'$ is assumed to be minimal. The above considerations show illustratively that all vertices of τ are contained in the

(a)   (b)
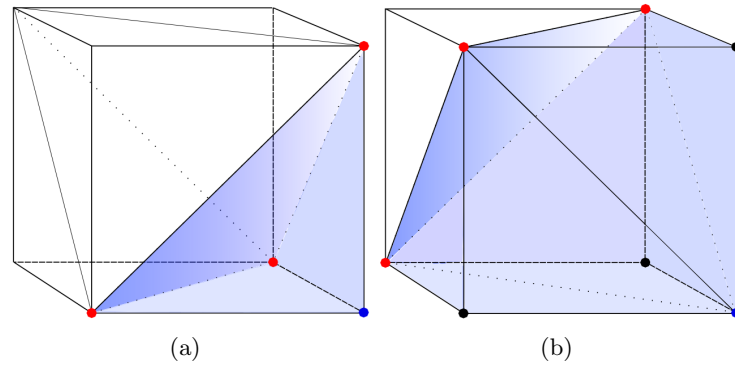
Figure 2.3: Illustration of fine tetrahedral elements which touch $\mathcal{F}_{\mathrm{int}}$ with one of their faces (shaded color); grid-points $x^{i'j'k'}$ in the interior of T (black and blue), grid-points $x^{i'j'k'}$ with $j' + k' - i'$ being minimal (blue) and grid-points on the boundary $\mathcal{F}_{\mathrm{int}}$ (red)

element $T \in \mathcal{T}_H$ and thus, T does not cut fine elements. This shows that the coarse element can be formed by a union of fine elements and hence, fine and coarse elements are aligned. The same arguments can be easily applied to any other $T \in \mathcal{T}_H(\square_H)$ which touches $\partial\square_H$ with a whole face. The remaining element $T' \in \mathcal{T}_H(\square_H)$ which touches the boundaries of $\square_H$ only with their vertices can be formed from the complementary union of fine elements $\tau \in \mathcal{T}_h(\square_H)$ which are not contained in any other $T \in \mathcal{T}_H(\square_H) \setminus T'$. While the above considerations provide a good illustration, we give a complete and more elegant proof of the concept of mesh alignment in the following.

Lemma 2.3.2. (Mesh alignment) *Let the fine and coarse meshes $\mathcal{T}_h$ and $\mathcal{T}_H$ be constructed as introduced above. Then, $\mathcal{T}_h$ and $\mathcal{T}_H$ are aligned.*

Proof. Let $\square_h^{ijk} \subset \bar{\Omega}$ be a fine grid-block. We introduce the four vectors $n^1 = (-1, 1, 1)^\top$, $n^2 = (1, -1, 1)^\top$, $n^3 = (1, 1, -1)^\top$ and $n^4 = (-1, -1, -1)^\top$. If s_h^{ijk} is odd (see Figure 2.2 (a)), they form the inner normal vectors on the four faces of the tetrahedron which is centered in the interior of $\square_h^{ijk}$, if s_h^{ijk} is even (see Figure 2.2 (b)), they
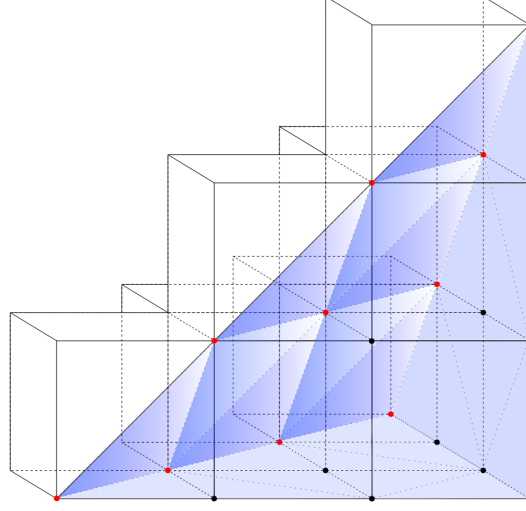
Figure 2.4: Illustration of coarse tetrahedral element with $H = 3h$ as an agglomeration of fine elements; Face $\mathcal{F}_{\text{int}}$ in shaded color; fine grid-points in the interior of T (black), grid-points on the boundary $\mathcal{F}_{\text{int}}$ (red)

form the outer normal vectors on the faces of the tetrahedron in the center of $\square_h^{ijk}$. The given normal vectors n^ℓ, $\ell = 1, \dots, 4$, characterize the four families of planes $\Xi_\ell^h := \left\{ n^\ell \cdot x = 2zh, x \in \bar{\Omega}, z \in \mathbb{Z} \right\}$. We want to show that these families induce the splitting of any fine voxel $\square_h^{ijk} \subset \bar{\Omega}$ into the five tetrahedra by their intersection with $\square_h^{ijk}$. To see this, let us first assume that s_h^{ijk} is odd, that is the fine voxel is decomposed according to the splitting in Figure 2.2 (a). We denote by $\mathcal{F}_\ell(\square_h^{ijk})$ the face of the tetrahedra in $\square_h^{ijk}$ which is normal to n^ℓ, $\ell \in \{1, \dots, 4\}$. Moreover, let $x^{i'j'k'} = (i'h, j'h, k'h)^\top$ be the vertex of $\square_h^{ijk}$ which is closest to the origin (node 1 in Figure 2.2 (a)), that is $(i', j', k') = (i - 1, j - 1, k - 1)$. Then it holds indeed that $(n^\ell \cdot x)/h \bmod 2 = (i' + j' + k') \bmod 2$ for all $x \in \mathcal{F}_\ell(\square_h^{ijk})$, $\ell = 1, \dots, 4$. Since $i + j + k$ is odd by assumption, we have that $(i' + j' + k') \bmod 2 = 0$. Hence, it holds $\mathcal{F}_\ell(\square_h^{ijk}) = \Xi_\ell^h \cap \square_h^{ijk}$ and the decomposition of $\square_h^{ijk}$ into tetrahedra is induced by the families Ξ^ℓ, $\ell = 1, \dots, 4$. Assuming now that s_h^{ijk} is even, the fine voxel is decomposed according to the splitting in Figure 2.2 (b). For $\ell = 1, \dots, 4$, let $\mathcal{F}_\ell(\square_h^{ijk})$ denote the angular face of the tetrahedra in $\square_h^{ijk}$ to which n^ℓ is normal. We denote by $x^{ijk} = (ih, jh, kh)^\top$ the vertex of $\square_h^{ijk}$ which is most distant form the origin (node 8 in Figure 2.2 (b)). It holds for all $x \in \mathcal{F}_\ell(\square_h^{ijk})$, $\ell \in \{1, \dots, 4\}$, that $(n^\ell \cdot x)/h \bmod 2 = (i + j + k) \bmod 2$. Since $i + j + k$ is even by assumption, we conclude again that $\Xi_\ell^h \cap \square_h^{ijk}$ defines the decomposition of $\square_h^{ijk}$ into tetrahe-

dra. The same arguments can be applied to show that for $\ell \in \{1, \ldots, 4\}$, the sets $\Xi_\ell^H := \{n^\ell \cdot x = 2zH, \, x \in \bar{\Omega}, \, z \in \mathbb{Z}\}$ form the family of planes which induce the decomposition of the coarse blocks into tetrahedra. Since the families Ξ_ℓ^h and Ξ_ℓ^H, $\ell = 1, \ldots, 4$, intersect in the origin and due to $H = c_f h$ for some $c_f \in \mathbb{N}$, the coarse grid family of planes is a subset of the fine ones which shows that fine and coarse meshes are aligned. $\qquad \square$

Having defined the coarse partition $\mathcal{T}_H$ of Ω into tetrahedral elements, we need grid-transfer operators R_H, respectively $R_H^\top$ which connect fine and coarse grid. In the following section we state requirements on the interpolation operators and the construction of coarse basis functions of multiscale character.

2.4 Robust Multiscale Coarsening

For scalar elliptic PDEs of multiscale character, a rigorous analysis of two-level overlapping domain decomposition preconditioners has successfully been developed in [45], including the construction of robust coarse spaces. Within the next chapters, we construct robust coarse spaces for multiscale problems in linear elasticity. In this section, we summarize the main properties of a robust coarse space and state the requirements when applying the multiscale framework to linear elasticity. The motivation is based on the increased kernel of the elasticity operator, which consists of the rigid body modes.

In section 2.3.2, we introduced the regular fine and coarse mesh which will be used in our numerical tests. However, we allow a more general framework for the construction of the basis functions, the assumptions on $\mathcal{T}_H$ can be slightly weakened. In general, we require that $\mathcal{T}_H$ is a conforming tetrahedral coarse mesh, such that each $T \in \mathcal{T}_H$ consists of a union of fine elements $\tau \in \mathcal{T}_h$ with $\mathcal{T}_H$ being shape-regular w.r.t. $H := \max_{T \in \mathcal{T}_H} H_T$, $H_T = \mathrm{diam}(T)$. Let Σ_H and $\bar{\Sigma}_H$ be the set of coarse nodes of $\mathcal{T}_H$ in Ω, respectively in $\bar{\Omega}$. For each coarse grid point $x^p \in \bar{\Sigma}_H$, we introduce the set

$$\omega_p := \mathrm{interior}\left(\bigcup_{\{T \in \mathcal{T}_H : x^p \in T\}} T \right), \qquad (2.25)$$

given by the interior of the union of coarse elements which are attached to node x^p. We will construct coarse vector-valued basis functions whose values are determined on the coarse grid points in $\bar{\Omega}$, given by the vertices of the coarse elements in $\mathcal{T}_H$. The

coarse basis functions are constructed such that they can be represented in terms of the vector-field of piecewise linear basis functions $\mathcal{V}^h$ on the fine grid. Here, we give an abstract formulation of the coarse spaces which we construct within the next chapters. It can be viewed as a generalization of the space of piecewise linear vector-fields on $\mathcal{T}_H$. The coarse basis functions are constructed to be of the following form:

Assumption 2.4.1. (Abstract coarse space)

(C1) $\phi_m^{p,\mathrm{H}} = (\phi_{m1}^{p,\mathrm{H}}, \ldots, \phi_{md}^{p,\mathrm{H}})^\top$, $\phi_{mk}^{p,\mathrm{H}}(x^q) = \delta_{pq}\, \delta_{mk}$, $p \in \bar{\mathcal{N}}_H$, $k \in \{1, \ldots, d\}$,

(C2) $\operatorname{supp} \phi_m^{p,\mathrm{H}} \subset \bar{\omega}_p$,

(C3) $\|\phi_{mk}^{p,\mathrm{H}}\|_{L^\infty(\Omega)} \leq C$, $k \in \{1, \ldots, d\}$,

(C4) $\sum_{p \in \bar{\mathcal{N}}_H} \phi_{mk}^{p,\mathrm{H}}(x) = \delta_{mk}$, $x \in \bar{\Omega}$, $k \in \{1, \ldots, d\}$,

(C5) $\mathcal{RBM}(\bar{\Omega}) \subset \operatorname{span}\big\{\phi_m^{p,\mathrm{H}} : p \in \bar{\mathcal{N}}_H,\ k \in \{1, \ldots, d\}\big\}$.

The space $\mathcal{RBM}(\bar{\Omega})$ of rigid body modes on $\bar{\Omega}$ is defined by

$$\mathcal{RBM}(\bar{\Omega}) = \begin{cases} \Big\{ v \in [L^2(\bar{\Omega})]^2 : v = a + b \begin{pmatrix} -x_2 \\ x_1 \end{pmatrix}, a \in \mathbb{R}^2,\ b \in \mathbb{R},\ x \in \bar{\Omega} \Big\}, & d = 2, \\ \Big\{ v \in [L^2(\bar{\Omega})]^3 : v = a + b \times x,\ a, b \in \mathbb{R}^3, x \in \bar{\Omega} \Big\}, & d = 3. \end{cases} \tag{2.26}$$

As the dependence on the domain $\bar{\Omega}$ is obvious, we may simply write $\mathcal{RBM} = \mathcal{RBM}(\bar{\Omega})$ instead. Moreover, we write $\mathcal{RBM}(D)$ when restricting the set of rigid body modes from $\bar{\Omega}$ to $D \subset \bar{\Omega}$.

Assumption *(C4)* implies that the rigid body translations are globally contained in the coarse space. Assumption *(C5)* states an additional requirement that the coarse space also contains the rigid body rotations.

Note that it is exactly the properties in Assumption 2.4.1 which we require to provide the analysis carried out in chapter 6. Given the coarse basis functions, we introduce the abstract coarse space by

$$\mathcal{V}^H := \operatorname{span}\Big\{ \phi_m^{p,\mathrm{H}} : p \in \bar{\mathcal{N}}_H,\ m = 1, \ldots, d \Big\}.$$

It is easy to verify that for all $u \in [H^1(\Omega)]^d$, it holds $\varepsilon(u) = 0 \Leftrightarrow u \in \mathcal{RBM}$. At least away from the boundary Γ_D where Dirichlet values are prescribed, the interpolation operator should be constructed such that it preserves the rigid body modes. The requirements can be summarized as follows:

1. The coarse basis should capture fine-scale information in the sense that the coarse space approximates the eigenfunctions corresponding to the smallest eigenvalues of the underlying PDE.

2. The coarse basis functions should be locally supported to ensure a certain sparsity pattern of the interpolation operator.

In the next chapters, we develop multiscale coarse spaces which satisfy the stated properties sufficiently.

2.5 Poincaré- and Korn-Type Inequalities

In linear elasticity, the semi-norm induced by the symmetrized gradient $\boldsymbol{\varepsilon}$ plays an important role. For any subset $\omega \subset \Omega$, we denote it by

$$|\boldsymbol{v}|^2_{\varepsilon,\omega} := \int_\omega \boldsymbol{\varepsilon}(\boldsymbol{v}) : \boldsymbol{\varepsilon}(\boldsymbol{v}) \, dx = \int_\omega \sum_{i,j=1}^d [\varepsilon_{ij}(\boldsymbol{v})]^2 dx.$$

Of special interest is how this semi-norm can be related to $|\cdot|_{[H^1(\omega)]^d}$, the semi-norm on $[H^1(\omega)]^d$. The relation is expressed in terms of Korn's inequalities, a fundamental tool in the analysis of the equations of linear elasticity. Introduced in the pioneering works of Korn [72, 73], they have been subject of further objective research [40, 52]. Several works are concerned with evaluating the Korn constants for bounded domains of specific shape [25, 50]. The existence of these bounds is not restricted to Lipschitz domains. They are also investigated for Jones domains (cf. [62]) in [30] or star shaped domains in [70, 71]. A short review can be found in [51].

In the following, we shortly summarize classical Poincaré- and Korn-type inequalities for vector-valued functions. The proofs of the next two lemmas can be found for scalar functions in [97]. The extension to vector-valued functions follows by a component-wise application. The explicit dependence on the size of the domain is obtained using a scaling argument [97, Section 3.4].

Lemma 2.5.1. (Scaled Poincaré inequality) *Let $D \subset \mathbb{R}^d$ be a Lipschitz domain of diameter H. Then, there is a constant $C > 0$ independent of H, such that $\forall \boldsymbol{u} \in [H^1(D)]^d$ with $\int_D \boldsymbol{u} \, dx = \boldsymbol{0}$,*

$$\|\boldsymbol{u}\|_{[L^2(D)]^d} \leq CH |\boldsymbol{u}|_{[H^1(D)]^d}.$$

2. PROBLEM FORMULATION

The lemma is a consequence of the Poincaré-inequality ([97], Lemma A.13) with vanishing mean value in each component and a scaling argument. If homogeneous Dirichlet conditions are applied on at least a part of the boundary, the following lemma applies.

Lemma 2.5.2. (Scaled Friedrichs inequality) *Let $D \subset \mathbb{R}^d$ be a Lipschitz domain with diameter H. Furthermore, let $\Gamma \subset \partial D$ with a positive $(d-1)$-dimensional measure and a diameter of order H. Then, there exists a constant C_Γ which only depends on Γ, but not on H, such that $\forall \boldsymbol{u} \in [H^1(D)]^d$ with $\boldsymbol{u} \mid_\Gamma = \boldsymbol{0}$,*

$$\|\boldsymbol{u}\|_{[L^2(D)]^d} \leq C_\Gamma H |\boldsymbol{u}|_{[H^1(D)]^d}.$$

It is a consequence of the component-wise application of the Friedrichs inequality for scalar functions ([97], Lemma A.14) and a scaling argument. For the proofs of Korn's inequalities, we refer to [40], [22] and the references therein.

Lemma 2.5.3. (Korn's first inequality) *Let $D \subset \mathbb{R}^d$ be a Lipschitz domain. Furthermore, let $\Gamma \subset \partial D$ have a positive $(d-1)$-dimensional measure. Then, there exists a constant $C_{D,\Gamma}$ which only depends on the shape of D and Γ, such that $\forall \boldsymbol{u} \in [H^1(D)]^d$ with $\boldsymbol{u} \mid_\Gamma = \boldsymbol{0}$,*

$$|\boldsymbol{u}|_{[H^1(D)]^d} \leq C_{D,\Gamma} |\boldsymbol{u}|_{\varepsilon,D}.$$

Lemma 2.5.4. (Korn's second inequality) *Let $D \subset \mathbb{R}^d$ be a domain in $\mathbb{R}^d$. Then, there exists a constant C_D such that $\forall \boldsymbol{u} \in [H^1(D)]^d$,*

$$\|\boldsymbol{u}\|_{[H^1(D)]^d} \leq C_D \big(|\boldsymbol{u}|_{\varepsilon,D} + \|\boldsymbol{u}\|_{[L^2(D)]^d} \big).$$

Several equivalent versions of Korn's inequality are studied in the literature. We know that the estimate in Lemma 2.5.3 does not hold in $[H^1(D)]^d$ for any rigid body rotation, while for rigid body translations, both sides in the estimate vanish. We denote by $\mathcal{RBM}(D)$ the space of rigid body modes on D. While Korn's first inequality only holds on a subspace of $\mathcal{RBM}(D)$, Korn's second inequality applies to any $\boldsymbol{u} \in [H^1(D)]^d$. The following formulation of Korn's inequality accentuates this feature.

Lemma 2.5.5. *Let $D \subset \mathbb{R}^d$ be a Lipschitz domain. Then, there exists a constant C_D which only depends on the shape of D, such that $\forall \boldsymbol{u} \in [H^1(D)]^d$,*

$$\min_{q \in \mathcal{RBM}(D)} |\boldsymbol{u} - \boldsymbol{q}|_{[H^1(D)]^d} \leq C_D |\boldsymbol{u}|_{\varepsilon,D}.$$

An important consequence of Lemma 2.5.1 and Lemma 2.5.5 is summarized in the Poincaré-Korn inequality:

Lemma 2.5.6. (Scaled Poincaré-Korn inequality) *Let $D \subset \mathbb{R}^d$ be a bounded Lipschitz domain of diameter H. Then, there exists a constant C_D which only depends on the shape of D, such that $\forall \boldsymbol{u} \in [H^1(\Omega)]^d$, there is $\boldsymbol{r} \in \mathcal{RBM}(D)$ such that*

$$\|\boldsymbol{u} - \boldsymbol{r}\|_{[L^2(D)]^d} \leq CH|\boldsymbol{u}|_{\varepsilon,D}.$$

Proof. Let $\boldsymbol{r}$ be the L^2-projection of $\boldsymbol{u}$ onto the space of rigid body modes $\mathcal{RBM}(D)$. Then, by definition, we obtain

$$\|\boldsymbol{u} - \boldsymbol{r}\|_{[L^2(D)]^d} = \min_{\boldsymbol{q} \in \mathcal{RBM}(D)} \|\boldsymbol{u} - \boldsymbol{q}\|_{[L^2(D)]^d}, \qquad (2.27)$$

or equivalently, $\int_D (\boldsymbol{u} - \boldsymbol{r}) \cdot \boldsymbol{q} \, dx = \boldsymbol{0}$ for all $\boldsymbol{q} \in \mathcal{RBM}(D)$. Plugging in the rigid body translations $\boldsymbol{q}_m = (q_{m1}, q_{m2}, q_{m3})^\top \in \mathcal{RBM}(D)$, $q_{mk} = \delta_{mk}$, $m = 1, \ldots, d$, we obtain

$$\int_D \boldsymbol{u} - \boldsymbol{r} \, dx = \boldsymbol{0}.$$

Now, let $\hat{\boldsymbol{r}} \in \mathcal{RBM}(D)$ be such that $\hat{\boldsymbol{r}} \in \arg\min_{\boldsymbol{q} \in \mathcal{RBM}(D)} |\boldsymbol{u} - \boldsymbol{q}|_{[H^1(D)]^d}$. By adding a constant vector to $\hat{\boldsymbol{r}}$, we may assume that $\int_D \boldsymbol{u} - \hat{\boldsymbol{r}} \, dx = \boldsymbol{0}$. Using equation (2.27), we obtain

$$
\begin{aligned}
\|\boldsymbol{u} - \boldsymbol{r}\|_{[L^2(D)]^d} &\leq & \|\boldsymbol{u} - \hat{\boldsymbol{r}}\|_{[L^2(D)]^d} \\
&\leq & CH|\boldsymbol{u} - \hat{\boldsymbol{r}}|_{[H^1(D)]^d} \\
&= & CH \min_{\boldsymbol{q} \in \mathcal{RBM}(D)} |\boldsymbol{u} - \boldsymbol{q}|_{[H^1(D)]^d} \\
&\leq & CH|\boldsymbol{u}|_{\varepsilon,D} \, ,
\end{aligned}
$$

where we used Lemma 2.5.1, the definition of $\hat{\boldsymbol{r}}$ and Lemma 2.5.5. $\qquad \square$

A similar result can be proven for vector-fields which have vanishing values on a part of the boundary. Therefore, we have to apply Friedrichs inequality and Korn's first inequality to obtain the following lemma.

Lemma 2.5.7. (Scaled Friedrichs-Korn inequality) *Let $D \subset \mathbb{R}^d$ be a bounded Lipschitz domain of diameter H. Furthermore, let $\Gamma \subset \partial D$ have a positive $(d-1)$-dimensional measure and a diameter of order H. Then, there exists a constant $C_{D,\Gamma}$ independent*

of H, *which only depends on the shape of D and Γ, such that $\forall \boldsymbol{u} \in [H^1(D)]^d$ with* $\boldsymbol{u} \mid_{\Gamma} = \boldsymbol{0}$,

$$\|\boldsymbol{u}\|_{[L^2(D)]^d} \leq C_{D,\Gamma} H |\boldsymbol{u}|_{\varepsilon,D}.$$

Proof. The assertion follows directly from Lemma 2.5.2 and Lemma 2.5.3. $\qquad\square$

2.6 Notations

Throughout the thesis, we assume $\Omega \subset \mathbb{R}^d$ to be a bounded, polygonal $(d = 2)$ or polyhedral $(d = 3)$ Lipschitz domain. Moreover, Ω shall admit a decomposition into fine and coarse meshes $\mathcal{T}_h$ and $\mathcal{T}_H$, respectively, consisting of triangles $(d = 2)$ or tetrahedra $(d = 3)$. The coarse mesh $\mathcal{T}_H$ is assumed to be formed by a union of fine elements $\tau \in \mathcal{T}_h$.

List of Selected Symbols

n_p, N_p	number of grid points of $\mathcal{T}_h$ and $\mathcal{T}_H$, respectively
$\mathcal{V}_h$	space of vector-valued piecewise linear basis functions $\{\varphi_k^{j,h}\}$ on $\mathcal{T}_h$
$\mathcal{V}_H$	space of coarse vector-valued basis functions on $\mathcal{T}_H$
$\Sigma_h(D)$	set of fine nodes $x^j \in \mathcal{T}_h \cap D$, $D \subset \bar{\Omega}$
$\Sigma_H(D)$	set of coarse nodes $x^p \in \mathcal{T}_H \cap D$, $D \subset \bar{\Omega}$
$\bar{\Sigma}_h$	set of fine nodes $x^j \in \Sigma_h(\bar{\Omega})$
$\bar{\Sigma}_H$	set of coarse nodes $x^p \in \Sigma_H(\bar{\Omega})$
$\mathcal{N}_h(D)$	index-set of nodes in $\Sigma_h(D)$
$\mathcal{N}_H(D)$	index-set of nodes in $\Sigma_H(D)$
$\bar{\mathcal{N}}_h$	index-set of nodes in $\bar{\Sigma}_h$
$\bar{\mathcal{N}}_H$	index-set of nodes in $\bar{\Sigma}_H$
n_d, N_d	number of degrees of freedom of $\mathcal{V}_h$ and $\mathcal{V}_H$, respectively
	$(n_d = d n_p, N_d = d N_p)$
$\mathcal{D}_h$	index-set of fine degrees of freedom in $\mathcal{V}_h$
$\mathcal{D}_H$	index-set of coarse degrees of freedom in $\mathcal{V}_H$
$\mathcal{T}_h(D)$	restriction of $\mathcal{T}_h$ to $D \subset \bar{\Omega}$
$\mathcal{T}_H(D)$	restriction of $\mathcal{T}_H$ to $D \subset \bar{\Omega}$
$\mathcal{D}_h(D)$	index-set (local numbering) of fine degrees of freedom in $\mathcal{V}_h(D)$
$\mathcal{D}_H(D)$	index-set (local numbering) of coarse degrees of freedom in $\mathcal{V}_H(D)$
$\bar{\omega}_p$	union of coarse elements $T \in \mathcal{T}_H$ which share the node $x^p \in \bar{\Sigma}_H$

To keep the indication of fine and coarse degrees of freedoms of $\mathcal{V}^h$ and $\mathcal{V}^H$ simpler, we use the following convention. To indicate degrees of freedom in $\mathcal{D}_h$, we use the

tuples (i, k) or (j, l), while the tuples (p, m) or (q, r) are used to indicate coarse degrees of freedom in $\mathcal{D}_H$. The first entry refers to the vertex with index $1 \leq i, j \leq n_p$, $1 \leq p, q \leq N_p$ and the second index to the *unknown* $k, l, m, r \in \{1, \ldots, d\}$ of the vector-fields in $\mathbb{R}^d$. Thereby, we may always interpret such a tuple as an integer value, i.e. we are given bijective mappings $\{1, \ldots, n_p\} \times \{1, \ldots, d\} \rightarrow \{1, \ldots, n_d\}$ and $\{1, \ldots, N_p\} \times \{1, \ldots, d\} \rightarrow \{1, \ldots, N_d\}$ which uniquely assign a integer value.

3

Multiscale Finite Elements with Linear Boundary Conditions

Multiscale finite element methods (MsFEMs) have been widely used when solving elliptic PDEs with highly oscillating coefficients on multiple scales. The idea of the multiscale finite element method is to capture small scale features of the solution on coarser grid-levels without accurately resolving all the small scale components. Beyond their application in the upscaling framework [34, 53, 54, 55], they are often utilized for the construction of two-level overlapping domain decomposition preconditioners, of main interest are problems where coefficient variations appear on a very small scale such that they cannot be resolved by a coarse grid.

In [45] and [46], coefficient independent convergence rates are proven for a large class of heterogeneous problems for scalar elliptic PDEs, without the requirement that coefficient jumps are resolved by a coarse mesh. Using a scalar multiscale finite element basis with linear boundary conditions, robustness is guaranteed if coefficient variations occur in the interior of coarse elements.

In this chapter we extend the linear multiscale finite element method, introduced for scalar elliptic PDEs by Hou and Wu [53], to the system of anisotropic linear elasticity. Although the capability of the adaption of multiscale finite elements to heterogeneous elasticity problems is often referred, to the authors knowledge, their application to the 3D system of linear elasticity has not yet taken place outside the scope of this thesis (see [19] and [17]). However, an application of an adaptive local-global multiscale finite element method to a 2D linear elasticity problem is given in [81]. There, an extension

of the multiscale finite volume element method presented in [31] for two-phase flow problems is proposed. This method iteratively adapts the current multiscale basis functions by combining an oversampling approach locally and a coarse scale simulation globally. In [81], applications to a structural optimization problem in 2D linear elasticity are presented.

The application here, motivated from the multiscale analysis of highly heterogeneous composite materials, is twofold. Resolving the heterogeneities on the finest scale, we utilize the linear multiscale-FE basis for the construction of robust coarse spaces in the context of two-level overlapping domain decomposition preconditioners. Furthermore, we numerically observe the properties of the multiscale-FE basis in an upscaling framework. Therefore, we present experimental results showing the approximation errors of the vector-valued linear multiscale finite element coarse space w.r.t. the fine-scale solution.

The outline of the chapter is as follows. Referring to the given setting and notations in section 3.1, we introduce the multiscale finite element basis with vector-valued linear boundary conditions in section 3.2. Details on the construction are provided in section 3.3. Moreover, we estimate the computational cost of the method in section 3.4 and compare the complexity with that of the scalar method in [53]. Furthermore, we study the properties of the linear multiscale finite element basis in section 3.5 and observe that it preserves the rigid body modes. The interpolation operator which is formed by the basis functions is defined in section 3.6. Section 3.7 is devoted to numerical results in 3D, a short discussion finalizes the chapter in section 3.8.

3.1 Preliminaries

Being in the setting which is stated in chapter 2, we use the notations of fine and coarse meshes, nodes and degrees of freedom as summarized in section 2.6. Details on the discretization are provided in section 2.2, the abstract two-level additive Schwarz method is introduced before in section 2.3.1.

3.2   Multiscale Coarsening: Linear Boundary Conditions

We construct a multiscale-FE coarse space $\mathcal{V}^H = \mathcal{V}^{\mathrm{MsL}}$ as a subspace of the finite element space $\mathcal{V}^h$ of the piecewise linear vector-valued basis functions (see equation (2.10)) on the fine triangulation $\mathcal{T}_h$. That is, the coarse space basis functions are represented by their values at the fine-grid DOFs. For $p \in \bar{\mathcal{N}}_H$, recall the set

$$\omega_p = \mathrm{interior}\bigg(\bigcup_{\{T \in \mathcal{T}_H : x^p \in T\}} T \bigg),$$

introduced before in section 2.4, which consists of the interior of the union of the coarse elements which are attached to $x^p \in \bar{\Sigma}_H$. For any $m \in \{1, \ldots, d\}$, we denote the vector-valued linear coarse nodal basis function corresponding to $p \in \bar{\mathcal{N}}_H$ by $\phi_m^{p,\mathrm{Lin}} : \omega_p \to \mathbb{R}^d$. More precisely, $\phi_m^{p,\mathrm{Lin}}$ is linear in $T \in \mathcal{T}_H$ and it holds $\phi_{mk}^{p,\mathrm{Lin}}(x^q) = \delta_{pq}\delta_{mk}, x^q \in \bar{\Sigma}_H$, $k \in \{1, \ldots, d\}$. For $p \in \bar{\mathcal{N}}_H$ and $m \in \{1, \ldots, d\}$ we construct a vector-valued multiscale-FE basis function $\phi_m^{p,\mathrm{MsL}} : \omega_p \to \mathbb{R}^d$. The construction is done separately for each $T \in \mathcal{T}_H$, such that it holds

$$\mathrm{div}(\mathrm{C} : \varepsilon(\phi_m^{p,\mathrm{MsL}})) \;\; = \;\; 0 \text{ in } T, \, T \subset \bar{\omega}_p, \tag{3.1}$$

$$\phi_m^{p,\mathrm{MsL}} \;\; = \;\; \phi_m^{p,\mathrm{Lin}} \text{ on } \partial T, \, T \subset \bar{\omega}_p. \tag{3.2}$$

Equation (3.1) and (3.2) have to be understood in the sense that they hold for $\phi_m^{p,\mathrm{MsL}}$ w.r.t. the discretization given by the fine grid. The vector-field $\phi_m^{p,\mathrm{MsL}}$ is PDE-harmonic in $T \subset \bar{\omega}_p$. On ∂T, linear boundary conditions are imposed in the m-th component of the vector-field and zero boundary conditions in the components $j \in \{1, \ldots, d\} \setminus \{m\}$. The imposed boundary values on ∂T ensure that the linear multiscale-FE basis function is continuous along the faces of the coarse elements. That is, it holds $\phi_m^{p,\mathrm{MsL}}(x) \mid_{T'} = \phi_m^{p,\mathrm{MsL}}(x) \mid_T = \phi_m^{p,\mathrm{Lin}}(x) \mid_T$ for all $x \in \partial T \cap \partial T'$, the corresponding multiscale-FE coarse space

$$\mathcal{V}^{\mathrm{MsL}} = \mathrm{span}\Big\{ \phi_m^{p,\mathrm{MsL}} \; : \; p \in \bar{\mathcal{N}}_H, \, m \in \{1, \ldots, d\} \Big\} \tag{3.3}$$

is conforming. Note that the support $\bar{\omega}_p, \, p \in \bar{\mathcal{N}}_H$ of the coarse basis function $\phi_m^{p,\mathrm{MsL}}$ is the same for each function $\phi_m^{p,\mathrm{MsL}}, m \in \{1, \ldots, d\}$.

3.3   Construction of the Linear Multiscale-FE Basis

The element-wise construction: Let $T \in \mathcal{T}_H$, let $x^p \in \Sigma_H(T)$ be a vertex of T and let $m \in \{1, \ldots, d\}$. By construction, $T = \cup \{\tau_i\}_{i=1}^{n_T}$ consists of a union of elements in $\mathcal{T}_h$. Let $\mathcal{V}^h(T) := \{\varphi^h \in \mathcal{V}^h : \operatorname{supp}(\varphi^h) \subset T\}$ and $\mathcal{V}_{|T}^h := \{\varphi^h|_T : \varphi^h \in \mathcal{V}^h\}$ denotes the restriction onto T of functions in $\mathcal{V}^h$. Furthermore, we denote the restriction of the bilinear form in (2.8) to $T \in \mathcal{T}_H$ by $a_T(\,\cdot\,,\,\cdot\,) : \mathcal{V}_{|T}^h \times \mathcal{V}_{|T}^h \to \mathbb{R}$. Following the BVP in (3.1) and (3.2), we want to find $\phi_m^{p,\mathrm{MsL}}|_T \in \mathcal{V}_{|T}^h$, with $\phi_m^{p,\mathrm{MsL}} = \phi_m^{p,\mathrm{Lin}}$ on ∂T, such that

$$a_T(\phi_m^{p,\mathrm{MsL}}, \boldsymbol{v}^h) := \int_T \left(\mathbf{C} : \boldsymbol{\varepsilon}(\phi_m^{p,\mathrm{MsL}}) \right) : \boldsymbol{\varepsilon}(\boldsymbol{v}^h) \, dx = 0, \quad \forall \boldsymbol{v}^h \in \mathcal{V}^h(T).$$

The finite element discretization leads to a local linear system $A_T \Phi_m^{p,T} = \mathbf{f}_m^{p,T}$. The system can be formed following the construction provided in section 2.2.3, with $\bar{\Omega}$ being replaced by T, and Γ_{D_i}, $i = 1, \ldots, d$, is replaced by ∂T. The coefficient vector $\Phi_m^{p,T}$ defines the solution to the problem in equation (3.1) and (3.2), discretized on $\mathcal{V}_{|T}^h$. It is given by $\phi_m^{p,\mathrm{MsL}}|_T = \sum_{(j,k) \in \mathcal{D}_h(\bar{\Omega})_{|T}} \Phi_{m,(j,k)}^{p,T} \varphi_k^{j,h}|_T$. Here, $\mathcal{D}_h(\bar{\Omega})_{|T}$ denotes the restriction onto T of the global degrees of freedom in $\mathcal{D}_h(\bar{\Omega})$. Note that the table *AE_element* formed in the element agglomeration process described in section 2.3.2 provides the required information of the fine elements contained in $T = \cup \{\tau_i\}_{i=1}^{n_T}$.

Construction of the coarse basis: Summarized, the procedure for the construction of the linear multiscale-FE basis is as follows:

1. For each $T \in \mathcal{T}_H$, the following applies

   - for each $p \in \mathcal{N}_H(T)$ and $m \in \{1, \ldots, d\}$, compute the solution $\phi_m^{p,\mathrm{MsL}}|_T$ of the BVP given in (3.1) and (3.2). Therefore, follow the procedure described above.

2. For each $p \in \bar{\mathcal{N}}_H$ and $m \in \{1, \ldots, d\}$, the following applies

   - assemble $\phi_m^{p,\mathrm{MsL}} : \omega_p \to \mathbb{R}^d$ from the computed vector-fields $\phi_m^{p,\mathrm{MsL}}|_T : T \to \mathbb{R}^d$ for which $T \subset \bar{\omega}_p$ shares the vertex x^p (see (2.25)). Therefore, assemble $\Phi_m^p \in \mathbb{R}^{n_d}$ by

     $$\Phi_{m,(j,k)}^p = \begin{cases} \Phi_{m,(j,k)}^{p,T} & \text{if } x^j \in \Sigma_h(T), \, T \subset \bar{\omega}_p, \\ 0 & \text{otherwise.} \end{cases}$$

The given vector defines the rows in the matrix $\bar{R}$ as given in equation (3.6). Note that since the basis function $\phi_m^{p,\mathrm{MsL}}$ is continuous along the element boundaries, the vector Φ_m^p is well-defined.

3.4 Complexity Estimate

In the following, we estimate the complexity of the construction of the linear multiscale finite element basis for linear elasticity. Let e be the number of vertices of T. Computing the basis function $\phi_m^{p,\mathrm{MsL}}\mid_T$ in equation (3.1) requires the solution of a sparse linear system with $O\left(d\left(\frac{H}{h}\right)^d\right)$ unknowns for any $T \in \mathcal{T}_H$, $q \in \mathcal{N}_H(T)$ and $m \in \{1, \ldots, d\}$. Using a solver with optimal order complexity, i.e. the computational cost per unknown is $O(1)$, the construction of the multiscale-FE basis requires the solution of $O(d\,e\,N_p)$ linear systems, each of which has computational cost of order $O\left(d\left(\frac{H}{h}\right)^d\right)$. Thus, the overall complexity can be estimated to $O(d^2\,e\,n_p)$ which is proportional to the number of nodes n_p on the fine grid $\mathcal{T}_h$.

Complexity of the Scalar Multiscale-FE Basis

Here, we shortly recapitulate the linear multiscale-FE method for scalar elliptic PDEs and provide a complexity estimate which we compare with the complexity of the vector-valued multiscale-FE basis for linear elasticity. A detailed and complete introduction into multiscale-FE methods for scalar PDEs can be found in [34]. We consider the scalar elliptic PDE $-\mathrm{div}(\alpha\nabla u) = f$ in Ω, where $\alpha = \alpha(x) > 0$ is a highly varying field in Ω. For any $p \in \bar{\mathcal{N}}_H$, the scalar multiscale finite element basis function $\phi^{p,\mathrm{msl}} : \omega_p \to \mathbb{R}$ is defined elementwise, i.e. for each $T \in \mathcal{T}_H$, by

$$\phi^{p,\mathrm{msl}}\mid_T = \begin{cases} \phi^{p,T} & \text{if } x^p \in \Sigma_H(T), \\ 0 & \text{otherwise,} \end{cases}$$

where $\phi^{p,T} : T \to \mathbb{R}$ is the α-harmonic extension of boundary data $\phi^{p,\mathrm{lin}} : \omega_p \to \mathbb{R}$ on ∂T, $T \in \mathcal{T}_H$ with $\phi^{p,\mathrm{lin}}$ being linear in $T \in \mathcal{T}_H$ and $\phi^{p,\mathrm{lin}}(x^q) = \delta_{pq}$, $q \in \bar{\mathcal{N}}_H$.

The complexity of the construction of the scalar multiscale finite element basis can be estimated as follows. For any $T \in \mathcal{T}_H$ and $x^p \in \Sigma_H(T)$, computing the basis function $\phi^{p,\mathrm{msl}}\mid_T$ requires the solution of a linear system with $O\left(\left(\frac{H}{h}\right)^d\right)$ equations. Using a solver for the linear system with computational cost scaling linearly with the number

of unknowns, the overall complexity of computing the scalar multiscale-FE basis can be estimated to $O\left(e\, N_p\, (\frac{H}{h})^d\right) = O(e\, n_p)$.

Comparing the complexity estimates for the scalar and elasticity problems, constructing the multiscale finite element basis for linear elasticity is more expensive by a factor of at least d^2 than the scalar multiscale basis. This factor appears naturally due to the larger number of degrees of freedom on the fine and the coarse mesh, respectively. Also, using tetrahedral elements ($e = 4$) allows a more efficient construction than hexahedral elements ($e = 8$).

In section 3.5 we see that, due to the PDE-harmonic extension of the vector-valued linear boundary conditions, the space $\mathcal{V}^{\mathrm{MsL}}$ contains the rigid body modes. Using the property that the translations are preserved (see equation (3.5)) a slight reduction of the setup cost to $O(d^2(e-1)n_p)$ can be achieved.

3.5 Properties

Indeed, assuming constant material coefficients in the PDE, the space $\mathcal{V}^{\mathrm{MsL}}$ recovers exactly the linear vector valued basis functions on the coarse grid $\mathcal{T}_H$. For the general case of varying coefficients, the following observation shows that the coarse space preserves the rigid body translations, separately for each unknown.

Global Translations: Due to the prescribed linear boundary conditions in (3.2), for each $m \in \{1, \ldots, d\}$ and $T \in \mathcal{T}_H$, it holds

$$\sum_{p \in \mathcal{N}_H(T)} \phi_{mk}^{p,\mathrm{MsL}} = \delta_{mk} \text{ on } \partial T, \ \ k \in \{1, \ldots, d\}. \tag{3.4}$$

The PDE-harmonic extension of the boundary data in (3.4) to the interior of T according to (3.1), together with the uniqueness of the solution (by Lemma 2.2.1), gives

$$\sum_{p \in \mathcal{N}_H(T)} \phi_{mk}^{p,\mathrm{MsL}} = \delta_{mk} \text{ in } T, \ \ k \in \{1, \ldots, d\}, \tag{3.5}$$

separately for each coarse element. Furthermore, this local argument can be extended to the global domain and it holds

$$\sum_{p \in \bar{\mathcal{N}}_H} \phi_{mk}^{p,\mathrm{MsL}} = \delta_{mk} \text{ in } \bar{\Omega}, \ k \in \{1, \ldots, d\}.$$

Thus, the translations are contained in the coarse space $\mathcal{V}^{\mathrm{MsL}}$, separately for each spatial component $m \in \{1, \ldots, d\}$.

Global Rotations: Next, we show representatively for $d = 3$ that the introduced space $\mathcal{V}^{\mathrm{MsL}}$ contains also the three rigid body rotations.

Lemma 3.5.1. *Let $\mathcal{V}^{\mathrm{MsL}}$ be the coarse space defined in (3.3) for $d = 3$. Then, $\mathcal{V}^{\mathrm{MsL}}$ contains the six rigid body modes, i.e. it holds*

$$\mathcal{RBM}(\bar{\Omega}) \subset \mathcal{V}^{\mathrm{MsL}}.$$

Proof. We have to show that the rotations around the m-th axis, $1^m \times x \in \mathcal{V}^{\mathrm{MsL}}$, $m \in \{1, 2, 3\}$, where $1^m \in \mathbb{R}^3, 1_k^m = \delta_{mk}, k \in \{1, 2, 3\}$. Here, we do not distinguish in our notation between a point $x \in \mathbb{R}^3$ and the identity mapping $x : \bar{\Omega} \to \mathbb{R}^3, x \mapsto x$, assuming that this should not lead to any confusion. For each $q \in \bar{\mathcal{N}}_H, m \in \{1, 2, 3\}$, we define the vector $\beta_m^q \in \mathbb{R}^3$,

$$\beta_{mk}^q := \sum_{l,n=1}^{3} \epsilon_{knl} \, \delta_{mn} \, x_l^q,$$

where ϵ_{knl} denotes the Levi-Civita-tensor [77], i.e. $\epsilon_{123} = \epsilon_{312} = \epsilon_{231} = 1$, $\epsilon_{321} = \epsilon_{213} = \epsilon_{132} = -1$ and $\epsilon_{kml} = 0$ otherwise. We have $x = \sum_{q \in \bar{\mathcal{N}}_H} x^q \phi^{q,\mathrm{lin}}(x)$ in $\bar{\Omega}$, where $\phi^{q,\mathrm{lin}}(x)$ is the scalar piecewise linear basis on $\mathcal{T}_H$ with $\phi^{q,\mathrm{lin}}(x^p) = \delta_{qp}$. In what follows, we first assume $x \in \partial T, T \in \mathcal{T}_H$. It holds

$$
\begin{aligned}
1^m \times x \ &= \ \sum_{q \in \bar{\mathcal{N}}_H} (1^m \times x^q) \, \phi^{q,\mathrm{lin}}(x) \quad \text{on } \partial T \\
&= \ \sum_{q \in \bar{\mathcal{N}}_H} \sum_{k=1}^{3} \beta_{mk}^q \, \phi_k^{q,\mathrm{Lin}}(x) \quad \text{on } \partial T \\
&= \ \sum_{q \in \bar{\mathcal{N}}_H} \sum_{k=1}^{3} \beta_{mk}^q \, \phi_k^{q,\mathrm{MsL}}(x) \quad \text{on } \partial T.
\end{aligned}
$$

The last step follows due to (3.2). Thus, along the boundaries of the coarse elements $T \in \mathcal{T}_H$, we can represent the rotation around the m-th axis as a linear combination of basis functions of $\mathcal{V}^{\text{MsL}}$. Using the argument which we used to validate equation (3.5), together with the uniqueness of the solution, we have

$$1^m \times x = \sum_{q \in \bar{\mathcal{N}}_H} \sum_{s=1}^{3} \beta^q_{ms} \phi^{q,\text{MsL}}_s(x) \text{ in } T,$$

locally for each $T \in \mathcal{T}_H$ and thus, also globally in $\bar{\Omega}$. The uniqueness argument holds here since, by equation (2.26), the vector field $1^m \times x$ is in the kernel of the elasticity operator and thus, it is a solution of $\text{div}(\mathbf{C} : \boldsymbol{\varepsilon}) = 0$. $\qquad \square$

Note that we concluded that from $\sum_q \phi^{q,\text{MsL}}_m \in \mathcal{V}^{\text{MsL}}$, $m \in \{1, 2, 3\}$, it follows $\sum_q \phi^{q,\text{MsL}}_m \times 1^m \in \mathcal{V}^{\text{MsL}}$. Indeed, this only holds for the sum of the basis functions, but not separately for each basis function. In general, we have $\phi \in \mathcal{V}^{\text{MsL}} \not\Rightarrow \phi \times 1^m \in \mathcal{V}^{\text{MsL}}$.

3.6   Interpolation Operator

In the following, we form the interpolation operator which is implicitly defined by the linear multiscale-FE coarse basis. We refer to the summary of notations in section 2.6 to recall notations of fine and coarse nodes and related degrees of freedom. We use the fine scale representation of a coarse basis function $\phi^{p,\text{MsL}}_m$ to define the interpolation operator, respectively the restriction operator. Each multiscale-FE basis function omits the representation

$$\phi^{p,\text{MsL}}_m = \sum_{k=1}^{d} \sum_{i=1}^{n_p} \bar{r}_{(p,m)(i,k)} \varphi^{i,h}_k. \tag{3.6}$$

This representation defines the matrix $\bar{R} \in \mathbb{R}^{N_d \times n_d}$ which contains the coefficient vectors, representing a coarse basis function in terms of the fine scale basis, by rows. Note that $\bar{R}$ does not define the final restriction operator used in the additive Schwarz setting. Assuming a numbering of the degrees of freedom by unknowns, the matrix $\bar{R}$ admits the block-decomposition

$$\bar{R} = \left(\bar{R}^{IJ}\right)^d_{I,J=1} \tag{3.7}$$

where $\bar{R}_{IJ} \in \mathbb{R}^{N_p \times n_p}$. Each block satisfies

$$\sum_{p=1}^{N_p} \bar{R}^{IJ}{}_{(p,I)(j,J)} = \delta_{IJ} \quad \forall j \in \{1, \ldots, n_p\}.$$

That is, the column sum of the diagonal-blocks is one, while the off-diagonals have column-sum zero. Note that, this is only true for the sum of the columns of each block. In general, this does not hold for the components itself. For $I \neq J$, we have $\bar{R}^{IJ}{}_{(p,I)(j,J)} = 0$ for all $p \in \{1, \ldots, N_p\}$ and $j \in \{1, \ldots, n_p\}$ if and only if the underlying material is homogeneous. In this case, where no coefficient jumps occur, the multiscale-FE basis functions exactly recover the vector-valued piecewise linear basis functions on the coarse grid, separately for each unknown. By construction, each row of the matrix $\bar{R}$ contains the fine-scale representation of a basis function of $\mathcal{V}^{\mathrm{MsL}}$. The restriction operator R_H, which we use in the additive Schwarz algorithm is then constructed as a submatrix of $\bar{R}$, which contains only the rows corresponding to coarse basis functions of $\mathcal{V}_0^{\mathrm{MsL}}$. Thus, it contains the rows related to coarse basis functions which vanish on the global Dirichlet boundaries Γ_{D_i}, $i = 1, \ldots, d$. Denoting the entries of R_H by $(r_{p'j'})_{p',j'}$, we define

$$r_{p'j'} = \bar{R}_{p'j'}, \;\; p' \in \mathcal{D}_H(\Omega^*), \;\; j' \in \mathcal{D}_h(\bar{\Omega}),$$

where $\mathcal{D}_H(\Omega^*)$, $\Omega^* := \bar{\Omega} \backslash (\cup^i \Gamma_{D_i})$ denotes the coarse interior degrees of freedom in Ω^*. The matrix representing the interpolation from the coarse space $\mathcal{V}_0^{\mathrm{MsL}}$ to the fine space $\mathcal{V}_0^h$ is simply given by the adjoint operator $R_H^\top$. The entries in the corresponding coarse stiffness matrix are determined by

$$
\begin{aligned}
A_{(p,m)(q,r)}^H &= \int_\Omega \tilde{\varepsilon}(\phi_m^{p,\mathrm{MsL}})^\top \tilde{\mathbf{C}}\, \tilde{\varepsilon}(\phi_r^{q,\mathrm{MsL}}) \, dx \\
&= \sum_{k,l=1}^d \sum_{i,j=1}^{n_h} r_{(p,m),(i,k)} \int_\Omega \tilde{\varepsilon}(\varphi_k^{i,h})^\top \tilde{\mathbf{C}} \tilde{\varepsilon}(\varphi_l^{j,h}) \, dx \, r_{(q,r),(j,l)} \quad (3.8)
\end{aligned}
$$

and the coarse stiffness matrix can be computed by the Galerkin product $A^H = R_H A R_H^\top$.

3.7 Numerical Results

In this section, we give a series of examples involving binary media, i.e. exactly two media are comprised in the composite, showing the performance of the linear multiscale-FE preconditioner under variations of the mesh parameters as well as the material coefficients. In addition to that, we measure the approximation error of the multiscale coarse space to a fine scale solution. In each experiment, we compare the multiscale coarse space with a standard linear coarse space. We perform our simulations on the domain $\bar{\Omega} = [0, 1] \times [0, 1] \times [0, L], L > 0$, with fine and coarse mesh as introduced in section 2.3.2. We consider two variants of heterogeneous media. First, we assume that the discontinuities are isolated, such that the material jumps occur only in the interior of coarse elements. Figure 3.1 shows such a binary medium with one inclusion inside each coarse tetrahedral element. In a second set of experiments, we do not impose any restriction on the position of the small inclusions. More precisely, we generate a binary medium whose inclusions are uniformly distributed. An example of such a medium is given in Figure 3.2, the structure is generated with GeoDict [43]. In the
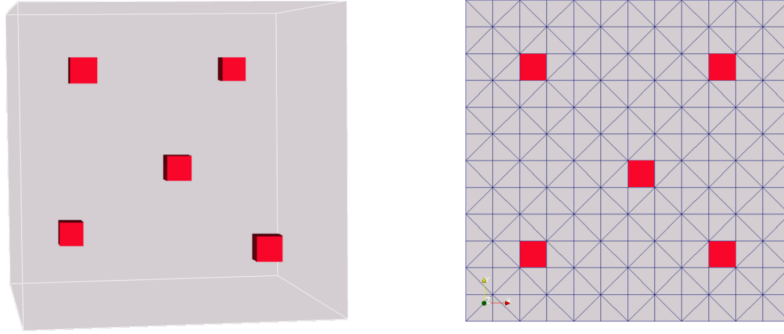
Figure 3.1: Medium 1: binary composite; matrix material (grey) and $1 \times 1 \times 1$ inclusions (red); discretization in $12 \times 12 \times 12$ voxels; each voxel is decomposed in 5 tetrahedra; 3D view (left) and 2D projection with fine mesh, showing the position of the inclusions (right)

following, we refer to the binary medium where inclusions are isolated in the interior of coarse elements as medium 1, while the medium with the random distribution of the inclusions is referred to as medium 2. For both media, the Young's modulus E as well as Poisson ratio ν for matrix material and inclusions are given in Table 3.1. The contrast $\Delta_E := E_{\text{inc}}/E_{\text{mat}}$ in the Young's modulus may vary over several orders of magnitude.
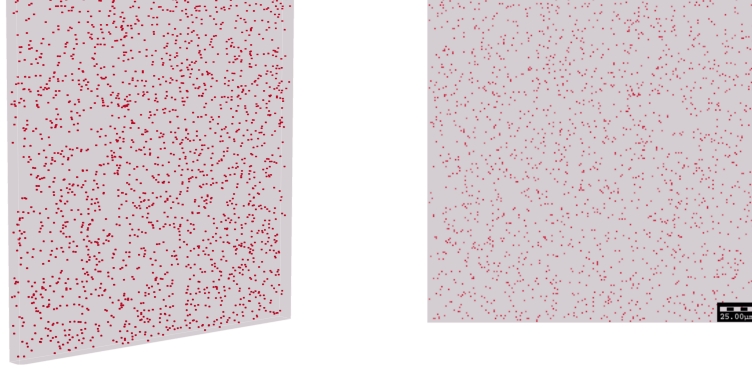
Figure 3.2: Medium 2: binary composite: discretization in $240 \times 240 \times 12$ voxels; matrix material (grey) and $1 \times 1 \times 1$ inclusions (red) uniformly distributed; 3D view (left) and 2D projection (right)

Young's modulus	Poisson ratio
$E_{\mathrm{mat}} = 1$ MPa	$\nu_{\mathrm{mat}} = 0.2$
$E_{\mathrm{inc}} = \Delta_E E_{\mathrm{mat}}$	$\nu_{\mathrm{inc}} = 0.2$

Table 3.1: Young's Modulus and Poisson ratio of matrix material and inclusions

3.7.1 Coarse Space Robustness

We choose the overlapping subdomains such that they coincide with the supports $\bar{\omega}_p$, $p \in \bar{\mathcal{N}}_H$ of the coarse basis functions. Then, $\{\Omega_i, i = 1, \dots, N\} = \{\omega_p, p \in \bar{\mathcal{N}}_H\}$ defines an overlapping covering of $\bar{\Omega}$ with overlap width $\delta = O(H)$, which is often referred to as *generous overlap*. We perform tests observing the performance of the two-level additive Schwarz preconditioner using vector-valued linear and multiscale-FE coarsening. We show condition numbers as well as iteration numbers of the PCG algorithm. The stopping criterion is to reduce the preconditioned initial residual by six orders of magnitude, i.e. $\|\mathbf{r}\|_{M_{AS}^{-1}} \leq 10^{-6} \|\mathbf{r}_0\|_{M_{AS}^{-1}}$. The estimated condition numbers of $\kappa(M_{AS}^{-1}A)$ are computed based on the three term recurrence which is implicitly formed by the coefficients within the PCG algorithm (cf. [89]).

In a first experiment, we test the robustness of the method on medium 1 for fixed mesh parameters under the variation of the contrast Δ_E. The Tables 3.2 and 3.3 show the corresponding condition numbers and iteration numbers having stiff ($\Delta_E > 1$) and soft ($\Delta_E < 1$) inclusions. In the former case, robustness is achieved only for the multiscale

3. MULTISCALE FINITE ELEMENTS WITH LINEAR BOUNDARY CONDITIONS

finite element coarse space, while linear coarsening leads to non-uniform convergence results. In the latter case, both coarse spaces are bounded in energy, an upper natural

	Lin		MsL	
Δ_E	n_{it}	$\kappa(M_{AS}^{-1}A)$	n_{it}	$\kappa(M_{AS}^{-1}A)$
10^0	13	4.4	13	4.4
10^3	21	18.7	13	4.4
10^6	25	109.0	13	4.4
10^9	25	109.0	13	4.4

Table 3.2: Iteration numbers n_{it} and condition numbers $\kappa(M_{AS}^{-1}A)$ for Experiment 1; geometry: $1/h$ x $1/h$ x H/h, $h = 1/240$, $H = 12h$; linear and multiscale-FE coarsening for different contrasts $\Delta_E \geq 1$

	Lin		MsL	
Δ_E	n_{it}	$\kappa(M_{AS}^{-1}A)$	n_{it}	$\kappa(M_{AS}^{-1}A)$
10^{-0}	13	4.4	13	4.4
10^{-3}	13	4.4	13	4.4
10^{-6}	13	4.4	13	4.4
10^{-9}	13	4.4	13	4.4

Table 3.3: Iteration numbers n_{it} and condition numbers $\kappa(M_{AS}^{-1}A)$ for Experiment 1; geometry: $1/h$ x $1/h$ x H/h, $h = 1/240$, $H = 12h$; linear and multiscale-FE coarsening for different contrasts $\Delta_E \leq 1$

bound is evidently given for $\Delta_E = 1$. Linear coarse space and multiscale-FE coarse space perform equally well.

In Experiment 2, performed on medium 1, we measure the condition numbers and iteration numbers under variation of the mesh parameters, while the coefficients of the PDE remain fixed. We observe similar results as in Experiment 1. Table 3.4 shows iteration and condition numbers for linear and multiscale-FE coarsening. For the linear coarse space, the condition number shows a linear dependence on the number of subdomains, while the condition number for multiscale coarsening is uniformly bounded.

To summarize, Experiment 1 and 2 show mesh and coefficient independent iteration and condition numbers for the multiscale-FE coarse space when the inclusions are isolated. In a second part, we test the performance of the method when small inclusions are allowed to touch coarse element boundaries. More precisely, we perform the same

	Lin		MsL	
h	n_{it}	$\kappa(M_{AS}^{-1}A)$	n_{it}	$\kappa(M_{AS}^{-1}A)$
1/60	14	7.9	13	4.4
1/120	17	28.1	13	4.4
1/180	21	61.8	13	4.4
1/240	25	109.0	13	4.4

Table 3.4: Iteration numbers n_{it} and condition numbers $\kappa(M_{AS}^{-1}A)$ for Experiment 2; geometry: $1/h$ x $1/h$ x H/h; $H = 12h$; linear and multiscale-FE coarsening for different h; contrast: $\Delta_E = 10^6$

experiments again and replace medium 1 by medium 2. We denote them by Experiment 3 and Experiment 4. As we already know, we cannot expect coefficient independent convergence rates when the inclusions in the binary medium are such that they cross coarse element boundaries. This is what we see in the Tables 3.5 and 3.6 for Experiment 3: For fixed mesh parameters under the variation of the contrast Δ_E, they show the corresponding condition numbers and iteration numbers having stiff ($\Delta_E > 1$) and soft ($\Delta_E < 1$) inclusions. Robustness is only achieved in the latter case where soft inclusions are considered. For stiff inclusions, both coarsening strategies lead to iteration numbers and condition numbers which depend on the contrast in the medium. We observe that in comparison with linear coarsening, the linear multiscale-FE coarse space performs not noticeably better.

	Lin		MsL	
Δ_E	n_{it}	$\kappa(M_{AS}^{-1}A)$	n_{it}	$\kappa(M_{AS}^{-1}A)$
10^0	13	4.4	13	4.4
10^3	27	19.3	18	8.4
10^6	66	414	78	373
10^9	68	427	75	465

Table 3.5: Iteration numbers n_{it} and condition numbers $\kappa(M_{AS}^{-1}A)$ for Experiment 3; geometry: $1/h$ x $1/h$ x H/h, $h = 1/240$, $H = 12h$; linear and multiscale-FE coarsening for different contrasts $\Delta_E \geq 1$

In Experiment 4, we measure the condition numbers and iteration numbers under variation of the mesh parameters for medium 2. The PDE coefficients remain fixed. The results agree with the observations in Experiment 3. Table 3.7 shows iteration and condition numbers for linear and multiscale-FE coarsening. Again, for each coarse space,

Δ_E	Lin		MsL	
	n_{it}	$\kappa(M_{AS}^{-1}A)$	n_{it}	$\kappa(M_{AS}^{-1}A)$
10^{-0}	13	4.4	13	4.4
10^{-3}	13	4.4	13	4.4
10^{-6}	13	4.4	13	4.4
10^{-9}	13	4.4	13	4.4

Table 3.6: Iteration numbers n_{it} and condition numbers $\kappa(M_{AS}^{-1}A)$ for Experiment 3; geometry: $1/h$ x $1/h$ x H/h, $h = 1/240$, $H = 12h$; linear and multiscale-FE coarsening for different contrasts $\Delta_E \leq 1$

h	Lin		MsL	
	n_{it}	$\kappa(M_{AS}^{-1}A)$	n_{it}	$\kappa(M_{AS}^{-1}A)$
$1/60$	26	39.2	27	37.7
$1/120$	48	154	43	109
$1/180$	52	261	62	230
$1/240$	66	414	78	373

Table 3.7: Iteration numbers n_{it} and condition numbers $\kappa(M_{AS}^{-1}A)$ for Experiment 4; geometry: $1/h$ x $1/h$ x H/h; $H = 12h$; linear and multiscale-FE coarsening for different h; contrast: $\Delta_E = 10^6$

iteration numbers as well as condition numbers grow with the number of subdomains. The multiscale-FE coarse space performs only slightly better than the linear coarse space.

3.7.2 Coarse Space Approximation

In a second set of experiments, we test the approximation properties of the multiscale-FE coarse space. The domain $\bar{\Omega} = [0,1] \times [0,1] \times [0,L]$ contains again a binary medium with small inclusions. Again, we distinguish between medium 1 (Figure 3.1: inclusions in the interior of each coarse element) and medium 2 (Figure 3.2: randomly distributed inclusions). We solve the system $-\mathrm{div}\,\boldsymbol{\sigma}(\boldsymbol{u}) = \boldsymbol{f}$ in $\bar{\Omega} \setminus \Gamma_D$ with a constant volume force $\boldsymbol{f} = (1,1,0)^\top$ in the x- and y-component. Homogeneous Dirichlet and Neumann boundary conditions are applied on the boundary $\partial\Omega$. Dirichlet conditions in the first unknown are given on $\Gamma_1 = \{(x,y,z)^\top \in \partial\Omega : x = 0, x = 1\}$, in the second unknown on $\Gamma_2 = \{(x,y,z)^\top \in \partial\Omega : y = 0, y = 1\}$, and in the third unknown on $\Gamma_3 = \{(x,y,z)^\top \in \partial\Omega : z = 0, z = L\}$.

Let $\boldsymbol{u}^h$ denote the approximate solution on a fine mesh $\mathcal{T}_h$. With the bilinear form defined in (2.9) and the space $\mathcal{V}_0^h$ of piecewise linear vector-valued basis functions as defined in (2.11), it holds $a(\boldsymbol{u}^h, \boldsymbol{v}^h) = F(\boldsymbol{v}^h) \ \forall \boldsymbol{v}^h \in \mathcal{V}_0^h$. This formulation leads to the linear system $A\mathbf{u^h} = \mathbf{f^h}$. We denote by $\mathcal{V}_0^{\mathrm{MsL}}$ the space of multiscale finite element functions on the coarse triangulation $\mathcal{T}_H$ which vanish on the Dirichlet boundary Γ_D. The multiscale finite element solution is given by $\boldsymbol{u}^{\mathrm{MsL}} \in \mathcal{V}_0^{\mathrm{MsL}}$, such that $a(\boldsymbol{u}^{\mathrm{MsL}}, \boldsymbol{v}^H) = F(\boldsymbol{v}^H) \forall \boldsymbol{v}^H \in \mathcal{V}_0^{\mathrm{MsL}}$. Using the fine-scale representation of a multiscale-FE basis function as defined in (3.6), the equivalent linear system reads $A_H \mathbf{u}^H = \mathbf{f}^H$. Here, $A_H = R_H A R_H^\top$ is the coarse stiffness matrix defined in equation (3.8), $\mathbf{f}^H = R_H \mathbf{f}^h$ and $\mathbf{u}^{\mathrm{MsL}} = R_H^\top \mathbf{u}^H$ is the vector whose entries define the fine-scale representation of $\boldsymbol{u}^{\mathrm{MsL}}$ in terms of the basis of $\mathcal{V}_0^h$.

For fixed mesh parameters h and H, under the variation of the contrast Δ_E, Table 3.8 and 3.9 show the relative approximation errors $\|\mathbf{u}^h - \mathbf{u}^c\|$ in l_2 and in the "energy" norm for linear (c=Lin) and linear multiscale-FE (c=MsL) coarse space for medium 1 and medium 2, respectively. The fine solution $\mathbf{u}^h$ is computed approximately within

Δ_E	$\dfrac{\|\mathbf{u}^h - \mathbf{u}^c\|_{l_2}}{\|\mathbf{u}^h\|_{l_2}}$		$\dfrac{\|\mathbf{u}^h - \mathbf{u}^c\|_A}{\|\mathbf{u}^h\|_A}$	
	Lin	MsL	Lin	MsL
10^{-9}	$8.63 \cdot 10^{-3}$	$8.11 \cdot 10^{-3}$	$8.92 \cdot 10^{-2}$	$8.54 \cdot 10^{-2}$
10^{-6}	$8.63 \cdot 10^{-3}$	$8.11 \cdot 10^{-3}$	$8.92 \cdot 10^{-2}$	$8.54 \cdot 10^{-2}$
10^{-3}	$8.63 \cdot 10^{-3}$	$8.11 \cdot 10^{-3}$	$8.91 \cdot 10^{-2}$	$8.54 \cdot 10^{-2}$
10^0	$8.09 \cdot 10^{-3}$	$8.09 \cdot 10^{-3}$	$8.53 \cdot 10^{-2}$	$8.53 \cdot 10^{-2}$
10^3	$7.39 \cdot 10^{-1}$	$9.42 \cdot 10^{-3}$	$8.60 \cdot 10^{-1}$	$9.44 \cdot 10^{-2}$
10^6	$9.97 \cdot 10^{-1}$	$9.44 \cdot 10^{-3}$	$9.99 \cdot 10^{-1}$	$9.45 \cdot 10^{-2}$
10^9	$9.97 \cdot 10^{-1}$	$9.44 \cdot 10^{-3}$	$9.99 \cdot 10^{-1}$	$9.45 \cdot 10^{-2}$

Table 3.8: Approximation of fine-scale solution by linear and multiscale finite element coarse space for medium 1; geometry: $1/h$ x $1/h$ x H/h, $h = 1/120$, $H = 12h$

the PCG algorithm by reducing the initial preconditioned residual by 12 orders of magnitude. The coarse solution $\mathbf{u}^H$ is computed exactly using a sparse direct solver for the coarse linear system. For medium 1, the multiscale-FE coarse space gives stable approximation errors, only slightly varying with the contrast. This is not the case anymore for the linear coarse space. For $\Delta_E \gg 1$, the fine-scale solution is contained in a space which is nearly A-orthogonal to the space spanned by the linear coarse

3. MULTISCALE FINITE ELEMENTS WITH LINEAR BOUNDARY CONDITIONS

basis functions. Note that this is in agreement with the results presented in Table 3.4, where the condition number grows almost linearly with the number of subdomains. For $\Delta_E \to \infty$, the coarse space does not correct the error anymore, the two-level method tends to perform as the one-level method. Considering medium 2, both coarse spaces only show a poor approximation of the fine-scale solution for high contrasts $\Delta_E \gg 1$. We can summarize the obtained results as follows. Assuming that the discontinuities

Δ_E	$\frac{\|\mathbf{u}^h - \mathbf{u}^c\|_{l_2}}{\|\mathbf{u}^h\|_{l_2}}$		$\frac{\|\mathbf{u}^h - \mathbf{u}^c\|_A}{\|\mathbf{u}^h\|_A}$	
	Lin	MsL	Lin	MsL
10^{-9}	$8.60 \cdot 10^{-3}$	$8.25 \cdot 10^{-3}$	$8.90 \cdot 10^{-2}$	$8.65 \cdot 10^{-2}$
10^{-6}	$8.60 \cdot 10^{-3}$	$8.25 \cdot 10^{-3}$	$8.90 \cdot 10^{-2}$	$8.65 \cdot 10^{-2}$
10^{-3}	$8.60 \cdot 10^{-3}$	$8.25 \cdot 10^{-3}$	$8.90 \cdot 10^{-2}$	$8.65 \cdot 10^{-2}$
10^{0}	$8.09 \cdot 10^{-3}$	$8.09 \cdot 10^{-3}$	$8.53 \cdot 10^{-2}$	$8.53 \cdot 10^{-2}$
10^{3}	$7.01 \cdot 10^{-1}$	$3.12 \cdot 10^{-1}$	$8.37 \cdot 10^{-1}$	$5.58 \cdot 10^{-1}$
10^{6}	$9.99 \cdot 10^{-1}$	$9.95 \cdot 10^{-1}$	$1.00 \cdot 10^{-0}$	$9.97 \cdot 10^{-1}$
10^{9}	$1.00 \cdot 10^{-0}$	$9.99 \cdot 10^{-1}$	$1.00 \cdot 10^{-0}$	$9.99 \cdot 10^{-1}$

Table 3.9: Approximation of fine-scale solution by linear and multiscale finite element coarse space for medium 2; geometry: $1/h$ x $1/h$ x H/h, $h = 1/120$, $H = 12h$

are isolated in the interior of coarse elements, the energy of a multiscale-FE basis function is bounded independently of the Young's modulus of the inclusions. Our experiments show uniform condition number bounds w.r.t. both, coefficient variations in the Young's modulus and the mesh size. When the distribution of the inclusions is such that they cross coarse element boundaries, the linear multiscale-FE basis function cannot capture the smallest eigenvalues associated to those inclusions which touch the coarse element boundary. The energy of the basis function depends on the Young's modulus of the inclusion. As the experiments show, no uniform iteration number and condition number bounds are achieved. For the considered medium with randomly distributed inclusions, the multiscale coarse space does not perform noticeably better than the linear coarse space.

3.8   Conclusions

In this chapter, we extend the linear multiscale finite element method to the PDE system of linear elasticity. The linear boundary conditions along coarse elements and the PDE-harmonic extension to their interior guarantee the following properties of the linear multiscale-FE basis:

1. Given the local boundary conditions, the energy of a multiscale-FE basis function is minimal within each coarse element (see also (6.17) for more details).

2. The rigid body translations are contained in the coarse space.

3. The rigid body rotations are contained in the coarse space.

4. Assuming homogeneous material coefficients, the multiscale-FE basis coincides with the vector-valued piecewise linear basis on the coarse triangulation.

The costs of constructing the linear multiscale-FE basis is of order d^2 more expensive for linear elasticity than for scalar elliptic PDEs. This factor appears naturally due to the larger number of degrees of freedom on the fine and the coarse mesh, respectively. We utilize the multiscale basis for the construction of two-level additive Schwarz preconditioners. When the discontinuities are isolated in the interior of coarse elements, our experiments show uniform condition number bounds w.r.t. both, coefficient variations in the Young's modulus and the mesh size. Along coarse element boundaries, the linear multiscale-FE basis is not PDE-harmonic. When inclusions cross a coarse element boundary, the prescribed linear boundary conditions lead to an increase in the energy of the multiscale basis function. The magnitude of the energy grows with the Young's modulus of the inclusions which cross the element boundaries. The condition number is not uniformly bounded.

Using the linear multiscale-FE coarse space in an upscaling framework, we also present experimental results in which we use the multiscale coarse space to approximate the fine-scale solution. When the inclusions are randomly distributed, the multiscale coarse space suffers from the inclusions which touch the coarse element boundaries and performs very similar to the linear coarse space. For the isolated inclusions, almost uniform approximation properties, independent of the contrast in the Young's modulus, are achieved.

3. MULTISCALE FINITE ELEMENTS WITH LINEAR BOUNDARY CONDITIONS

However, along the boundaries of the coarse elements, the small scale heterogeneities cannot be captured accurately by the presented multiscale-FE coarse space with linear boundary conditions. In case that material jumps occur through coarse element boundaries, the coarse space needs to be adapted. A possible extension can be given using oscillatory boundary conditions, similar to the ones in the scalar case (cf. [45, 53]), or energy minimizing methods (cf. [98, 110]). Such methods are studied in the following chapters.

The vector-valued character and the increased kernel of the elasticity system states an important difference to scalar elliptic PDEs, which can be seen also in the approaches presented in [32, 41, 42, 108], where generalized eigenvalue problems are solved. As mentioned in the introduction, numerical results for these spectral methods when applied to linear elasticity are not available yet, but a theoretical verification of the robustness of the method is already provided in [108]. The coarse spaces constructed there will contain the rigid body modes, multiplied with a (scalar) partition of unity. In contrast to the scalar version, we cannot expect that the spectral coarse space in [108] is an enrichment of the multiscale finite element basis.

4

Multiscale Finite Elements with Oscillatory Boundary Conditions

The application of the multiscale finite element method with vector-valued linear boundary conditions to linear elasticity as presented in chapter 3 shows that, if material jumps occur only in the interior of coarse grid elements, uniform condition number bounds which do not depend on the contrast in the Young's modulus are obtained. However, when stiff inclusions touch coarse element boundaries, the method fails to be robust. This motivates the construction of boundary conditions for the multiscale finite element basis which adapt to the heterogeneities in the PDE coefficients.

In this chapter we extend the multiscale finite element method with oscillatory boundary conditions, introduced for scalar elliptic PDEs by Hou and Wu in [53], to the system of anisotropic linear elasticity. We apply the approach for the construction of robust coarse spaces in the context of two-level overlapping domain decomposition preconditioners for multi-phase elastic composites. We explain the construction on a tetrahedral coarse mesh and present numerical results for isotropic materials showing that robustness w.r.t. coefficient variations in the PDE can be achieved even for the class of problems where inclusions of high stiffness cross or touch coarse element boundaries. For scalar elliptic PDEs, it is shown numerically and analytically in [45, 46] that scalar multiscale finite element basis functions with oscillatory boundary conditions may lead to robust two-level preconditioners, especially when the high contrast regions can be characterized as a union of disjoint islands [45].

The chapter is organized as follows. Referring to the overall setting in section 4.1, we precisely introduce the oscillatory multiscale finite element basis in section 4.2. Details on the construction are presented in section 4.3. The computational complexity as well as properties of the oscillatory multiscale basis are discussed in section 4.4 and 4.5, respectively. In Section 4.6, we present numerical results on a binary medium in 3D, the conclusions in section 6.7 finalize the chapter.

4.1   Preliminaries

We are in the setting as stated in chapter 2. That is, we are given a bounded domain $\Omega \subset \mathbb{R}^d$ which admits a decomposition into fine and coarse meshes $\mathcal{T}_h$ and $\mathcal{T}_H$, respectively. Details on the discretization are provided in section 2.2, the two-level additive Schwarz method is introduced before in section 2.3.1. We refer to section 2.6 for a summary of required notations.

4.2   Multiscale Coarsening: Oscillatory Boundary Conditions

A good choice of the local boundary conditions for the multiscale finite element basis can significantly improve the quality of the coarse space, as the boundary conditions determine how well local properties of the PDE are captured by the basis functions. Multiscale basis functions with oscillatory boundary conditions are introduced for scalar elliptic PDEs in [53] to also reflect the heterogeneities in the PDE coefficients across coarse element boundaries. The approach extracts boundary values on ∂T by solving reduced problems on the edges respectively the faces of a coarse element $T \in \mathcal{T}_H$. In the following, we extend this method to linear elasticity and formulate the reduced problems on ∂T. Also, we precisely describe the construction of the resulting oscillatory multiscale-FE basis and summarize the algorithm for solving the subproblems on the edges and faces of a coarse tetrahedral element $T \in \mathcal{T}_H$. We define the coarse basis and introduce suitable coordinate transformations that allow the derivation of the equations which govern the boundary data of the oscillatory multiscale-FE basis on general meshes. On composites with isotropic constituents, we present the construction in detail. For any $p \in \bar{\mathcal{N}}_H$ and $m \in \{1, \dots, d\}$, the oscillatory multiscale-FE basis

function $\mathcal{V}^h \ni \phi_m^{p,\text{MsO}} : \omega_p \to \mathbb{R}^d$ is defined such that for $T \subset \bar{\omega}_p$,

$$\text{div}(C : \varepsilon(\phi_m^{p,\text{MsO}})) \;=\; 0 \qquad \text{in } T, \tag{4.1}$$

$$\phi_m^{p,\text{MsO}} \;=\; \eta_m^{p,T} \quad \text{on } \partial T, \tag{4.2}$$

where the oscillatory boundary data $\eta_m^{p,T} : \partial T \to \mathbb{R}^d$ is continuous and compatible, i.e. $\eta_m^{p,T} = \eta_m^{p,T'}$ on $\partial T \cap \partial T' \subset \bar{\Omega}$ for $T, T' \in \mathcal{T}_H$. We impose the vector-valued nodal constraints

$$\eta_{mk}^{p,\text{T}}(x^q) = \delta_{pq}\delta_{mk}, \; q \in \mathcal{N}_H(T), \; k \in \{1, \ldots, d\}, \tag{4.3}$$

and show how $\eta_m^{p,T} = (\eta_{m1}^{p,T}, \ldots, \eta_{md}^{p,T})^\top$ is derived in section 4.2.2 and 4.2.3.

4.2.1 Coordinate Transformation

The boundary data $\eta_m^{p,T}$ in equation (4.2) are extracted by solving a restricted version of the PDE (2.1) on the coarse element boundary. The reduced problems derive from neglecting the terms in the original PDE with partial derivatives in the direction normal to ∂T. This needs to be done separately for the edges and faces of a coarse (tetrahedral) element and implies that $\phi_m^{p,\text{MsO}} |_{\partial T}$ is independent of the coordinate in the direction normal to ∂T. To make the construction applicable to edges and faces of $T \in \mathcal{T}_H$ which are not aligned with or perpendicular to one of the coordinate axis (see Figure 4.1), we apply a suitable coordinate transformation of the Cartesian coordinate system with basis $\{\mathbf{e}^1, \ldots, \mathbf{e}^d\}$ to a (right handed) coordinate system with orthonormal basis $\{\hat{\mathbf{e}}^1, \ldots, \hat{\mathbf{e}}^d\}$. W.l.o.g., for any

edge $\mathcal{E}$: we introduce the rotated coordinate system such that $\hat{\mathbf{e}}^1$ is parallel to $\mathcal{E}$,

face $\mathcal{F}$: we introduce the rotated coordinate system such that the normal vector $\boldsymbol{n}$ on $\mathcal{F}$ is parallel to one of the coordinate axis, i.e. w.l.o.g. $\hat{\mathbf{e}}^d = \boldsymbol{n}$ $(d = 3)$.

Let $\hat{x}_1, \ldots, \hat{x}_d$ be the coordinates of $x = (x_1, \ldots, x_d)^\top$ w.r.t. the transformed basis. The coordinate transformation can be described by a linear map $\Theta : T \to \mathbb{R}^d$, $\hat{x} = \Theta x$ with entries $\theta_{ij} = \hat{\mathbf{e}}^i \cdot \mathbf{e}^j$, $1 \le i, j \le d$. The coefficients of the elastic tensor $\hat{C}$ transform under the rotation of the coordinate system to $\hat{c}_{ijkl} = \sum_{p,q,r,s=1}^d \theta_{ip} \theta_{jq} \theta_{kr} \theta_{ls} c_{pqrs}$ (cf. [82]).

4. MULTISCALE FINITE ELEMENTS WITH OSCILLATORY BOUNDARY CONDITIONS

4.2.2 Equations Governing the Oscillatory Boundary Data

Using transformed coordinate systems as introduced in section 4.2.1, we derive the reduced problems on an edge $\mathcal{E}$ and a face $\mathcal{F}$ of $T \in \mathcal{T}_H$ for the system of anisotropic linear elasticity. The components of the elasticity operator in (2.1) read

$$\sum_{j=1}^{d} \partial_j \sigma_{ij}(\boldsymbol{u}) = \sum_{j=1}^{d} \partial_j \left(\sum_{k,l=1}^{d} c_{ijkl}\, \varepsilon_{kl}(\boldsymbol{u}) \right).$$

Forcing that $\hat{\phi}_m^{p,\mathrm{MsO}} = \hat{\eta}_m^{p,T}(\hat{x}_1, \dots, \hat{x}_{d-1})$ is independent of $\hat{x}_d$ on $\mathcal{F}$ (for $d = 3$) or $\mathcal{E}$ (for $d = 2$) and using the symmetry $\hat{c}_{ijkl} = \hat{c}_{ijlk}$ of the stiffness tensor, we obtain by using $\hat{\varepsilon}_{kl}(\hat{\boldsymbol{u}}) = \frac{1}{2}(\hat{\partial}_k \hat{u}_l + \hat{\partial}_l \hat{u}_k)$ in the rotated coordinate system

$$
\begin{aligned}
\sum_{j=1}^{d} \hat{\partial}_j \hat{\sigma}_{ij}(\hat{\eta}_m^{p,T}) \;=\;& \sum_{j=1}^{d-1} \hat{\partial}_j \left(\sum_{k,l=1}^{d} \hat{c}_{ijkl}\, \hat{\varepsilon}_{kl}(\hat{\eta}_m^{p,T}) \right) \\
=\;& \sum_{j=1}^{d-1} \hat{\partial}_j \left(\sum_{k,l=1}^{d-1} \hat{c}_{ijkl}\, \hat{\varepsilon}_{kl}(\hat{\eta}_m^{p,T}) + 2 \sum_{k=1}^{d-1} \hat{c}_{ijkd}\, \hat{\varepsilon}_{kd}(\hat{\eta}_m^{p,T}) \right) \\
=\;& \sum_{j=1}^{d-1} \hat{\partial}_j \left(\sum_{k,l=1}^{d-1} \hat{c}_{ijkl}\, \hat{\varepsilon}_{kl}(\hat{\eta}_m^{p,T}) \right) && (4.4) \\
& + \sum_{j=1}^{d-1} \hat{\partial}_j \left(\sum_{k=1}^{d-1} \hat{c}_{ijkd}\, \hat{\partial}_k \hat{\eta}_{md}^{p,T} \right). && (4.5)
\end{aligned}
$$

While equation (4.4) affects exclusively the first two components of $\hat{\eta}_m^{p,T}$, equation (4.5) acts only on the third component of the oscillatory boundary data on $\mathcal{F}$. For an anisotropic stiffness tensor, a reduced system needs to be solved on $\mathcal{F}$ in which the three components of $\hat{\eta}_m^{p,T}$ are coupled. Having a deeper look at the entries of the stiffness tensor, the systems in (4.4) and (4.5) are fully decoupled for an orthotropic material whose symmetry axes are normal to $\hat{\mathbf{e}}^1, \dots, \hat{\mathbf{e}}^d$. Particularly, the components $\hat{\eta}_{m1}^{p,T}$ and $\hat{\eta}_{m2}^{p,T}$ on $\mathcal{F}$ are then governed by a 2D system of linear elasticity (see (4.4)), while the component $\hat{\eta}_{md}^{p,T}$ normal to $\mathcal{F}$ is governed by a scalar second order elliptic PDE (see (4.5)). Analogously, on an edge $\mathcal{E}$, we can deduce that the boundary data $\hat{\eta}_m^{p,T}(\hat{x}_1)$ are governed by scalar second order PDEs in each particular component which may, again, be coupled in the anisotopic case.
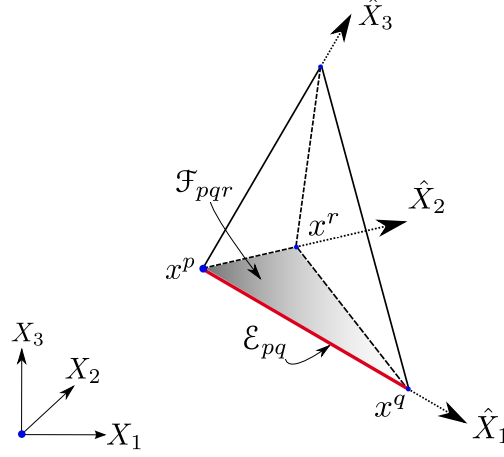
Figure 4.1: Coarse tetrahedral element with face $\mathcal{F}_{pqr}$ connecting the coarse nodes x^p, x^q and x^r (grey) and edge $\mathcal{E}_{pq}$ connecting node x^p and x^q (red); rotated orthonormal coordinate system $\hat{\mathbf{e}}^1, \hat{\mathbf{e}}^2, \hat{\mathbf{e}}^3$ with coordinates $\hat{X}_1, \hat{X}_2, \hat{X}_3$ is such that $\mathcal{F}_{pqr} \perp \hat{\mathbf{e}}^3$ and $\mathcal{E}_{pq} \parallel \hat{\mathbf{e}}^1$

4.2.3 Isotropic Linear Elasticity

Given the formulation of the reduced problems in a suitable coordinate system, we summarize the procedure of computing boundary data $\eta_m^{p,T}$ on the faces and edges of T, assuming that the stiffness tensor is isotropic. Its components are given by $c_{ijkl} = \lambda \delta_{ij} \delta_{kl} + \mu (\delta_{ik} \delta_{jl} + \delta_{il} \delta_{jk})$, where the Lamé coefficients λ and μ can be assumed to be piecewise constant in $\tau \in \mathcal{T}_h$. Note that the material coefficients are not uniquely determined on ∂T, a proper averaging (e.g. by taking their maximum values) in the adjacent elements $\tau \in \mathcal{T}_h$ is required. Due to (4.4), the reduced problem on an edge $\mathcal{E}$ in rotated coordinates reads

$$\left.\begin{aligned}
\hat{\partial}_1 \left((\lambda + 2\mu) \, \hat{\partial}_1 \hat{\eta}_{m1}^{p,T} \right) = 0 \\
\hat{\partial}_1 \left(\mu \, \hat{\partial}_1 \hat{\eta}_{mk}^{p,T} \right) = 0, \; k = 2,3
\end{aligned}\right\} \text{ on } \mathcal{E}. \tag{4.6}$$

It needs to be equipped with the vector-valued nodal constraints in (4.3). Let us assume that $\mathcal{E} = \mathcal{E}_{p_1 p_2}$ connects the two nodes $x^{p_1}, x^{p_2} \in \Sigma_H(T)$ with $x^p = x^{p_1}$, then we impose

$$\begin{aligned}
\hat{\eta}_m^{p,T}(\hat{x}^{p_1}) &= \Theta \mathbf{e}^m, \\
\hat{\eta}_m^{p,T}(\hat{x}^{p_2}) &= (0,0,0)^\top.
\end{aligned} \tag{4.7}$$

Next, we state the equations governing the reduced problem on a face $\mathcal{F}$ under the assumption that λ and μ are piecewise constant on $\mathcal{F}$. This allows to simplify the notation of the reduced system without affecting its weak formulation. According to (4.4) and (4.5), the reduced system reads

$$
\left.\begin{aligned}
\mu\,(\hat{\partial}_{11}\hat{\eta}_{m1}^{p,T} + \hat{\partial}_{22}\hat{\eta}_{m1}^{p,T}) + (\lambda+\mu)(\hat{\partial}_{11}\hat{\eta}_{m1}^{p,T} + \hat{\partial}_{12}\hat{\eta}_{m2}^{p,T}) &= 0 \\
\mu\,(\hat{\partial}_{11}\hat{\eta}_{m2}^{p,T} + \hat{\partial}_{22}\hat{\eta}_{m2}^{p,T}) + (\lambda+\mu)(\hat{\partial}_{21}\hat{\eta}_{m1}^{p,T} + \hat{\partial}_{22}\hat{\eta}_{m2}^{p,T}) &= 0 \\
\mu\,(\hat{\partial}_{11}\hat{\eta}_{m3}^{p,T} + \hat{\partial}_{22}\hat{\eta}_{m3}^{p,T}) &= 0
\end{aligned}\right\} \quad \text{on } \mathcal{F}. \tag{4.8}
$$

We deduce that the boundary data on a face $\mathcal{F}$ are governed by a reduced elasticity system in the first two components and a scalar elliptic problem in the component normal to $\mathcal{F}$. Let $\mathcal{F} = \mathcal{F}_{p_1 p_2 p_3}$ contain the coarse nodes x^{p_1}, x^{p_2} and x^{p_3}. Then the three edges $\mathcal{E}_{p_1 p_2}$, $\mathcal{E}_{p_1 p_3}$ and $\mathcal{E}_{p_2 p_3}$ form the 2D boundary of the face $\mathcal{F}$. The system in equation (4.8) is subject to the boundary conditions

$$
\hat{\eta}_m^{p,\mathcal{F}}\,|_{\mathcal{E}_{p_k p_l}} = \hat{\eta}_m^{p,\mathcal{E}_{p_k p_l}} \quad 1 \leq k < l \leq 3, \tag{4.9}
$$

where $\hat{\eta}_m^{\mathcal{E}_{p_k p_l}}$ is the solution of the BVP in (4.6) and (4.7) on the edge $\mathcal{E}_{p_k p_l}$ in the coordinate system w.r.t. $\mathcal{F}$ and $\hat{\eta}_m^{p,\mathcal{D}}$ denotes the restriction of $\hat{\eta}_m^{p,T}$ to $\mathcal{D} \subset \partial T$. Note that the rotated coordinate systems differ for any face and edge. Once the boundary data are computed on and edge or a face, they should be transformed to the original coordinate system.

4.3 Construction of the Oscillatory Multiscale-FE Basis

For the computation of the oscillatory boundary data, first, for each face $\mathcal{F}$ of $T \in \mathcal{T}_H$, boundary conditions on $\partial\mathcal{F}$ are extracted from solving lower-dimensional problems on any of their edges. The end points of an edge $\mathcal{E}$ of $\mathcal{F}$ are determined by two coarse nodes $x^q, x^{q'} \in \Sigma_H(T)$. Imposing the appropriate vector-valued boundary conditions at these end points of $\mathcal{E}$, the solution to the problem in (4.6) can be computed analytically using a line-integral, by

$$
\hat{\eta}_{mk}^{\mathcal{E}_{pq}}(\hat{x}_1) = \hat{b}_k \, \frac{\int_{x_1^q}^{\hat{x}_1} \zeta_{\lambda,\mu}^{k}{}^{-1} ds}{\int_{x_1^q}^{x_1^p} \zeta_{\lambda,\mu}^{k}{}^{-1} ds}, \tag{4.10}
$$

where $\zeta_{\lambda,\mu}^k(\hat{x}^1) = \lambda + 2\mu$ for $k = 1$ and $\zeta_{\lambda,\mu}^k(\hat{x}^1) = \mu$ for $k = 2, 3$ and $\hat{b}_k = (\Theta \mathbf{e}^m)_k$ is the boundary condition in (4.7). Again, note that the coefficients λ and μ might not be uniquely determined on any edge or face. To properly average the coefficients between adjacent elements $\tau \in \mathcal{T}_h$, we simply consider their maximum values. Having derived the oscillatory boundary conditions on all edges which form the boundary of a face $\mathcal{F}$, the reduced BVP in (4.8) can be computed using a finite element discretization on the projection of the fine mesh $\mathcal{T}_h$ onto $\mathcal{F}$ (for more details, see Algorithm 4.1).

In the following, we may omit the upper index on $\eta_m^{p,T}$ and write $\eta_m^{\mathcal{E}}$ and $\eta_m^{\mathcal{F}}$, referring to the restriction $\eta_m^{p,T}\mid_{\mathcal{D}}$ to an edge ($\mathcal{D} = \mathcal{E}$) or a face ($\mathcal{D} = \mathcal{F}$) of T. It is easy to verify from (4.6) and (4.7) that the values on the edge $\mathcal{E}_{p'q'}$ which is not connected to the coarse node $x^p \in \Sigma_H(T)$ are zero. Consequently, $\hat{\eta}^{\mathcal{E}_{p'q'}}$ only needs to be computed on edges which touch the coarse node x^p. The same holds if a face $\mathcal{F} = \mathcal{F}_{p_1 p_2 p_3}$ is not connected to the node $x^p \in \Sigma_H(T)$ where non-homogeneous Dirichlet conditions are imposed. If $p \notin \{p_1, p_2, p_3\}$, then from equation (4.8) and (4.9) we deduce that $\hat{\eta}_m^{\mathcal{F}} = 0$.

Once the boundary data are computed, the computation of the particular basis function can be done analogously to the procedure described in section 3.3, with the linear vector-valued boundary data being replaced by the oscillatory boundary data. The oscillatory multiscale finite element basis defines the coarse space

$$\mathcal{V}^{\mathrm{MsO}} = \mathrm{span}\Big\{\phi_m^{p,\mathrm{MsO}} \ : \ p \in \bar{\mathcal{N}}_H, \ m \in \{1, \ldots, d\}\Big\}. \tag{4.11}$$

Algorithm 4.1 summarizes the overall construction of the oscillatory multiscale finite element basis on a (tetrahedral) coarse mesh.

4.4 Complexity Estimate

While the number of degrees of freedom for computing a multiscale-FE basis function $\phi_m^{p,\mathrm{MsL}}$ on $T \subset \bar{\omega}_p$ is of order $O\big(d(\frac{H}{h})^d\big)$ (see chapter 3.4), extracting the boundary data for $\phi_m^{p,\mathrm{MsO}}$ only requires the solution of sparse s.p.d. linear systems of size $O\big(d(\frac{H}{h})^{d-1}\big)$. Hence, using a solver with optimal complexity $O(1)$ per unknown in the linear system, the complexity of computing an oscillatory multiscale-FE basis function is of the same asymptotic order $O\big(d(\frac{H}{h})^d\big)$ as for $\phi_m^{p,\mathrm{MsL}}$, with a small additional cost that is one order of $\frac{H}{h}$ cheaper $(O\big(d(\frac{H}{h})^d\big) + O\big(d(\frac{H}{h})^{d-1}\big))$. Thus, similar to the linear multiscale-FE

4. MULTISCALE FINITE ELEMENTS WITH OSCILLATORY BOUNDARY CONDITIONS

Algorithm 4.1: Construction of a Multiscale Finite Element Basis Function $\phi_m^{p,\mathrm{MsO}}\,|_T$ with Oscillatory Boundary Data $\eta_m^{p,T}$

Require: $T \in \mathcal{T}_H$ with vertices $\{x^{p_k} \in \Sigma_H(T) : k = 1, \ldots, n_T\}$ and $x^p = x^{p_1}$

for *any face* $\mathcal{F} = \mathcal{F}_{q_1 \ldots q_{n_{\mathcal{F}}}}$, $q_1 \neq \cdots \neq q_{n_{\mathcal{F}}} \in \{p_1, \ldots, p_{n_T}\}$ *of* T, $m \in \{1, 2, 3\}$ **do**

    for *any edge* $\mathcal{E} = \mathcal{E}_{r_1 r_2}$, $r_1 \neq r_2 \in \{q_1, \ldots, q_{n_{\mathcal{F}}}\}$ *of* $\mathcal{F}$ **do**

1. if $p \notin \{r_1, r_2\}$, set $\eta_m^{\mathcal{E}_{r_1 r_2}} = 0$ and go to next edge, else let $p = r_1$

2. set $\hat{\mathbf{e}}^1 := \frac{x^{r_1} - x^{r_2}}{\|x^{r_1} - x^{r_2}\|_2}$

3. if $\hat{\mathbf{e}}^1 \nparallel \mathbf{e}^m$, set $\hat{\mathbf{e}}^2 := \frac{\mathbf{e}^m - \langle \hat{\mathbf{e}}^1, \mathbf{e}^m \rangle_2 \hat{\mathbf{e}}^1}{\|\mathbf{e}^m - \langle \hat{\mathbf{e}}^1, \mathbf{e}^m \rangle_2 \hat{\mathbf{e}}^1\|_2}$, else $\hat{\mathbf{e}}^2 = 0$

4. average material coefficients on $\mathcal{E}$ from their values in adjacent $\tau \in \mathcal{T}_h$

5. find $\hat{\eta}_m^{\mathcal{E}}$ by solving the BVP in (4.6) and (4.7) according to (4.10)

6. form and store $\eta_m^{\mathcal{E}} := \hat{\eta}_{m1}^{\mathcal{E}} \langle \hat{\mathbf{e}}^1, \mathbf{e}^m \rangle \hat{\mathbf{e}}^1 + \hat{\eta}_{m2}^{\mathcal{E}} \langle \hat{\mathbf{e}}^2, \mathbf{e}^m \rangle \hat{\mathbf{e}}^2$

- form the transformation map $\Theta = [\hat{\mathbf{e}}^1, \hat{\mathbf{e}}^2, \hat{\mathbf{e}}^3]^\top$ for the face $\mathcal{F}$ with
  $\hat{\mathbf{e}}^1 := \frac{x^{q_2} - x^{q_1}}{\|x^{q_2} - x^{q_1}\|_2}$, $\hat{\mathbf{e}}^2 := \frac{x^{q_3} - x^{q_1} - \langle x^{q_3} - x^{q_1}, \hat{\mathbf{e}}^1 \rangle_2 \hat{\mathbf{e}}^1}{\|x^{q_3} - x^{q_1} - \langle x^{q_3} - x^{q_1}, \hat{\mathbf{e}}^1 \rangle_2 \hat{\mathbf{e}}^1\|_2}$, $\hat{\mathbf{e}}^3 := \hat{\mathbf{e}}^1 \times \hat{\mathbf{e}}^2$

- form the 2D-mesh $\mathcal{T}_h^{2\mathrm{D}}(\mathcal{F})$ on the face $\mathcal{F}$ by projecting fine elements $\tau \in \mathcal{T}_h$ onto $\mathcal{F}$ which share three vertices with the face; store the 2D coordinates of these vertices in the transformed coordinate system spanned by $\hat{\mathbf{e}}^1, \hat{\mathbf{e}}^2$. Furthermore, average the material parameters in $\tau^{2\mathrm{D}}$ using information of the adjacent elements $\tau \in \mathcal{T}_h$ which share three vertices with $\tau^{2\mathrm{D}}(\mathcal{F})$.

- following equation (4.8) and (4.9), **do**

  1. assemble and solve the 2D elasticity system for $(\hat{\eta}_{m1}^{\mathcal{F}}, \hat{\eta}_{m2}^{\mathcal{F}})^\top$, equipped with b.c. on $\mathcal{E}_{r_1 r_2} \subset \partial \mathcal{F}$, given by $(\hat{\eta}_{m1}^{\mathcal{E}_{r_1 r_2}}, \hat{\eta}_{\hat{m}2}^{\mathcal{E}_{r_1 r_2}})^\top$, where $\hat{\eta}_m^{\mathcal{E}_{r_1 r_2}} = \Theta \eta_m^{\mathcal{E}_{r_1 r_2}}$

  2. assemble and solve the 2D scalar finite element system for $\hat{\eta}_{m3}^{\mathcal{E}}$, equipped with b.c. on the edges $\mathcal{E}_{r_1 r_2} \subset \partial \mathcal{F}$, given by $\hat{\eta}_{m3}^{\mathcal{E}_{r_1 r_2}}$, where $\hat{\eta}_m^{\mathcal{E}_{r_1 r_2}} = \Theta \eta_m^{\mathcal{E}_{r_1 r_2}}$

  and store the solution $\eta_m^{\mathcal{F}} = \hat{\eta}_{m1}^{\mathcal{F}} \hat{\mathbf{e}}^1 + \hat{\eta}_{m2}^{\mathcal{F}} \hat{\mathbf{e}}^2 + \hat{\eta}_{m3}^{\mathcal{F}} \hat{\mathbf{e}}^3 = \Theta^{-1} \hat{\eta}_m^{\mathcal{F}}$

- assemble and solve the discretization of the system in (4.1) with the b.c. of (4.2), given by $\eta_m^{p,T}\,|_{\mathcal{F}} = \eta_m^{\mathcal{F}}$ for any face $\mathcal{F} \subset \partial T$

---

basis, the overall cost for the construction of the oscillatory multiscale-FE basis can be estimated to $O(d^2 e n_p)$ where e denotes the number of coarse element vertices and n_p stands for the number of nodes on the fine grid $\mathcal{T}_h$. Note that for applications in three dimensions, the complexity estimate still holds even if a sparse direct solver (cf. e.g. [3, Chapter 7]) is applied for solving the subproblems on the faces of coarse elements.

4.5 Properties

As shown in chapter 3.5, the multiscale-FE basis with vector-valued linear boundary data (MsL) recovers all the rigid body modes. Indeed, assuming constant material coefficients in the PDE, both spaces $\mathcal{V}^{\text{MsL}}$ and $\mathcal{V}^{\text{MsO}}$ recover exactly the linear vector-valued basis functions on the coarse grid $\mathcal{T}_H$. Moreover, if no material jumps occur on the boundaries of coarse elements, it can be shown that $\phi_m^{p,\text{MsO}} = \phi_m^{p,\text{MsL}}$. On general heterogeneous materials, the construction of the oscillatory multiscale basis guarantees that the rigid body translations are contained in the coarse space. This can be seen from the following arguments. Given $T \in \mathcal{T}_H$, and let us assume that the edge $\mathcal{E}$ of T connects the two nodes $x^p, x^q \in \Sigma_H(T)$. Then, due to the boundary conditions given in (4.7), (4.6) and the uniqueness of the solution, along this edge we have $\phi_{mk}^{p,\text{MsO}} \mid_{\mathcal{E}} + \phi_{mk}^{q,\text{MsO}} \mid_{\mathcal{E}} = \delta_{mk}$, $m, k \in \{1, \ldots, d\}$. Applying a similar argument shows that constants are also preserved on any face $\mathcal{F}$ of T and the PDE-harmonic extension of the constant boundary values to the coarse element interior ensures that the translations are preserved inside $T \in \mathcal{T}_H$. Since $\bar{\Omega} = \cup_{T \in \mathcal{T}_H} T$, the coarse space contains the three translations globally.

However, the construction might not guarantee that all rigid body modes are globally contained in the coarse space. For inclusions which cross coarse element boundaries, not all the rigid body rotations might be preserved as not all the rotations can be extracted from solving lower-dimensional problems. For instance, for an inclusion of high stiffness which crosses a face in the plane spanned by $\mathbf{e}^1$ and $\mathbf{e}^2$, only rotations around the axis $\mathbf{e}^3$ can be captured within the basis. Since the reduced system is obtained by neglecting terms in the PDE which have partial derivatives normal to the face, rotations around the other two axis will not occur in this specific case.

4.6   Numerical Results

In this section we present numerical examples on a binary composite. We apply vector-valued (i) linear coarse space as well as multiscale-FE coarse spaces with (ii) linear and (iii) oscillatory boundary conditions. We perform the simulations on a domain $\bar{\Omega} = [0,1] \times [0,1] \times [0,L], L > 0$, with regular fine and coarse triangular mesh $\mathcal{T}_h$ and $\mathcal{T}_H$ of equal structure with uniform mesh size h and H, respectively. Both meshes are constructed from an initial voxel geometry as described in chapter 2.3.2. In the numerical test we show condition numbers as well as iteration numbers of the PCG algorithm. The stopping criterion is set to reduce the preconditioned initial residual by six orders of magnitude.

The medium consists of an isotropic matrix material with coefficients $\mu_{mat} = 1$ and $\lambda_{mat} = 1$ and contains inclusions which are positioned equally in each coarse block of size $H \times H \times H$ as shown in Figure 4.2. The distribution of the inclusions as well as
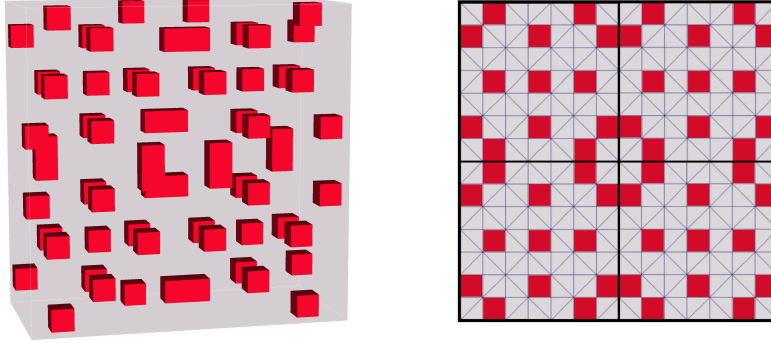
Figure 4.2: Binary composite; matrix material (grey) and inclusions (red); discretization in $14 \times 14 \times 7$ voxels (left); 2D-projection onto the (X_1, X_2)-plane with position of the inclusion (right); each coarse block is decomposed in five tetrahedra

the boundaries of the coarse tetrahedra are shown in more detail in Figure 4.3. At each slice in the plane normal to X_1 and X_2, the position of the inclusions above and below this level are indicated in dark and shaded red, respectively. Each inclusion touches or crosses coarse element boundaries while one inclusion in the center is isolated in the interior of a coarse element. Under the variation of the material contrast $\Delta_E := \mu_{inc}/\mu_{mat} = \lambda_{inc}/\lambda_{mat}$, Table 4.1 shows the condition and iteration numbers for the three coarsening strategies. For $\Delta_E > 1$, condition and iteration numbers for vector-valued linear and multiscale-FE coarse space with linear boundary conditions grow with
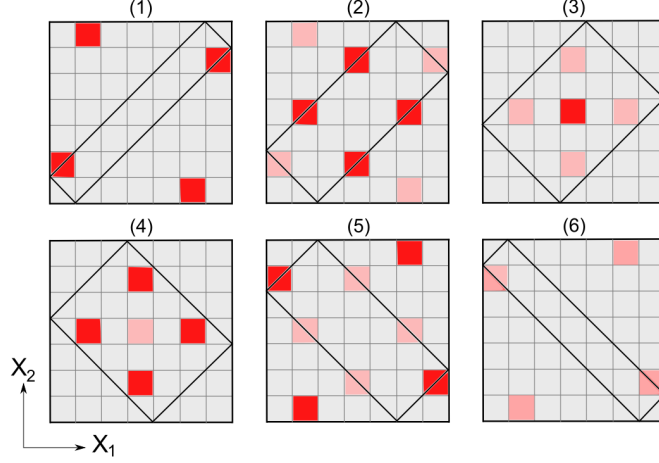
Figure 4.3: $2D$-slices (at $X_3 = l\,h$, $l \in \{1, \ldots, 6\}$) of a coarse block of $7 \times 7 \times 7$ voxels of the medium in Figure 4.2 ; boundaries of coarse tetrahedral elements (black), matrix material (grey) and 1x1x1 inclusions (red); inclusions touch the slice from below (shaded red) or top (dark red); inclusions touch coarse element boundaries

the contrast in the material coefficients, the latter does not perform noticeably better than the linear coarse space. The multiscale coarse basis functions with oscillatory boundary conditions are bounded in energy and show coefficient-independent bounds of the condition number. For $\Delta_E < 1$, each coarse space performs well.

	Lin		MsL		MsO	
Δ_E	n_{it}	$\kappa(M_{AS}^{-1}A)$	n_{it}	$\kappa(M_{AS}^{-1}A)$	n_{it}	$\kappa(M_{AS}^{-1}A)$
10^{-9}	28	26	28	26	28	26
10^{-6}	28	26	28	26	28	26
10^{-3}	28	26	28	26	28	26
10^{0}	27	25	27	25	27	25
10^{3}	91	426	76	233	27	25
10^{6}	102	965	104	955	27	25
10^{9}	102	970	104	955	27	25

Table 4.1: Iteration numbers Condition numbers n_{it} and iteration numbers κ of precond. matrix for $H = 7h$, $\delta = 2h$

4.7 Conclusions

In this chapter, we extend the oscillatory multiscale finite element method as introduced in [53] to the PDE system of anisotropic linear elasticity. We derive the reduced system which governs the oscillatory boundary data in a general setting which allows their construction on triangular, tetrahedral, quadrilateral and hexahedral coarse meshes. We apply the coarse basis in the context of two-level additive Schwarz domain decomposition preconditioners. Numerical results are presented on a tetrahedral mesh for isotropic composites where stiff inclusions touch and cross coarse element boundaries. We observe condition number bounds of the preconditioned linear system which are independent of the contrast in the Young's modulus of the inclusions.

It is easy to verify (see chapter 3.4) that the computation of a multiscale finite element basis is more costly on quadrilateral and hexahedral coarse meshes than on their triangular and tetrahedral counterparts (by a factor of $\frac{4}{3}$ in 2D and a factor of 2 in 3D). However, we may point out that, especially for applications in three spatial dimensions, using hexahedral coarse meshes may be beneficial for the robustness of the overall method as it reduces the amount of element boundaries which are introduced when tetrahedral coarse meshes are used.

5

Energy Minimizing Coarse Spaces

In this chapter we construct coarse basis functions with a minimal energy property subject to pointwise constraints which ensure that the coarse space exactly contains the rigid body translations, while the rigid body rotations are preserved approximately. Energy minimizing methods with pointwise constraints, often referred to as trace-minimization, have been proposed first in [78] and [105] and were further investigated in [98, 110] and [83]. Applications to isotropic linear elasticity are already provided in [78], in the context of smoothed aggregation. The novel part here is the application to the multiscale framework. It was shown in [110] that coarse spaces constructed by explicit energy minimization share similarities with multiscale finite element basis functions in the sense that the basis functions are locally PDE-harmonic in the interior of coarse elements. Hence, since the construction on a coarse tetrahedral mesh as introduced in chapter 2.3 allows large overlaps in the supports of the basis functions, an energy minimizing coarse space obeys multiscale features similar to the coarse spaces considered in the two previous chapters.

The construction of the basis functions requires the solution of additional global problems whose solutions implicitly form the counterpart to the vector-valued linear or oscillatory boundary conditions of the multiscale finite element basis. We also study how these so called Lagrange multiplier systems can be solved efficiently by constructing preconditioners as proposed in [98] for scalar elliptic PDEs.

The chapter is organized as follows. Summarizing useful notations in section 5.1, we proceed with introducing the energy minimizing basis and the corresponding multiscale coarse space in section 5.2. Section 5.3 is concerned with the precise construction of the energy minimizing basis functions. A complexity estimate and details of the coarse space properties are stated in section 5.4 and 5.5, respectively. Furthermore, we provide in section 5.6 a detailed definition of the interpolation operators which are formed by the coarse basis. Moreover, we show how the basis functions can be computed robustly in section 5.7 by applying robust preconditioners to the so called Lagrange multiplier system which arises from the energy minimizing construction. Section 5.8 is devoted to numerical results in 3D, a short discussion in section 5.9 finalizes the chapter.

5.1 Preliminaries

We are again in the setting of chapter 2. Using the discretization introduced in section 2.2, we refer to the notations related to the fine and coarse meshes and respective degrees of freedoms as summarized in section 2.6.

5.2 Multiscale Coarsening by Energy Minimization

We construct the energy minimizing coarse space $\mathcal{V}^{\mathrm{EM}}$ on $\mathcal{T}_H$ according to Assumption 2.4.1. We denote by $|\cdot|_{a,\Omega}$ the semi-norm on $[H^1(\Omega)]^d$, induced by the bilinear form in (2.8). For each $m \in \{1, \ldots, d\}$ and $p \in \bar{\mathcal{N}}_H$, we construct a basis function

$$\phi_m^{p,\mathrm{EM}} : \omega_p \to \mathbb{R}^d.$$

Ensuring that the three translations are exactly contained in the coarse space, the construction is done separately for $m \in \{1, \ldots, d\}$, such that

$$\sum_{p \in \bar{\mathcal{N}}_H} |\phi_m^{p,\mathrm{EM}}|_{a,\Omega}^2 \to \ \min \tag{5.1}$$

$$\text{subject to} \sum_{p \in \bar{\mathcal{N}}_H} \phi_{mk}^{p,\mathrm{EM}} = \delta_{mk} \quad k = 1, \ldots, d, \ \text{in } \Omega. \tag{5.2}$$

Thus, the basis is constructed such that the coarse basis preserves the translations exactly. The rigid body rotations are contained approximately. The given functions

are linearly independent and the basis satisfies Assumption 2.4.1 *(C1) - (C4)*. We define the coarse space by

$$\mathcal{V}^{\mathrm{EM}} := \mathrm{span}\Big\{ \phi_m^{p,\mathrm{EM}} : p \in \bar{\mathcal{N}}_H,\, m = 1, \ldots, d \Big\}.$$

Note that we define the subspace $\mathcal{V}_0^{\mathrm{EM}} \subset \mathcal{V}^{\mathrm{EM}}$ as the subspace which contains only basis functions which correspond to coarse nodes $x^p \in \bar{\Sigma}_H$ which do not touch the global Dirichlet boundary. Furthermore, we exclude any fine grid degrees of freedom on the boundary $\Gamma_{D_i}, i = 1, \ldots, d$, when constructing the interpolation operator. More details are given in section 5.6. In the following, we give a constructive proof for the existence and uniqueness of the solution of the minimization problem in (5.1) and (5.2). Therefore, we denote by $\bar{A} \in \mathbb{R}^{n_d \times n_d}$ the global stiffness matrix where no essential boundary conditions are applied. The entries of $\bar{A}$ are determined by (2.13). We set $\mathcal{V}^h(\omega_p) := \{\varphi \in \mathcal{V}^h : \mathrm{supp}(\varphi) \subset \bar{\omega}_p\}$ and denote by R_p the matrix describing the restriction to degrees of freedom in $\mathcal{V}^h(\omega_p)$ of a vector which corresponds to degrees of freedom in $\mathcal{V}^h$. The principal submatrix of $\bar{A}$ is then given by $\bar{A}_p = R_p \bar{A} R_p^\top$. Note that $\bar{A}_p$ is non-singular for any suitable R_p. Furthermore, let $\mathbf{1}^m \in \mathbb{R}^{n_d}$ be the coefficient vector in terms of the fine-scale basis of $\mathcal{V}^h$ which represents a rigid body translation in the unknown $m \in \{1, \ldots, d\}$.

Theorem 5.2.1. *The solution of the minimization problem in* (5.1) *and* (5.2) *on the space* $\mathcal{V}^h$ *is given by*

$$\Phi_m^{p,\mathrm{EM}} = R_p^\top \bar{A}_p^{-1} R_p \Lambda_m, \tag{5.3}$$

where $\Lambda_m \in \mathbb{R}^{n_d}$ *is the vector of Lagrange multipliers, which satisfies*

$$\sum_{p \in \bar{\mathcal{N}}_H} R_p^\top \bar{A}_p^{-1} R_p \Lambda_m = \mathbf{1}^m.$$

Proof. The minimization problem couples the quadratic objective function in (5.1) with linear constraints, given in (5.2). Introducing the *Lagrange multiplier* [7] Λ_m, a solution can be found by the extrema of the quadratic Lagrange functional

$$\mathcal{L}_m\Big(\{\Phi_m^{p,\mathrm{EM}}\}, \Lambda_m \Big) = \frac{1}{2} \sum_{p \in \bar{\mathcal{N}}_H} \Phi_m^{p,\mathrm{EM}\top} \bar{A}\, \Phi_m^{p,\mathrm{EM}} \ - \ \Lambda_m^\top \Bigg(\sum_{p \in \bar{\mathcal{N}}_H} \Phi_m^{p,\mathrm{EM}} - \mathbf{1}^m \Bigg).$$

We enforce an additional constraint on the support of the basis functions by substituting $\Phi_m^{p,\mathrm{EM}} = R_p^\top \hat{\Phi}_m^{p,\mathrm{EM}}$. The vector $\hat{\Phi}_m^{p,\mathrm{EM}}$ can be interpreted as the local representation of $\Phi_m^{p,\mathrm{EM}}$ on its support $\bar{\omega}_p$ in terms of the basis of $\mathcal{V}^h(\omega_p)$. To find the critical point of this functional we impose $\nabla_{\Lambda_m}\mathcal{L}_m = 0$ and $\nabla_{\hat{\Phi}_m^{p,\mathrm{EM}}}\mathcal{L}_m = 0$, which results in the saddle point problem

$$
\bar{A}_p \hat{\Phi}_m^{p,\mathrm{EM}} - R_p \Lambda_m \;=\; 0 \quad \forall\, p \in \bar{\mathcal{N}}_H, \tag{5.4}
$$

$$
\sum_{p \in \bar{\mathcal{N}}_H} R_p^\top \hat{\Phi}_m^{p,\mathrm{EM}} - \mathbf{1}^m \;=\; 0. \tag{5.5}
$$

From equation (5.4), we conclude

$$
\hat{\Phi}_m^{p,\mathrm{EM}} = \bar{A}_p^{-1} R_p \Lambda_m \quad \forall\, p \in \bar{\mathcal{N}}_H. \tag{5.6}
$$

Substituting equation (5.6) into (5.5) yields

$$
\mathbf{1}^m = \sum_{p \in \bar{\mathcal{N}}_H} R_p^\top \bar{A}_p^{-1} R_p \Lambda_m.
$$

We introduce $\bar{L} := \sum_{p \in \bar{\mathcal{N}}_H} R_p^\top \bar{A}_p^{-1} R_p$ and obtain for $m \in \{1, \ldots, d\}$,

$$
\Lambda_m = \bar{L}^{-1} \mathbf{1}^m. \tag{5.7}
$$

$\square$

Thus, to compute the basis of minimal energy, we have to solve a global Lagrange multiplier system in (5.7) for each $m \in \{1, \ldots, d\}$ and solve local subproblems in (5.6) to compute the particular basis functions.

5.3 Construction of the Energy Minimizing Basis

The Local Construction: First, we shortly describe how to compute a single coarse basis function. We fix $m \in \{1, \ldots, d\}$ and $p \in \bar{\mathcal{N}}_H$ and assume that the Lagrange multiplier Λ_m is already known. By construction, the set $\bar{\omega}_p$ consists of a union of fine elements $\bar{\omega}_p = \cup\{\tau_i\}_{i=1}^{n_T}$ in $\mathcal{T}_h$. The entries of the global Neumann matrix $\bar{A}$ are defined by $\bar{A}_{(i,k)(j,l)} = a(\varphi_k^{i,h}, \varphi_l^{j,h})$ for all $(i,k),(j,l) \in \mathcal{D}_h$ and $\bar{A}$ is symmetric positive semi-definite with $\mathrm{Ker}(\bar{A}) = \mathcal{RBM}(\bar{\Omega})$. The coefficient vector $\Phi_m^{p,\mathrm{EM}} = R_p^\top \hat{\Phi}_m^{p,\mathrm{EM}}$ respresenting the energy minimizing basis function in terms of the basis of $\mathcal{V}^h$ can be

computed from $\bar{A}_p \hat{\Phi}_m^{p,\mathrm{EM}} = R_p \Lambda_m$, where Λ_m is the Lagrange multiplier given in (5.7). The solution $\Phi_m^{p,\mathrm{EM}}$ of the linear system defines the solution of the minimization problem in (5.1) and (5.2), discretized on the space $\mathcal{V}^h$. The basis function reads

$$\phi_m^{p,\mathrm{EM}} = \sum_{(j,k) \in \mathcal{D}_h(\bar{\Omega})} \Phi_{m,(j,k)}^{p,\mathrm{EM}} \, \varphi_k^{j,h}.$$

The Overall Construction: The procedure for the construction of the energy minimizing basis is as follows: For $m = 1, \ldots, d$, the following applies:

1. Solve the Lagrange multiplier system $\bar{L}\Lambda_m = \mathbf{1}^m$ (see equation (5.7)), using the (P)CG algorithm:

   - in each (P)CG iteration, compute the action of L to a given iterate $\mathbf{v_k}$ by summing over the terms $R_p^\top \hat{\mathbf{x}}_k$, $p = 1, \ldots, N_p$, where $\hat{\mathbf{x}}_k$ is the solution of the local systems $\bar{A}_p \hat{\mathbf{x}}_k = R_p \mathbf{v}_k$.

2. For each $p \in \bar{\mathcal{N}}_H$, the following applies:

   - compute $\phi_m^{p,\mathrm{EM}} : \omega_p \to \mathbb{R}^d$ w.r.t. the fine-scale discretization. That is, solve the linear system $\bar{A}_p \hat{\Phi}_m^{p,\mathrm{EM}} = R_p \Lambda_m$. The components of $\Phi_m^{p,\mathrm{EM}} = R_p^\top \hat{\Phi}_m^{p,\mathrm{EM}}$ define the rows in the matrix $\bar{R}$ as given in equation (5.8).

5.4 Complexity Estimate

The complexity estimate for the construction of the energy minimizing basis can be given as follows. Solving the linear system in equation (5.6) requires for $m = 1, \ldots, d$, and any $p \in \bar{\mathcal{N}}_H$ the solution of a local linear system. Under the idealized assumption of applying a solver with optimal order complexity, the total cost can be estimated to be of order $O\big(d^2 e N_p (\frac{H}{h})^d\big) = O(d^2 e n_p)$, where e is the number of coarse element vertices. This estimate yields equal order complexity than the overall construction of the multiscale finite element basis (see section 3.4 and 4.4). However, note that energy minimizing construction requires inversions on the entire $\bar{\omega}_p$ while the multiscale-FE spaces require only local inversions on any $T \subset \bar{\omega}_p$. Additionally, solving the Lagrange multiplier system in equation (5.7) needs the inversion of the local submatrices within any (P)CG iteration. The overall complexity of solving the Lagrange multiplier system

can be computed analogously and is of equal order $O(d^2 e n_p)$. However, it introduces a larger constant which is proportional to the number of iterations of the (P)CG-algorithm. In practical applications, solving the Lagrage multiplier system with an accuracy of three orders of magnitude has proven to be sufficient and requires at least $7 - 10$ (P)CG iterations. Thus, altough both methods have equal order complexity when optimal local solvers are used, computing the energy minimizing coarse basis is, by a small factor, more costly than computing a multiscale finite element basis.

5.5 Properties

As we can conclude from the construction, the coarse space contains the rigid body translations globally in $\bar{\Omega}$. However, it is not obvious to see how well the coarse space approximates the set of rigid body rotations. The rotations are, in general, not exactly contained in $\mathcal{V}^{\mathrm{EM}}$. Energy minimizing constructions of basis functions allow quite general supports and the method is easily applicable to unstructured meshes (cf. [104, 110]). Denoting by $\omega_p^{\mathrm{int}} := \{x \in \omega_p : x \notin \omega_q \text{ for } q \neq p\}$ the subset of ω_p which is not overlapped with the support of any other basis function, it is clear that rigid body rotations cannot be globally contained in the coarse space as long as $\mathrm{meas}(\omega_p^{\mathrm{int}}) > 0$. Thus, to ensure that the presented construction of the coarse space allows an adequate approximation of the rigid body rotations, a necessary requirement needs to be stated on the supports of the basis functions. Defining the coarse basis functions on the coarse mesh $\mathcal{T}_H$ as introduced before yields large overlaps in the supports of neighboring basis functions. It holds $\omega_p^{\mathrm{int}} = \{x^p\}$ and thus, we obtain $\mathrm{meas}(\omega_p^{\mathrm{int}}) = 0$. However, this criterion is not sufficient to ensure that all the rigid body rotations are preserved exactly by the coarse space. Indeed, the quality of the approximation may even depend on the underlying mesh itself.

An important property, showing the multiscale character of the presented energy minimizing coarse space, is summarized in the following. We show that the Lagrange multipliers $\Lambda_m, m = 1, \ldots, d$, are supported exclusively on the coarse element boundaries and thus, the energy minimizing basis functions are given by a discrete PDE-harmonic extension of local boundary data. Before proving this statement, we introduce the

following notation. For $T \in \mathcal{T}_H$, let

$$\text{range}(T) := \bigcap_{p \in \mathcal{N}_H(T)} \text{range}(R_p^\top)$$

be the set of vectors in $\mathbb{R}^{n_d}$ which correspond to functions in $\mathcal{V}^h$ which are supported in the interior of $T \subset \bar{\Omega}$. We show that the Lagrange multiplier Λ_m, $m = 1, \ldots, d$ has non-zero values only in a set which is complementary to $\{\text{range}(T) : T \in \mathcal{T}_H\}$. The entries which are non-zero correspond to fine basis functions which are supported along the boundaries of coarse elements.

Lemma 5.5.1. *Let* $m \in \{1, \ldots, d\}$ *be fixed and let* $\Lambda_m = \bar{L}^{-1} \mathbf{1}^m$. *Then for each* $T \in \mathcal{T}_H$, *we have*

$$\xi^\top \Lambda_m = 0 \quad \forall \xi \in range(T).$$

Proof. Let $n_T = \#\{p \in \mathcal{N}_H(T)\}$ be the number of vertices of T. For $m \in \{1, \ldots, d\}$, it holds

$$\sum_{p \in \mathcal{N}_H(T)} \Phi_{mk}^{p,\text{EM}} = \delta_{mk} \quad \text{on } T, \ k \in \{1, \ldots, d\}.$$

For each $\xi \in \text{range}(T)$, let $\hat{\xi}_p := R_p \xi$, $p \in \mathcal{N}_H(T)$ be the local representation of ξ in $\omega_p \subset \Omega$. Note that it also holds $R_p^\top \hat{\xi}_p = \xi$ since ξ_p is supported in $\text{range}(R_p^\top)$ by assumption. Moreover, we have by equation (5.4),

$$n_T \, \xi^\top \Lambda_m = \sum_{p \in \mathcal{N}_H(T)} \hat{\xi}_p^\top R_p \Lambda_m = \sum_{p \in \mathcal{N}_H(T)} \hat{\xi}_p^\top \bar{A}_p \hat{\Phi}_m^{p,\text{EM}} = \xi^\top \bar{A} \mathbf{1}^m = 0,$$

where we used $\xi \in \text{range}(T)$ twice. The last equality follows since $\mathbf{1}^m \in \text{Ker}(\bar{A})$. $\qquad\square$

This shows that the basis functions are locally PDE-harmonic, a well known property of energy minimizing bases (cf. [110]). From the solution of the Lagrange multiplier system, optimal boundary conditions for the local basis functions are extracted on $\{\partial T, T \in \mathcal{T}_H\}$. It is obvious that the energy minimizing basis functions are continuous along the boundaries of the coarse elements and lead to a conforming coarse space.

5.6 Interpolation Operator

In the following, we form the interpolation operator which is obtained from the energy minimizing coarse space. We refer to the summary of notations in section 2.6 to recall notations of fine and coarse nodes and related degrees of freedom. We use the fine scale representation of a coarse basis function $\phi_m^{p,\text{EM}}$ to define the interpolation operator, respectively the restriction operator. Each energy minimizing basis function omits the representation

$$\phi_m^{p,\text{EM}} = \sum_{k=1}^{d} \sum_{i=1}^{n_p} \bar{r}_{(p,m)(i,k)} \varphi_k^{i,h}. \tag{5.8}$$

This representation defines a matrix $\bar{R} \in \mathbb{R}^{N_d \times n_d}$ which contains the coefficient vectors, representing a coarse basis function in terms of the fine scale basis, by rows. The restriction operator R_H, which we use in the additive Schwarz algorithm is then constructed as a submatrix of $\bar{R}$, which contains only the rows corresponding to coarse basis functions which vanish on the global Dirichlet boundaries Γ_{D_i}, $i = 1, \ldots, d$ and do not contain any fine degrees of freedom on the global Dirichlet boundary. Denoting the entries of R_H by $(r_{p'j'})_{p',j'}$, we define

$$r_{p'j'} = \begin{cases} \bar{R}_{p'j'} & \text{if } p' \in \mathcal{D}_H(\Omega^*), \ j' \in \mathcal{D}_{h,0}(\bar{\Omega}), \\ 0 & \text{if } p' \in \mathcal{D}^H(\Omega^*), \ j' \in \mathcal{D}_{h,\Gamma_D}(\bar{\Omega}), \end{cases}$$

where $\mathcal{D}_H(\Omega^*)$, $\Omega^* := \bar{\Omega} \backslash (\cup^i \Gamma_{D_i})$ denotes the coarse interior degrees of freedom in Ω^*. The matrix representing the interpolation from the coarse space $\mathcal{V}_0^{\text{EM}}$ to the fine space $\mathcal{V}_0^h$ is simply given by $R_H^\top$ and the coarse stiffness matrix can be computed by the Galerkin product $A^H = R_H A R_H^\top$.

5.7 Preconditioning the Lagrange Multiplier System

As we have seen, in order to compute the energy minimizing basis functions, a global Lagrange multiplier system has to be solved for each $m \in \{1, \ldots, d\}$. We solve these systems using the PCG algorithm. To ensure that the overall cost of the method, including the setup of the energy minimizing basis as well as the application of the two-level additive Schwarz preconditioner, does not grow with the contrast in the material co-

efficients, we apply a preconditioner for the Lagrange multiplier system which allows to robustly compute the Lagrange multipliers independently of variations in mesh and material parameters. Different such preconditioners are studied in the literature for finite element discretizations of scalar PDEs. They are summarized in [98] where their robustness properties are also studied numerically. As presented in [110], a diagonal preconditioner is sufficient to achieve robustness when applied in the context of AMG, where small coarsening factors $c_f \approx 2$ are used to generate the coarser elements. However, the results in [98] show that robustness may be lost when the supports ω_p of the basis functions are large. Therefore, the authors in [98] apply a one-level additive Schwarz preconditioner for the Lagrange multiplier system and show its robustness and performance numerically. In the following, we apply this preconditioner to linear elasticity problems, i.e. we present a one-level additive Schwarz preconditioner as proposed before in [98] for the Lagrange multiplier system

$$\bar{L} = \sum_{p \in \bar{\mathcal{N}}_H} R_p^\top \bar{A}_p^{-1} R_p.$$

Note that, once the stiffness matrix and the restriction operators are defined, the construction is equivalent for scalar elliptic and vector-valued problems. To apply a one-level additive Schwarz preconditioner for $\bar{L}$, we introduce the local submatrix $\bar{L}_p$ describing the action of $\bar{L}$ when restricted from $\bar{\Omega}$ to ω_p, by

$$\bar{L}_p = R_p \bar{L} R_p^\top.$$

The one-level additive Schwarz preconditioner $\bar{Q}_{1\mathrm{AS}}^{-1}$ to $\bar{L}$ is then given by

$$\bar{Q}_{1\mathrm{AS}}^{-1} = \sum_{p \in \bar{\mathcal{N}}_H} R_p^\top \bar{L}_p^{-1} R_p. \tag{5.9}$$

In the following, we show that the preconditioner in (5.9) can be applied efficiently without explicitely forming the dense matrices $\bar{L}_p$. To simplify the illustration, let us first assume that the domain ω_p is overlapped by only two others, ω_l and ω_r. Thus, it holds $R_{p \leftarrow q} := R_p R_q^\top \neq 0$ if and only if $q \in \{l, r, p\}$ and it is $R_{p \leftarrow q}^\top = (R_p R_q^\top)^\top = R_q R_p^\top = R_{q \leftarrow p}$. Furthermore, we have $R_{p \leftarrow p} = R_p R_p^\top = I_p$ where I_p denotes the matrix

representing the identity mapping on $\mathcal{V}^h(\omega_p)$. Thus, we obtain

$$
\begin{aligned}
\bar{L}_p &= R_p \bigg(\sum_{q \in \bar{\mathcal{N}}_H} R_q^\top \bar{A}_q^{-1} R_q \bigg) R_p^\top \\
&= \bar{A}_p^{-1} + \begin{bmatrix} R_{p\leftarrow l} & R_{p\leftarrow r} \end{bmatrix} \begin{bmatrix} \bar{A}_l^{-1} & \\ & \bar{A}_r^{-1} \end{bmatrix} \begin{bmatrix} R_{l\leftarrow p} \\ R_{r\leftarrow p} \end{bmatrix}.
\end{aligned}
$$

To obtain the inverse of $\bar{L}_p$, we apply a Woodbury matrix identity. We substitute

$$
B \leftrightarrow \bar{A}_p, \quad X \leftrightarrow \begin{bmatrix} R_{p\leftarrow l} & R_{p\leftarrow r} \end{bmatrix}, \quad C \leftrightarrow \begin{bmatrix} \bar{A}_l & \\ & \bar{A}_r \end{bmatrix},
$$

and use a Sherman-Morrison-Woodbury formula [88, Sec.2.7] in the form

$$
(B^{-1} + XC^{-1}X^\top)^{-1} = B - BX(C + X^\top BX)^{-1}X^\top B.
$$

We obtain

$$
\bar{L}_p^{-1} = \bar{A}_p - \bar{A}_p \begin{bmatrix} R_{p\leftarrow l} & R_{p\leftarrow r} \end{bmatrix} \bar{J}_p^{-1} \begin{bmatrix} R_{l\leftarrow p} \\ R_{r\leftarrow p} \end{bmatrix} \bar{A}_p,
$$

where

$$
\bar{J}_p = \begin{bmatrix} \bar{A}_l & \\ & \bar{A}_r \end{bmatrix} + \begin{bmatrix} R_{l\leftarrow p} \\ R_{r\leftarrow p} \end{bmatrix} \bar{A}_p \begin{bmatrix} R_{p\leftarrow l} & R_{p\leftarrow r} \end{bmatrix}.
$$

Now we consider the general case where n_s basis functions have an intersecting support with ω_p. Let $q_1, \ldots, q_{n_s}$ be such that $\omega_p \cap \omega_{q_i} \neq \emptyset$, $\omega_p \neq \omega_{q_i}$, $i = 1, \ldots, n_s$. We introduce

$$
R_{p\leftarrow \{q\}} := \begin{bmatrix} R_{p\leftarrow q_1} & \cdots & R_{p\leftarrow q_{n_s}} \end{bmatrix}.
$$

Then we set, for the general case,

$$
\bar{J}_p := \mathrm{diag}(\bar{A}_{q_1}, \ldots, \bar{A}_{q_{n_s}}) + R_{p\leftarrow \{q\}} \bar{A}_p R_{p\leftarrow \{q\}}^\top \tag{5.10}
$$

and obtain

$$
\bar{L}_p^{-1} = \bar{A}_p - \bar{A}_p R_{p\leftarrow \{q\}} \bar{J}_p^{-1} R_{p\leftarrow \{q\}}^\top \bar{A}_p. \tag{5.11}
$$

Hence, the action of $\bar{L}_p^{-1}$ can be applied efficiently to a vector without forming the dense matrix $\bar{L}_p$. According to (5.11), it involves sparse matrix-vector multiplications and requires solving a linear system which is determined by the sparse matrix in (5.10). Figure 5.1 illustrates the support in which the action of $\bar{L}_p^{-1}$ applies.
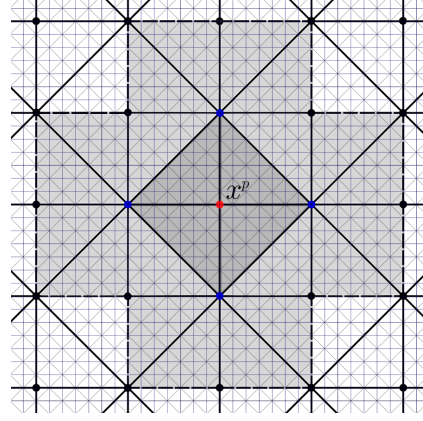
Figure 5.1: Example of fine and coarse mesh in 2D indicating the support $\bar{\omega}_p$ (dark grey) of a coarse basis function and the supports $\{\bar{\omega}_q, \omega_q \cap \omega_p \neq \emptyset\}$ of neighboring basis functions (light grey)

Next, we numerically test the robustness of the one-level additive Schwarz preconditioner in (5.9) for the Lagrange multiplier system in (5.7). We consider heterogeneous

(a) 0.25 VP   (b) 1 VP   (c) 5 VP   (d) 10 VP
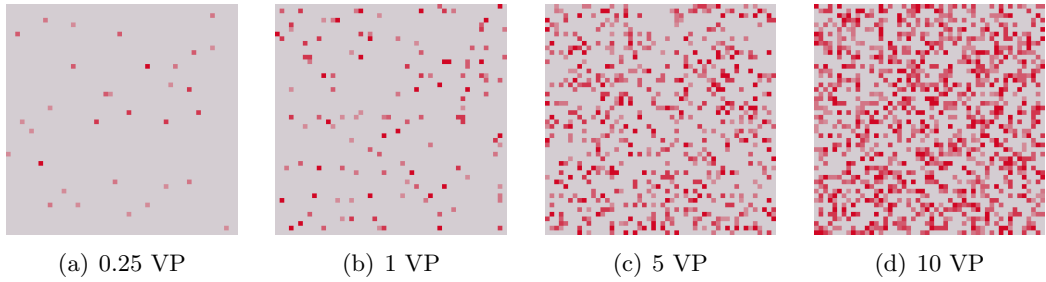
Figure 5.2: 2D-projections of random media, discretized with $50 \times 50 \times 5$ voxels; small inclusions uniformly distributed in matrix material for different volume fractions: $0.25 - 10.0$ volume percent (VP); darker color indicates that inclusion is positioned in a higher voxel-layer of the 3D microstructure

media of different coefficient distributions in $\bar{\Omega} = [0,1] \times [0,1] \times [0,2]$. Figure 5.2 shows 2D projections of such media in 3D, small inclusions are uniformly distributed in a

matrix material for different volume fractions. Matrix material and inclusions are both isotropic, the material parameters are set to $\mu_{\mathrm{mat}} = 3$, $\lambda_{\mathrm{mat}} = 2$ and $\mu_{\mathrm{mat}} = 3\Delta_E$, $\lambda_{\mathrm{inc}} = 2\Delta_E$ and Δ_E varies over several orders of magnitude.

On these media, we solve the Lagrange multiplier system $\bar{L}$ in equation (5.7) with the one-level additive Schwarz preconditioner presented in (5.9) for fixed mesh parameters. For comparison, we also apply a diagonal preconditioner to $\bar{L}$.

Table 5.1 shows the PCG-iteration numbers needed to solve the Lagrange multiplier system by reducing the preconditioned initial residual by three orders of magnitude. The given accuracy has shown to be fully sufficient for the construction of the basis functions. Applying the one-level additive Schwarz preconditioner to the Lagrange

$\Delta_E \setminus$ VP	Diagonal precond.				1-Level AS			
	0.25	1	5	10	0.25	1	5	10
10^0	12	12	12	12	7	7	7	7
10^3	24	43	111	124	8	8	10	11
10^6	13	15	200^+	200^+	8	8	10	11
10^9	13	15	200^+	200^+	8	8	9	11

Table 5.1: PCG iteration numbers for solving the Lagrange multiplier system using diagonal and one-level additive Schwarz preconditioner

multiplier system, the numerical results show constant iteration numbers, independent of the coefficient distribution and the magnitude of the discontinuities in the Young's modulus. The method allows a robust construction of the energy minimizing basis. Using a diagonal preconditioner, the iteration numbers act very sensitive to coefficient variations. We can say that the additive Schwarz preconditioner as proposed before in [98] is robust w.r.t. the contrast in the coefficients also when applied to linear elasticity problems.

5.8 Numerical Results

Following the numerical tests for the multiscale finite element coarse space in chapter 3.7, we give a series of examples involving binary media, showing the performance of the energy minimizing preconditioner under variations of the mesh parameters as well as the material coefficients. Additionally, we measure the approximation error of the energy minimizing coarse space to a fine scale solution. In each experiment, the energy

minimizing coarse space is compared with a standard linear coarse space. We perform simulations on the domain $\bar{\Omega} = [0, 1] \times [0, 1] \times [0, L], L > 0$ consisting of different heterogeneous media, with fine and coarse mesh as introduced in section 2.3.2. Figure 5.3 shows a binary medium with isolated inclusions, one inclusion is located inside each coarse tetrahedra. The inclusions of the second binary medium, given in Figure 5.4, are identically distributed. In the subsequent parts, we refer to the binary medium where inclusions are isolated in the interior of coarse elements as medium 1.
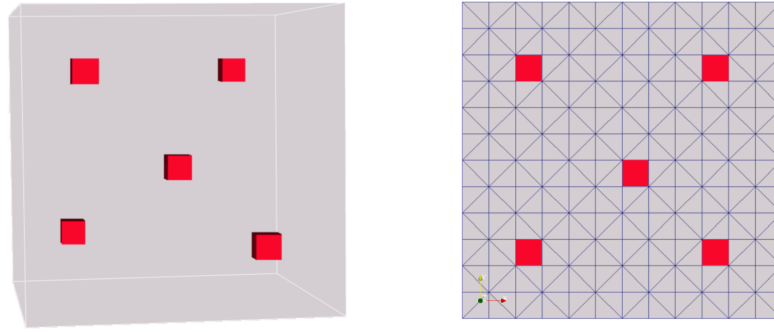
Figure 5.3: Medium 1: binary composite; matrix material (grey) and $1 \times 1 \times 1$ inclusions (red); discretization in $12 \times 12 \times 12$ voxels; each voxel is decomposed in 5 tetrahedra; $3D$ view (left) and 2D projection with fine mesh, showing the position of the inclusions (right); inclusions in the interior of coarse tetrahedral elements

The medium with identically distributed inclusions is referred to as medium 2. For both media, the Young's modulus E as well as Poisson ratio ν for matrix material and inclusions are given in Table 5.2. The contrast $\Delta_E := E_{inc}/E_{mat}$ may vary over several orders of magnitude.

Young's modulus	Poisson ratio
$E_{\mathrm{mat}} = 1$ MPa	$\nu_{\mathrm{mat}} = 0.2$
$E_{\mathrm{inc}} = \Delta_E E_{\mathrm{mat}}$	$\nu_{\mathrm{inc}} = 0.2$

Table 5.2: Young's Modulus and Poisson ratio of matrix material and inclusions

5.8.1 Coarse Space Robustness

We choose the overlapping subdomains such that they coincide with the supports $\bar{\omega}_p$, $p \in \bar{\mathcal{N}}_H$ of the coarse basis functions. Then, $\{\Omega_i, i = 1, \dots, N\} = \{\omega_p, p \in \bar{\mathcal{N}}_H\}$
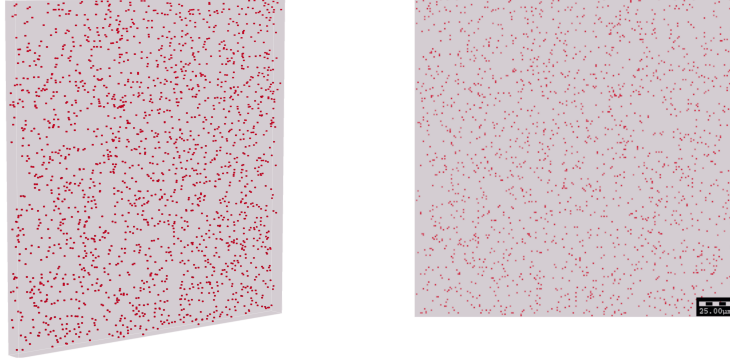
Figure 5.4: Medium 2: binary composite: discretization in $240 \times 240 \times 12$ voxels; matrix material (grey) and $1 \times 1 \times 1$ inclusions (red) identically distributed; $3D$ view (left) and 2D projection (right)

defines an overlapping covering of $\bar{\Omega}$ with overlap width $\delta = O(H)$, often referred to as a *generous overlap*. We perform tests observing the performance of the two-level additive Schwarz preconditioner using linear and energy minimizing coarsening. Condition numbers as well as iteration numbers of the PCG algorithm are presented. The stopping criterion is to reduce the preconditioned initial residual by six orders of magnitude. For the construction of the energy minimizing basis functions, the Lagrange multiplier systems are solved using the CG algorithm, the initial residual is reduced by three orders of magnitude.

In the first experiment, we test the robustness of the method on medium 1 for fixed mesh parameters under the variation of the contrast Δ_E. The Tables 5.3 and 5.4 show the corresponding condition numbers and iteration numbers having stiff ($\Delta_E > 1$) and soft ($\Delta_E < 1$) inclusions. In the former case, robustness is achieved only for the energy minimizing coarse space, while linear coarsening leads to non-uniform convergence results. Considering soft inclusions, both coarse spaces are bounded in energy, an upper natural bound is evidently given for $\Delta_E = 1$. Linear coarse space and energy minimizing coarse space both perform well.

In Experiment 2, performed on medium 1, we measure the condition numbers and iteration numbers under variation of the mesh parameters, while keeping the PDE coefficients fixed. We observe similar results as in Experiment 1. Table 5.5 shows the condition numbers for linear and energy minimizing coarsening. For the linear coarse space, the condition number shows a linear dependence on the number of subdomains,

Δ_E	LIN		EM	
	n_{it}	$\kappa(M_{AS}^{-1}A)$	n_{it}	$\kappa(M_{AS}^{-1}A)$
10^0	13	4.4	14	4.9
10^3	21	18.7	14	5.0
10^6	25	109.0	14	5.0
10^9	25	109.0	14	5.0

Table 5.3: Iteration numbers n_{it} and condition numbers $\kappa(M_{AS}^{-1}A)$ for Experiment 1; geometry: $1/h$ x $1/h$ x H/h, $h = 1/240$, $H = 12h$; linear and energy minimizing coarsening for different contrasts $\Delta_E \geq 1$

Δ_E	LIN		EM	
	n_{it}	$\kappa(M_{AS}^{-1}A)$	n_{it}	$\kappa(M_{AS}^{-1}A)$
10^{-0}	13	4.4	13	4.9
10^{-3}	13	4.4	13	5.0
10^{-6}	13	4.4	13	5.0
10^{-9}	13	4.4	13	5.0

Table 5.4: Iteration numbers n_{it} and condition numbers $\kappa(M_{AS}^{-1}A)$ for Experiment 1; geometry: $1/h$ x $1/h$ x H/h, $h = 1/240$, $H = 12h$; linear and energy minimizing coarsening for different contrasts $\Delta_E \leq 1$

h	LIN		EM	
	n_{it}	$\kappa(M_{AS}^{-1}A)$	n_{it}	$\kappa(M_{AS}^{-1}A)$
$1/60$	14	7.9	13	4.4
$1/120$	17	28.1	14	5.0
$1/180$	21	61.8	14	4.9
$1/240$	25	109.0	14	5.0

Table 5.5: Iteration numbers n_{it} and condition numbers $\kappa(M_{AS}^{-1}A)$ for Experiment 2; geometry: $1/h$ x $1/h$ x H/h; $H = 12h$; linear and energy minimizing coarsening for different h; contrast: $\Delta_E = 10^6$

while the condition number for energy minimizing coarsening is uniformly bounded.

In the first experiment, we obtained coefficient independent convergence rates of the energy minimizing coarse space on medium 1. In a second part, we test the performance of the method on medium 2, where the small inclusions are identically distributed. This is what we see in the Tables 5.6 and 5.7 for Experiment 1 on medium 2: For fixed mesh parameters under the variation of the contrast Δ_E, the corresponding condition

numbers and iteration numbers are shown having stiff ($\Delta_E > 1$) and soft ($\Delta_E < 1$) inclusions. Robustness for the linear coarse space is only achieved in the latter case where soft inclusions are considered. For stiff inclusions, the linear coarsening strategy leads to iteration numbers and condition numbers which strongly depend on the contrast in the medium. The energy minimizing coarse space is fully robust w.r.t. coefficient variations.

	LIN		EM	
Δ_E	n_{it}	$\kappa(M_{AS}^{-1}A)$	n_{it}	$\kappa(M_{AS}^{-1}A)$
10^0	13	4.4	14	4.9
10^3	27	19.3	14	4.9
10^6	66	414	14	5.0
10^9	68	427	14	5.0

Table 5.6: Iteration numbers n_{it} and condition numbers $\kappa(M_{AS}^{-1}A)$ for Experiment 1 on medium 2; geometry: $1/h$ x $1/h$ x H/h, $h = 1/240$, $H = 12h$; linear and energy minimizing coarsening for different contrasts $\Delta_E \geq 1$

	LIN		EM	
Δ_E	n_{it}	$\kappa(M_{AS}^{-1}A)$	n_{it}	$\kappa(M_{AS}^{-1}A)$
10^{-0}	13	4.4	14	4.9
10^{-3}	13	4.4	14	5.0
10^{-6}	13	4.4	14	5.0
10^{-9}	13	4.4	14	5.0

Table 5.7: Iteration numbers n_{it} and condition numbers $\kappa(M_{AS}^{-1}A)$ for Experiment 1 on medium 2; geometry: $1/h$ x $1/h$ x H/h, $h = 1/240$, $H = 12h$; linear and energy minimizing coarsening for different contrasts $\Delta_E \leq 1$

Now, we perform Experiment 2 on medium 2 and measure the condition numbers and iteration numbers under variation of the mesh parameters and fixed PDE coefficients. Table 5.8 shows iteration and condition numbers for linear and energy minimizing coarsening. Mesh independent bounds are achieved for the energy minimizing coarse space. Using the vector-valued linear coarse space, iteration numbers as well as condition numbers grow with the number of subdomains.

	LIN		EM	
h	n_{it}	$\kappa(M_{AS}^{-1}A)$	n_{it}	$\kappa(M_{AS}^{-1}A)$
1/60	26	39.2	13	4.4
1/120	48	154	14	5.0
1/180	52	261	14	4.9
1/240	66	414	14	5.0

Table 5.8: Iteration numbers n_{it} and condition numbers $\kappa(M_{AS}^{-1}A)$ for Experiment 2 on medium 2; geometry: $1/h$ x $1/h$ x H/h; $H = 12h$; linear and energy minimizing coarsening for different h; contrast: $\Delta_E = 10^6$

5.8.2 Coarse Space Approximation

In a second set of experiments, we test the approximation properties of the energy minimizing coarse space. The domain $\bar{\Omega} = [0,1] \times [0,1] \times [0,L]$ contains a binary medium with small inclusions. Again, we distinguish between medium 1 (Figure 5.3: inclusions in the interior of each coarse element) and medium 2 (Figure 5.4: identically distributed inclusions). We solve the linear system $-\mathrm{div}\,\boldsymbol{\sigma}(\boldsymbol{u}) = \boldsymbol{f}$ in $\bar{\Omega} \setminus \Gamma_D$ with a constant volume force $\boldsymbol{f} = (1,1,0)^\top$ in the x- and y-component. Homogeneous Dirichlet and Neumann boundary conditions are applied on the boundary $\partial\Omega$. Dirichlet conditions in the first unknown are given on $\Gamma_1 = \{(x,y,z)^\top \in \partial\Omega : x = 0, x = 1\}$, in the second unknown on $\Gamma_2 = \{(x,y,z)^\top \in \partial\Omega : y = 0, y = 1\}$, and in the third unknown on $\Gamma_3 = \{(x,y,z)^\top \in \partial\Omega : z = 0, z = L\}$.

Let $\boldsymbol{u}^h$ denote the approximate solution on a fine mesh $\mathcal{T}_h$. With the bilinear form defined in (2.9) and the space $\mathcal{V}_0^h$ of piecewise linear vector-valued basis functions as defined in (2.11), it holds $a(\boldsymbol{u}^h, \boldsymbol{v}^h) = F(\boldsymbol{v}^h)\ \forall \boldsymbol{v}^h \in \mathcal{V}_0^h$. This formulation leads to the linear system $A\mathbf{u}^h = \mathbf{f}^h$. Let $\mathcal{V}_0^{\mathrm{EM}}$ be the space of energy minimizing basis functions on the coarse triangulation $\mathcal{T}_H$ which vanish on the Dirichlet boundary $\Gamma_i, i = 1, 2, 3$ (see section 5.6). The energy minimizing solution is given by $\boldsymbol{u}^{\mathrm{EM}} \in \mathcal{V}_0^{\mathrm{EM}}$, such that $a(\boldsymbol{u}^{\mathrm{EM}}, \boldsymbol{v}^H) = F(\boldsymbol{v}^H)\ \forall \boldsymbol{v}^H \in \mathcal{V}_0^{\mathrm{EM}}$. Using the fine-scale representation of an energy minimizing basis function as defined in (5.8), the equivalent linear system reads $A_H \mathbf{u}^H = \mathbf{f}^H$. Here, $A_H = R_H A R_H^\top$ is the coarse stiffness matrix, $\mathbf{f}^H = R_H \mathbf{f}^h$ and $\mathbf{u}^{\mathrm{EM}} = R_H^\top \mathbf{u}^H$ is the vector whose entries define the fine-scale representation of $\boldsymbol{u}^{\mathrm{EM}}$ in terms of the basis of $\mathcal{V}_0^h$.

For fixed mesh parameters h and H, under the variation of the contrast Δ_E, the Tables

5.9 and 5.10 show the relative approximation errors $\|\mathbf{u}^h - \mathbf{u}^c\|$ in l_2 and in the "energy" norm for linear (c=LIN) and energy minimizing (c=EM) coarse space for medium 1 and medium 2, respectively. The fine solution $\mathbf{u}^h$ is computed approximately within

Δ_E	$\dfrac{\|\mathbf{u}^h - \mathbf{u}^c\|_{l_2}}{\|\mathbf{u}^h\|_{l_2}}$		$\dfrac{\|\mathbf{u}^h - \mathbf{u}^c\|_A}{\|\mathbf{u}^h\|_A}$	
	LIN	EM	LIN	EM
10^{-9}	$8.63 \cdot 10^{-3}$	$1.09 \cdot 10^{-1}$	$8.92 \cdot 10^{-2}$	$3.32 \cdot 10^{-1}$
10^{-6}	$8.63 \cdot 10^{-3}$	$1.09 \cdot 10^{-1}$	$8.92 \cdot 10^{-2}$	$3.32 \cdot 10^{-1}$
10^{-3}	$8.63 \cdot 10^{-3}$	$1.09 \cdot 10^{-1}$	$8.91 \cdot 10^{-2}$	$3.32 \cdot 10^{-1}$
10^0	$8.09 \cdot 10^{-3}$	$1.09 \cdot 10^{-1}$	$8.53 \cdot 10^{-2}$	$3.31 \cdot 10^{-1}$
10^3	$7.39 \cdot 10^{-1}$	$1.07 \cdot 10^{-1}$	$8.60 \cdot 10^{-1}$	$3.28 \cdot 10^{-1}$
10^6	$9.97 \cdot 10^{-1}$	$1.07 \cdot 10^{-1}$	$9.99 \cdot 10^{-1}$	$3.28 \cdot 10^{-1}$
10^9	$9.97 \cdot 10^{-1}$	$1.07 \cdot 10^{-1}$	$9.99 \cdot 10^{-1}$	$3.28 \cdot 10^{-1}$

Table 5.9: Approximation of fine-scale solution by linear and energy minimizing coarse space for medium 1; geometry: $1/h$ x $1/h$ x H/h, $h = 1/120$, $H = 12h$

the PCG algorithm by reducing the initial preconditioned residual by 12 orders of magnitude. The coarse solution $\mathbf{u}^H$ is computed exactly using a sparse direct solver for the coarse linear system. For both media, the energy minimizing coarse space gives stable approximation errors, only slightly varying with the contrast. The linear coarse space shows only a poor approximation of the fine-scale solution for high contrasts $\Delta_E \gg 1$. The explanation is that for $\Delta_E \gg 1$, the fine-scale solution is contained in a space which is nearly A-orthogonal to the space spanned by the linear coarse basis functions. Note that this is in agreement with the results presented in Table 5.5, where the condition number grows almost linearly with the number of subdomains.

We also observe from Table 5.9 and 5.10 that for soft inclusions ($\Delta_E \leq 1$), the approximation error is smaller by the linear coarse space than by the energy minimizing coarse space. The latter is due to the circumstance that the vector-valued energy minimizing basis is, even for homogeneous coefficients, not piecewise linear on the coarse triangulation. It is known that the shape of the energy minimizing basis functions is in general mesh dependent, e.g. for the discretization of the scalar Poisson problem on a regular mesh in 2D, an energy minimizing basis is observed to be piecewise linear in [105] (see also [98]). However, for the vector-valued problem considered here with the mesh as in section 2.3.2, the vector-valued energy minimizing basis is not piecewise linear on the

Δ_E	$\dfrac{\|\mathbf{u}^h - \mathbf{u}^c\|_{l_2}}{\|\mathbf{u}^h\|_{l_2}}$		$\dfrac{\|\mathbf{u}^h - \mathbf{u}^c\|_A}{\|\mathbf{u}^h\|_A}$	
	LIN	EM	LIN	EM
10^{-9}	$8.60 \cdot 10^{-3}$	$1.09 \cdot 10^{-1}$	$8.90 \cdot 10^{-2}$	$3.32 \cdot 10^{-1}$
10^{-6}	$8.60 \cdot 10^{-3}$	$1.09 \cdot 10^{-1}$	$8.90 \cdot 10^{-2}$	$3.32 \cdot 10^{-1}$
10^{-3}	$8.60 \cdot 10^{-3}$	$1.09 \cdot 10^{-1}$	$8.90 \cdot 10^{-2}$	$3.32 \cdot 10^{-1}$
10^{0}	$8.09 \cdot 10^{-3}$	$1.09 \cdot 10^{-1}$	$8.53 \cdot 10^{-2}$	$3.31 \cdot 10^{-1}$
10^{3}	$7.01 \cdot 10^{-1}$	$1.15 \cdot 10^{-1}$	$8.37 \cdot 10^{-1}$	$3.40 \cdot 10^{-1}$
10^{6}	$9.99 \cdot 10^{-1}$	$1.12 \cdot 10^{-1}$	$1.00 \cdot 10^{-0}$	$3.36 \cdot 10^{-1}$
10^{9}	$1.00 \cdot 10^{-0}$	$1.12 \cdot 10^{-1}$	$1.00 \cdot 10^{-0}$	$3.36 \cdot 10^{-1}$

Table 5.10: Approximation of fine-scale solution by linear and energy minimizing coarse space for medium 2; geometry: $1/h$ x $1/h$ x H/h, $h = 1/120$, $H = 12h$

coarse mesh for reasonable mesh sizes $H > h > 0$. The latter also implies that the rigid body rotations are only approximated globally.

We can summarize the numerical results obtained in this section as follows. The energy minimizing construction allows a low energy approximation of the basis functions, independently of the Young's modulus of the inclusions. We considered different media where the discontinuities are either isolated in the interior of coarse elements or randomly distributed. Using an energy minimizing coarse space, our experiments show uniform condition number bounds w.r.t. both, coefficient variations in the Young's modulus and the mesh size. In contrast, robustness is not achieved with the linear coarse space. The linear basis function cannot capture the smallest eigenvalues associated to the discontinuities in the material parameters. The energy of the basis function strongly depends on the Young's modulus of the inclusion. As the experiments show, no uniform iteration number and condition number bounds are achieved. This observation holds for all considered media.

5.9 Conclusions

In this chapter, we construct energy minimizing coarse spaces for microstructural problems in linear elasticity. The coarse basis is such that it contains the rigid body translations exactly, while the rigid body rotations are preserved approximately. We utilize the coarse basis for the construction of two-level overlapping domain decomposition pre-

conditioners in the additive version and perform experiments on 3D binary media. For the class of problems which excludes pure traction boundary values, the results show uniform condition number bounds w.r.t. both, coefficient variations in the Young's modulus and the mesh size. Furthermore, we test the fine-scale approximation of the energy minimizing coarse space and observe uniform results, independent of the contrast in the composite material.

We presented the construction by performing the minimization w.r.t. the global Neumann matrix $\bar{A}$. However, if the Neumann matrix is not available, the minimization can also be performed w.r.t. the stiffness matrix A, where Dirichlet boundary conditions are already applied. We illustrate in the following consideration that this may even lead to an improved treatment of high contrast inclusions which are positioned such that they touch the global Dirichlet boundary. Note that, in both cases, no fine degree of freedom on the Dirichlet boundary should contribute to the interpolation operator. If the global Dirichlet boundary is such that $\Gamma_D := \Gamma_{D_1} = \Gamma_{D_2} = \Gamma_{D_3}$, i.e., Dirichlet conditions are imposed in each component at $x \in \Gamma_D$, the construction of the energy minimizing basis as opposed before does not require additional attention. However, if the Dirichlet boundaries are such that $\Gamma_{D_i} \neq \Gamma_{D_j}$, $i \neq j$, then the construction might produce high energy basis functions near the global Dirichlet boundary when measured in terms of the energy-norm induced by A. More precisely, let us assume that a stiff and small inclusion touches the global boundary and fully lies in a set ω_p with $p \in \bar{\mathcal{N}}_H$, $x^p \in \partial\Omega$. Thus, we have three basis functions $\phi_m^{p,\mathrm{EM}} : \omega_p \to \mathbb{R}^3, m = 1, 2, 3$, with low energy w.r.t. the semi-norm induced by $\bar{A}$. Now, we assume that Dirichlet conditions are applied only in the first component on $\omega_p \cap \Gamma_{D_1} \neq \emptyset$. By construction, each basis function has small energy w.r.t. $\bar{A}$. However, the situation might not be the same when the energy is measured in A-norm, which derives from $\bar{A}$ be deleting entries related to fine Dirichlet degrees of freedom. The energy might depend on the contrast between matrix material and inclusion when measured w.r.t. the A-norm. For instance, if each of the three basis functions describes a rotation of the inclusion, deleting the entries related to Dirichlet DOFs in the first component yields basis functions whose energy grows with the magnitude of the material parameters in the inclusion also for $m = 2$ and $m = 3$. By construction, the "first basis function" does not remain in the coarse space due to the applied Dirichlet boundary conditions. However, the second and third basis

function remain there with possibly high energy w.r.t. A. This specific characteristic can be overcome by performing the overall construction w.r.t. the norm induced by A.

6

Convergence Analysis

In this chapter, we present a novel convergence analysis for two-level overlapping Schwarz preconditioners for multiscale problems in linear elasticity, arising from a vector-valued piecewise-linear finite element discretization. In the context of the developed condition number bounds, we analyse the robustness properties of the multiscale coarse spaces which are introduced in chapter 3, 4 and 5 again in more detail.

The experimental results presented in the previous chapters (see also [16, 17, 19]) justify expectations to obtain condition number bounds for the PDE system of linear elasticity similar to the existing ones for scalar elliptic PDEs in [45] (cf. also the bound in equation (1.4)). This issue is investigated in detail in this chapter (see also [15]). The bounds developed here are sharp and show that robustness may also be achieved for problems where the coefficients cannot be resolved by a coarse mesh. Furthermore, they provide guidance in the construction of robust coarse spaces for two-level overlapping domain decomposition preconditioners. The analysis carried out in this chapter follows the outstanding framework provided in [45]. A condition number bound for the linear elasticity system in the form of the bound in equation (1.4) is obtained.

To give a comprehensive understanding of the analysis presented subsequently, we also recall notations introduced in earlier chapters and equip them by the extensions required.

The chapter is organized as follows. Since we are considering problems with homogeneous boundary conditions on the Dirichlet boundary, we shortly recall the governing equations and the discretization in this setting in section 6.1. Section 6.2 deals with the two-level additive Schwarz method, further notations and assumptions on the ingredi-

ents are introduced. We present the framework for the analysis in section 6.3, section 6.4 contains the main convergence result of the analysis. In the context of the developed convergence results, we investigate the properties of the different multiscale coarsening strategies which are introduced in the previous chapters in section 6.5. We validate the sharpness of the theoretical findings in section 6.6 using the multiscale coarsening strategies to perform numerical tests on binary media in $3D$. A short discussion finalizes the chapter in section 6.7.

6.1 Preliminaries

Let $\Omega \subset \mathbb{R}^d$ be a bounded, open, polygonal ($d = 2$) or polyhedral ($d = 3$) domain. We consider a solid body in Ω, deformed under the influence of volume forces $\boldsymbol{f}$ and traction $\boldsymbol{t}$, the displacement field $\boldsymbol{u}$ of which is governed by the system of linear elasticity as introduced in section 2.2. For simplicity, we may assume in this chapter that homogeneous Dirichlet boundary conditions are imposed on Γ_D in each component of the vector-field, where $\Gamma_D \subset \Gamma = \partial\Omega$ and Γ admits the decomposition into two disjoint subsets Γ_D and Γ_N, $\Gamma = \overline{\Gamma_D \cup \Gamma_N}$ with meas$(\Gamma_D) > 0$. Thus, we are in the setting as introduced in section 2.2 with homogeneous boundary conditions on the Dirichlet boundary. Additionally, we may assume here that the global Dirichlet boundary Γ_D can be characterized by a union of faces $\mathcal{F} \subset T$ of elements $T \in \mathcal{T}_H$. More precisely, if there is a point $x \in \Gamma_D$, then we find $T \in \mathcal{T}_H$ such that an entire face $\mathcal{F}$ of T touches Γ_D. Additionally, we introduce the following convention. We denote by $\Sigma_H := \Sigma_H(\bar{\Omega} \setminus \Gamma_D)$ the set of coarse nodes of $\mathcal{T}_H$ which do not touch the global Dirichlet boundary. This convention applies to the index-set of coarse nodes $\mathcal{N}_H := \mathcal{N}_H(\bar{\Omega} \setminus \Gamma_D)$ in a straightforward manner. Moreover, we make a slight modification of the primarily introduced notation of coarse degrees of freedom in section 2.6. We redefine $\mathcal{D}_H$ to the set of coarse degrees of freedom which do not touch the Dirichlet boundary Γ_D, i.e.

$$\mathcal{D}_H := \mathcal{D}_H(\bar{\Omega} \setminus \Gamma_D) = \Big\{ (p, m) \in \mathbb{N}^{N_p \times d} \; : \; p \in \mathcal{N}_H, \, m \in \{1, \ldots, d\}, \, x^p \notin \Gamma_D \Big\}.$$

For any set $D \subset \bar{\Omega}$, we denote by $\mathcal{D}_H(D) := \{(p, m) \in \mathcal{D}_H \; : \; p \in \mathcal{N}_H(D)\}$ the set of coarse degrees of freedom in D. Beyond the slight modification of the Dirichlet boundary and the notation of $\mathcal{D}_H$, all other notations introduced in chapter 2 remain unchanged.

6.2 Two Level Overlapping Domain Decomposition

The following two theorems repeat basic results in domain decomposition theory. Proofs can be found in [97]. They provide the basis for the convergence analysis presented in the next section. Theorem 6.2.1 also states a reasonable assumption on the choice of the overlapping subdomains.

Theorem 6.2.1. (Colouring argument) *The set of overlapping subspaces* $\{\Omega_i, i = 1, \ldots, N\}$ *can be coloured by* $N_C \leq N$ *different colours such that if two subspaces* Ω_i *and* Ω_j *have the same colour, it holds* $\Omega_i \cap \Omega_j = \emptyset$. *Let* N_C *be the smallest possible number such that the colouring argument holds. Then, the largest eigenvalue of the two-level additive Schwarz preconditioned linear system is bounded by*

$$\lambda_{\max}(M_{\mathrm{AS}}^{-1} A) \leq N_C + 1.$$

Theorem 6.2.2. (Stable decomposition) *Suppose there exists a number* $C_0 \geq 1$, *such that for every* $\boldsymbol{u}^h \in \mathcal{V}_0^h$, *there exists a decomposition* $\boldsymbol{u}^h = \sum_{i=0}^N \boldsymbol{u}^i$ *with* $\boldsymbol{u}^0 \in \mathcal{V}_0^H$ *and* $\boldsymbol{u}^i \in \mathcal{V}^h(\Omega_i)$, $i = 1, \ldots, N$ *such that*

$$\sum_{i=0}^N a(\boldsymbol{u}^i, \boldsymbol{u}^i) \leq C_0^2 \, a(\boldsymbol{u}^h, \boldsymbol{u}^h).$$

Then, it holds

$$\lambda_{\min}(M_{\mathrm{AS}}^{-1} A) \geq C_0^{-2}.$$

As we can see, the choice of the coarse space has no influence on the estimate of the largest eigenvalue of the preconditioned system. However, it is crucial for obtaining a small constant C_0 in the estimate of the smallest eigenvalue in Theorem 6.2.2. We proceed with stating some assumptions on the overlapping covering $\{\Omega_i, i = 1, \ldots, N\}$, the coarse triangulation $\mathcal{T}_H$ and the coarse space $\mathcal{V}^H$ and introduce some notations.

6.2.1 The Overlapping Subdomains

For each $i = 1, \ldots, N$, let $\Omega_i^\circ := \{x \in \Omega_i \,:\, x \notin \bar{\Omega}_j \text{ for any } j \neq i\}$ be the subset of Ω_i which is not overlapped with the closure of any other subdomain. Being oriented towards the analysis for scalar elliptic PDEs in [45], we use the tools introduced in [45] which allow us stating regularity assumptions on the subdomains and the width of the

overlap $\Omega_i \setminus \Omega_i^\circ$ between subdomains and their direct neighbours. We introduce the *near boundary subsets*, defined for $\theta > 0$ by:

$$\Omega_{i,\theta} := \left\{ x \in \Omega_i \,:\, \mathrm{dist}(x, \Gamma_i) < \theta \right\},$$

where $\Gamma_i := \partial\Omega_i \setminus \Gamma_D$. The part of Ω_i which is overlapped with its neighbours should be of uniform width $\delta_i > 0$. In the following, we refer to δ_i as the *overlap parameter*.

Assumption 6.2.1. (Overlap assumption [45]) *For a fixed constant $0 < c < 1$ and $\delta_i > 0$, it holds*

$$\Omega_{i,c\delta_i} \subset \Omega_i \setminus \Omega_i^\circ \subset \Omega_{i,\delta_i}.$$
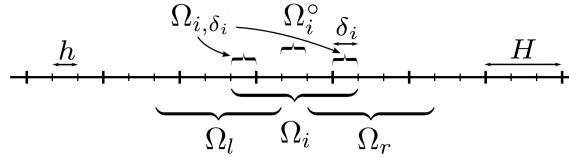
Figure 6.1: Illustration of the subdomain Ω_i, the interior Ω_i° which is not overlapped by any other subdomain and the near boundary subset Ω_{i,δ_i} in 1D

Definition 6.2.1. (Partition property [45]) *We say that the set $\Omega_{i,\theta}$ has the partition property if there exists a finite covering of $\Omega_{i,\theta}$ with Lipschitz polyhedra, each of which has: volume $\sim \theta^d$; a closure which intersects Γ_i in a set of measure $\sim \theta^{d-1}$; diameter $\sim \theta$; length of edges $\sim \theta$;*

We extend the concept of the regularity of meshes (cf. Definition 2.3.2) to subdomains in the following way:

Definition 6.2.2. (Shape regularity) *Let $\Omega_i \subset \bar{\Omega}$ be such that Assumption 6.2.1 holds. We introduce the shape parameter ρ_i of Ω_i by*

$$\rho_i := \sup \left\{ \theta \,:\, \Omega_{i,\theta} \text{ has the partition property} \right\}.$$

Then, Ω_i is said to be shape-regular if $\rho_i \sim \mathrm{diam}(\Omega_i)$.

Assuming that Ω_i consists of the interior of a union of shape-regular elements $\tau \in \mathcal{T}_h$ (cf. section 2.3.1), the same applies to the overlapped part $\Omega_i \setminus \Omega_i^\circ$. Hence, $\Omega_{i,\delta_i} \supset \Omega_i \setminus \Omega_i^\circ$ has the partition property and by Assumption 6.2.1, we have $0 < \delta_i \leq c'\rho_i$. As introduced

in equation (2.21), we denote the restriction of the subspace $\mathcal{V}^h$ to the subdomain Ω_i by $\mathcal{V}^i = \mathcal{V}^h(\Omega_i)$ for $i = 1, \ldots, N$. For our analysis in the next section, we require partition of unity functions subordinate to the covering Ω_i, which are defined as follows [45].

Definition 6.2.3. (Partition of unity) *A partition of unity subordinate to a covering* $\{\Omega_i, i = 1, \ldots, N\}$ *of* Ω *is a set of functions* $\{\chi_i \in W^{1,\infty}(\Omega), \ i = 1, \ldots, N\}$, *with the properties:*

(PU1) $\quad \operatorname{supp} \chi_i \subset \bar{\Omega}_i, \quad i = 1, \ldots, N;$

(PU2) $\quad 0 \leq \chi_i(x) \leq 1, \quad x \in \bar{\Omega}, \ i = 1, \ldots, N;$

(PU3) $\quad \sum_{i=1}^{N} \chi_i(x) = 1, \quad x \in \bar{\Omega};$

The existence of such a partition of unity can be shown, given that for each Ω_i, the overlap assumption holds with an overlap parameter $\delta_i > 0$ (e.g. [97, Lemma 3.4]). Indeed, we have $\chi_i(x) = 1$ and thus, $\nabla \chi_i(x) = 0$ in $\Omega_i \setminus \Omega_i^\circ$. We denote by $\Pi(\{\Omega_i\})$ the set of all partitions of unity $\{\chi_i\}$ subordinate to the covering $\{\Omega_i, i = 1, \ldots, N\}$.

6.2.2 The Coarse Space

As introduced in section 2.3.2 and 2.4, let the coarse mesh $\mathcal{T}_H$ consist of triangles $(d = 2)$ or tetrahedra $(d = 3)$, with coarse mesh diameter $H := \max_{T \in \mathcal{T}_H} H_T$ where $H_T = \operatorname{diam} T$. For $p \in \bar{\mathcal{N}}_H$, we recall respectively introduce the sets

$$\omega_p := \operatorname{interior}\left(\bigcup_{\{T \in \mathcal{T}_H \, : \, p \in \mathcal{N}_H(T)\}} T \right), \quad \omega_T := \operatorname{interior}\left(\bigcup_{\{p \in \mathcal{N}_H(T)\}} \bar{\omega}_p \right),$$

which consist of the interior of the union of coarse elements which are attached to the node $x^p \in \bar{\Sigma}_H$ and the element $T \in \mathcal{T}_H$, respectively. Following section 2.4, for any $p \in$
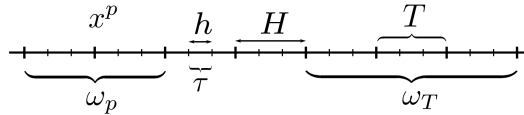
Figure 6.2: Illustration of the sets ω_p and ω_T in 1D

$\bar{\mathcal{N}}_H$ and $m \in \{1, \ldots, d\}$, we define a vector-valued basis function $\phi_m^{p,\mathrm{H}} : \bar{\Omega} \to \mathbb{R}^d \in \mathcal{V}^h$, such that the abstract coarse space $\mathcal{V}_0^H = \operatorname{span}\{\phi_m^{p,\mathrm{H}} : p \in \bar{\mathcal{N}}_H, \ x^p \notin \Gamma_D\}$ satisfies the constraints in Assumption 2.4.1, which are repeated here for a better reading:

Assumption 6.2.2. (Abstract coarse space)

(C1) $\quad \phi_m^{p,\mathrm{H}} = (\phi_{m1}^{p,\mathrm{H}}, \ldots, \phi_{md}^{p,\mathrm{H}})^\top, \; \phi_{mk}^{p,\mathrm{H}}(x^q) = \delta_{pq}\,\delta_{mk}, \; p \in \bar{\mathcal{N}}_H, \; k \in \{1, \ldots, d\},$

(C2) $\quad \operatorname{supp} \phi_m^{p,\mathrm{H}} \subset \bar{\omega}_p,$

(C3) $\quad \|\phi_{mk}^{p,\mathrm{H}}\|_{L^\infty(\Omega)} \le C, \; k \in \{1, \ldots, d\},$

(C4) $\quad \sum_{p \in \bar{\mathcal{N}}_H} \phi_{mk}^{p,\mathrm{H}}(x) = \delta_{mk}, \; x \in \bar{\Omega}, \; k \in \{1, \ldots, d\},$

(C5) $\quad \mathcal{RBM} \subset \operatorname{span}\{\phi_m^{p,\mathrm{H}} : p \in \bar{\mathcal{N}}_H, \; k \in \{1, \ldots, d\}\}.$

The set of rigid body modes are defined in chapter 2.4. We make one assumption on the correlation of the size of the overlapping subdomains and the diameter of the coarse mesh and introduce

$$\mathcal{T}_H(\Omega_i) := \Big\{ T \in \mathcal{T}_H : T \cap \bar{\Omega}_i \ne \emptyset \Big\}.$$

We define the *local coarse mesh diameter* [45]

$$H_i := \max_{T \in \mathcal{T}_H(\Omega_i)} H_T. \tag{6.1}$$

Assumption 6.2.3. (Coarse space and subdomains) *Let H_i be the local coarse mesh diameter in* (6.1) *and let ρ_i be the shape parameter in Definition 6.2.2. We require that there exists a constant C, such that*

(C6) $\quad H_i \le C\rho_i, \quad i = 1, \ldots, N.$

6.3 General Framework for Analysis

In the following two sections we present a comprehensive convergence analysis for two-level additive Schwarz domain decomposition methods for multiscale problems in linear elasticity. We first introduce further semi-norms and state assumptions on the stiffness tensor in section 6.3.1. Important technical lemmas are provided in section 6.3.2. They are necessary to prove the coefficient explicit condition number bound in Theorem 6.4.1.

6.3.1 Notation and Assumptions on Material Parameters

In our analysis, we may assume that the heterogeneities of the underlying material are resolved by the fine mesh $\mathcal{T}_h$. Thus, the stiffness tensor $\boldsymbol{C}$ is piecewise constant in

$\tau \in \mathcal{T}_h$. For any domain $\omega \subset \Omega$, we define the bilinear form

$$a_\omega(\boldsymbol{u}, \boldsymbol{v}) := \int_\omega (\boldsymbol{C} : \boldsymbol{\varepsilon}(\boldsymbol{u})) : \boldsymbol{\varepsilon}(\boldsymbol{v}) \, dx. \tag{6.2}$$

If $\omega = \Omega$, we may omit the index and write $a(\boldsymbol{u}, \boldsymbol{v}) = a_\Omega(\boldsymbol{u}, \boldsymbol{v})$ instead. Furthermore, we assume the stiffness tensor $\boldsymbol{C}$ to be positive definite and uniformly bounded in $\bar{\Omega}$. To be more specific, we assume that a lower and upper bound for the eigenvalues of the stiffness tensor exists not only globally in $\bar{\Omega}$, but also locally in each $\tau \in \mathcal{T}_h$. More precisely, we assume there is $c_{\min} = c_{\min}(\tau) > 0$ and $c_{\max} = c_{\max}(\tau)$ such that the strain energy in τ is bounded by $c_{\min} \boldsymbol{\varepsilon}(\boldsymbol{v}) : \boldsymbol{\varepsilon}(\boldsymbol{v}) \leq (\boldsymbol{C} : \boldsymbol{\varepsilon}(\boldsymbol{v})) : \boldsymbol{\varepsilon}(\boldsymbol{v}) \leq c_{\max} \boldsymbol{\varepsilon}(\boldsymbol{v}) : \boldsymbol{\varepsilon}(\boldsymbol{v})$ a.e. for all $\boldsymbol{v} \in [H^1(\tau)]^d$. By proper rescaling of the stiffness tensor with a constant, we may assume that $c_{\min} \geq 1$ a.e. in Ω. Note that this does not change the condition number of the corresponding linear system in equation (2.14).

The bilinear form in equation (6.2) induces a weighted semi-norm on $[H^1(\omega)]^d$, which we denote by $|\cdot|_{a,\omega}$. It is also referred to as the "energy" norm. Furthermore, we introduce the unweighted semi-norm

$$|\boldsymbol{v}|_{\varepsilon,\omega}^2 := \int_\omega \boldsymbol{\varepsilon}(\boldsymbol{v}) : \boldsymbol{\varepsilon}(\boldsymbol{v}) \, dx. \tag{6.3}$$

Due to the assumption on the smallest eigenvalue of $\boldsymbol{C}$, we have $|\boldsymbol{v}|_{\varepsilon,\omega} \leq |\boldsymbol{v}|_{a,\omega}$ for all $\boldsymbol{v} \in [H^1(\omega)]^d$. Additionally, for any $\tau \in \mathcal{T}_h$, there is $c_{\max}$ uniformly bounded in Ω, $c_{\max}(\tau) < \infty$ such that $|\boldsymbol{v}|_{a,\tau}^2 \leq c_{\max}(\tau)|\boldsymbol{v}|_{\varepsilon,\tau}^2$ for $\boldsymbol{v} \in [H^1(\tau)]^d$. As introduced in section 2.1, the L^2-norm on $[H^1(\omega)]^d$ reads

$$\|\boldsymbol{v}\|_{[L^2(\omega)]^d}^2 := \int_\omega |\boldsymbol{v}|^2 \, dx.$$

Equation (2.1) and (2.2) state the general form of the PDE system of anisotropic linear elasticity. When each of the constituent materials of the solid body is isotropic, the elasticity tensor simplifies to $c_{ijkl}(x) = \lambda(x)\delta_{ij}\delta_{jk} + \mu(x)(\delta_{ik}\delta_{jl} + \delta_{il}\delta_{jk})$ in Ω, with Lamé coefficients λ and μ. The stress tensor reduces to $\boldsymbol{\sigma}(\boldsymbol{u}) = \boldsymbol{C} : \boldsymbol{\varepsilon}(\boldsymbol{u}) = \lambda \text{tr}(\boldsymbol{\varepsilon}(\boldsymbol{u}))\boldsymbol{I} + 2\mu\boldsymbol{\varepsilon}(\boldsymbol{u})$. To simplify the notations, in the following analysis, we assume that each constituent of the underlying composite is isotropic. However, all the theoretical results also apply if the stiffness tensor $\boldsymbol{C}$ is anisotropic. Remark 6.4.1 summarizes the adaptions required to make the theory applicable.

To ensure that the "isotropic stiffness tensor" is positive definite with $c_{\min} \geq 1$, it is sufficient to assume that $\mu \geq 1/2$ and $2\mu + d\lambda \geq 1$ a.e. in $\bar{\Omega}$. A bound for the largest eigenvalue of the stiffness tensor is given by $c_{\max}(\tau) = \max\{2\mu, 2\mu + d\lambda\}$ for each $\tau \in \mathcal{T}_h$. It can also be derived from the following relation, valid in $\mathbb{R}^d$: We have for each $\tau \in \mathcal{T}_h$,

$$\int_\tau \varepsilon(\boldsymbol{u}) : \varepsilon(\boldsymbol{u})\, dx = \sum_{i,j=1}^d \int_\tau \varepsilon_{ij}(\boldsymbol{u})^2\, dx \geq \sum_{i=1}^d \int_\tau \varepsilon_{ii}(\boldsymbol{u})^2\, dx,$$

and

$$\int_\tau \varepsilon(\boldsymbol{u}) : \big(\mathrm{tr}(\varepsilon(\boldsymbol{u}))\boldsymbol{I}\big)\, dx = \sum_{i,j=1}^d \int_\tau \varepsilon_{ii}(\boldsymbol{u})\varepsilon_{jj}(\boldsymbol{u})\, dx \leq d \sum_{i=1}^d \int_\tau \varepsilon_{ii}(\boldsymbol{u})^2\, dx.$$

Thus, we obtain $\int_\tau \varepsilon(\boldsymbol{u}) : \varepsilon(\boldsymbol{u})\, dx \geq d^{-1} \int_\tau \varepsilon(\boldsymbol{u}) : \big(\mathrm{tr}(\varepsilon(\boldsymbol{u}))\boldsymbol{I}\big)\, dx\ \forall \boldsymbol{u} \in [H^1(\tau)]^d$. Recalling the bilinear form in equation (6.2) with $\boldsymbol{C} : \varepsilon(\boldsymbol{u}) = \lambda \mathrm{tr}(\varepsilon(\boldsymbol{u}))\boldsymbol{I} + 2\mu\varepsilon(\boldsymbol{u})$ yields the estimate. Note that the above relation holds also pointwise a.e. in Ω. Since $\int_\tau \nabla \cdot \boldsymbol{u}\, dx = \int_\tau \mathrm{tr}(\varepsilon(\boldsymbol{u}))\, dx$, the divergence-free term is dominating if $\lambda \gg \mu$.

6.3.2 Technical Lemmas

In this section we introduce two indicators which measure the coefficient robustness of the coarse basis as well as the coefficient robustness w.r.t. the partitioning into overlapping subdomains. These indicators both appear in the condition number bound of the preconditioned linear system which is stated in Theorem 6.4.2.

To prove the existence of a stable decomposition (Theorem 6.2.2), we need to show the existence of a coarse interpolant which satisfies the approximation property and is stable in the appropriate norms. Therefore, we introduce a quasi-interpolant (cf. [24]) in the following way.

Definition 6.3.1. *Let the coarse basis functions be given according to Assumption 6.2.2. We define the (linear) quasi-interpolant $I^H : [H_0^1(\Omega)]^d \to \mathcal{V}^H$ by*

$$I^H \boldsymbol{u} = \sum_{p \in \mathcal{N}_H} \sum_{m=1}^d \pi_m^{p,\boldsymbol{u}}(x^p)\, \phi_m^{p,\mathrm{H}},$$

where $\pi^{p,\boldsymbol{u}} := (\pi_1^{p,\boldsymbol{u}}, \ldots, \pi_d^{p,\boldsymbol{u}})^\top \in [H^1(\omega_p)]^d$ is the L^2-projection of $\boldsymbol{u}$ onto the space of rigid body modes $\mathfrak{RBM}(\omega_p)$.

The following lemma gives the approximation property of the quasi-interpolant.

Lemma 6.3.1. (Approximation property) *For the linear operator $I^H : [H_0^1(\Omega)]^d \to \mathcal{V}^H$ of Definition 6.3.1, the following approximation property holds: For all $\boldsymbol{u} \in [H_0^1(\Omega)]^d$ and $T \in \mathcal{T}_H$,*

$$\|\boldsymbol{u} - I^H\boldsymbol{u}\|_{[L^2(T)]^d}^2 \leq CH^2|\boldsymbol{u}|_{\varepsilon,\omega_T}^2 ,$$

where the constant C is independent of H.

Proof. Let $T \in \mathcal{T}_H$ such that ω_T does not touch the boundary $\Gamma_D \subset \partial\Omega$. Let $\boldsymbol{r}$ be the L^2-projection of $\boldsymbol{u}$ onto the space of rigid body modes $\mathfrak{RBM}(\omega_T)$. Define $\hat{\boldsymbol{u}} := \boldsymbol{u} - \boldsymbol{r}$. Then, $\boldsymbol{r} \in \mathfrak{RBM}(\omega_T)$ and $\hat{\boldsymbol{u}}$ is orthogonal to $\boldsymbol{r}$ in $[L^2(\omega_T)]^d$. By Assumption 6.2.2 *(C5)*, the coarse space $\mathcal{V}^H|_{\bar{\omega}_p}$ contains the rigid body modes on $\bar{\omega}_p \subset \bar{\Omega}$ for all $p \in \mathcal{N}_H(T)$. It holds pointwise in T that $I^H\boldsymbol{u} = I^H(\hat{\boldsymbol{u}} + \boldsymbol{r}) = I^H(\hat{\boldsymbol{u}}) + \boldsymbol{r}$. Thus we obtain

$$\begin{aligned}
\|\boldsymbol{u} - I^H\boldsymbol{u}\|_{[L^2(T)]^d}^2 &= \|\hat{\boldsymbol{u}} + \boldsymbol{r} - (I^H(\hat{\boldsymbol{u}}) + \boldsymbol{r})\|_{[L^2(T)]^d}^2 \\
&= \|\hat{\boldsymbol{u}} - I^H\hat{\boldsymbol{u}}\|_{[L^2(T)]^d}^2 \\
&\leq 2\big(\|\hat{\boldsymbol{u}}\|_{[L^2(T)]^d}^2 + \|I^H\hat{\boldsymbol{u}}\|_{[L^2(T)]^d}^2\big).
\end{aligned}$$

Now, we obtain

$$\begin{aligned}
\|I^H\hat{\boldsymbol{u}}\|_{[L^2(T)]^d} &= \Big\| \sum_{p \in \mathcal{N}_H(T)} \sum_{m=1}^d \pi_m^{p,\hat{\boldsymbol{u}}}(x^p)\phi_m^{p,\mathrm{H}} \Big\|_{[L^2(T)]^d} \\
&\leq \sum_{p \in \mathcal{N}_H(T)} \Big\| \sum_{m=1}^d \pi_m^{p,\hat{\boldsymbol{u}}}(x^p)\phi_m^{p,\mathrm{H}} \Big\|_{[L^2(\omega_p)]^d} \qquad (6.4) \\
&\leq C\|\hat{\boldsymbol{u}}\|_{[L^2(\omega_T)]^d} ,
\end{aligned}$$

where the last inequality follows from the property of the L^2-projection. Thus, using Lemma 2.5.6, we obtain

$$\begin{aligned}
\|\boldsymbol{u} - I^H\boldsymbol{u}\|_{[L^2(T)]^d}^2 &\leq C\|\hat{\boldsymbol{u}}\|_{[L^2(\omega_T)]^d}^2 \\
&= C\|\boldsymbol{u} - \boldsymbol{r}\|_{[L^2(\omega_T)]^d}^2 \\
&\leq CH^2|\boldsymbol{u}|_{\varepsilon,\omega_T}^2.
\end{aligned}$$

If $T \in \mathcal{T}_H$ is such that ω_T touches the boundary Γ_D at a whole face (3D), the result is obtained using Lemma 2.5.7,

$$\|I^H \boldsymbol{u}\|^2_{[L^2(T)]^d} \leq C\|\boldsymbol{u}\|^2_{[L^2(\omega_T)]^d} \leq CH^2|\boldsymbol{u}|^2_{\varepsilon,\omega_T}.$$

Otherwise, if ω_T touches the Dirichlet boundary only on a node or an edge (3D), the argument before can be applied by adding an additional element to ω_T. $\qquad\square$

Remark 6.3.1. *Note that from the estimates in equation* (6.4)*, we can conclude that* $|\pi_m^{p,\boldsymbol{u}}(x^p)|^2 \leq C|\omega_p|^{-1}\|\boldsymbol{u}\|^2_{[L^2(\omega_p)]^d}$ *for* $m \in \{1,\ldots,d\}$*. This is due to*

$$\phi_m^{p,\mathrm{H}}\|^2_{[L^2(\omega_p)]^d} \sim H^d,$$

and

$$\left\|\pi_m^{p,\boldsymbol{u}}(x^p)\phi_m^{p,\mathrm{H}}\right\|_{[L^2(\omega_p)]^d} \leq C|\pi_m^{p,\boldsymbol{u}}(x^p)|\left\|\phi_m^{p,\mathrm{H}}\right\|_{[L^2(\omega_p)]^d}.$$

Before we prove the stability estimate for the quasi-interpolant in Definition 6.3.1, we introduce the following "stability measure". Note that the dependence of the following indicator on the coefficients λ and μ is implicitly given over the energy functional $|\cdot|_{a,\Omega}$ as defined in section 6.3.1.

Definition 6.3.2. (Coarse space robustness indicator) *Let the coarse space satisfy Assumption 6.2.2. We define the coarse space robustness indicator*

$$\gamma(\lambda,\mu) := \max_{(p,m)\in\mathcal{D}_H}\left\{H_p^{2-d}|\phi_m^{p,\mathrm{H}}|^2_{a,\Omega}\right\}, \quad H_p = \mathrm{diam}(\omega_p). \tag{6.5}$$

Lemma 6.3.2. (Stability estimate) *For the linear operator* $I^H : [H_0^1(\Omega)]^d \to \mathcal{V}^H$ *introduced in Definition 6.3.1, it holds for all* $\boldsymbol{u} \in [H_0^1(\Omega)]^d$ *and* $T \in \mathcal{T}_H$,

$$|I^H \boldsymbol{u}|^2_{a,T} \leq C\,\gamma(\lambda,\mu)\,|\boldsymbol{u}|^2_{a,\omega_T}.$$

Proof. Let $T \in \mathcal{T}_H$. We first consider the case where ω_T does not touch the boundary $\Gamma_D \subset \partial\Omega$. Let $\boldsymbol{r}$ be the L^2-projection of $\boldsymbol{u}$ onto the space of rigid body modes $\mathcal{RBM}(\omega_T)$ and define $\hat{\boldsymbol{u}} := \boldsymbol{u} - \boldsymbol{r}$. By Assumption 6.2.2 *(C5)*, the coarse space $\mathcal{V}^H|_{\bar{\omega}_p}$ preserves

the rigid body modes. Hence, it holds $I^H \boldsymbol{r} = \boldsymbol{r}$ pointwise in ω_T and we obtain

$$
\begin{aligned}
|I^H \boldsymbol{u}|_{a,T}^2 = |I^H \hat{\boldsymbol{u}}|_{a,T}^2 &= \Big| \sum_{p \in \mathcal{N}_H(T)} \sum_{m=1}^{d} \pi_m^{p,\hat{\boldsymbol{u}}}(x^p)\, \phi_m^{p,\mathrm{H}} \Big|_{a,T}^2 \\
&\leq C \max_{(p,m) \in \mathcal{D}_H(T)} |\pi_m^{p,\hat{\boldsymbol{u}}}(x^p)\, \phi_m^{p,\mathrm{H}}|_{a,T}^2 \\
&\leq C \max_{(p,m) \in \mathcal{D}_H(T)} \left(|\omega_p|^{-1} \|\hat{\boldsymbol{u}}\|_{[L^2(\omega_p)]^d}^2 \right) |\phi_m^{p,\mathrm{H}}|_{a,T}^2 \\
&\leq C|T|^{-1} \|\hat{\boldsymbol{u}}\|_{[L^2(\omega_T)]^d}^2 \max_{(p,m) \in \mathcal{D}_H(T)} |\phi_m^{p,\mathrm{H}}|_{a,T}^2 .
\end{aligned}
$$

Since $\hat{\boldsymbol{u}}$ is L^2-orthogonal to any rigid body motion on ω_T, we can apply the scaled Poincaré-Korn inequality (Lemma 2.5.6) and obtain,

$$
\begin{aligned}
|I^H \boldsymbol{u}|_{a,T}^2 &\leq C|T|^{-1} H^2 |\hat{\boldsymbol{u}}|_{\varepsilon,\omega_T}^2 \max_{(p,m) \in \mathcal{D}_H(T)} |\phi_m^{p,\mathrm{H}}|_{a,T}^2 \\
&\leq C \max_{(p,m) \in \mathcal{D}_H(T)} H_p^{2-d} |\phi_m^{p,\mathrm{H}}|_{a,T}^2 \, |\hat{\boldsymbol{u}}|_{\varepsilon,\omega_T}^2 \\
&\leq C\gamma(\lambda,\mu) |\hat{\boldsymbol{u}}|_{a,\omega_T}^2,
\end{aligned}
$$

where we used the assumption that $|\boldsymbol{v}|_{\varepsilon,\omega_T} \leq |\boldsymbol{v}|_{a,\omega_T}$ for all $\boldsymbol{v} \in [H^1(\omega_T)]^d$ in the last estimate. If ω_T touches Γ_D on a face (3D), we apply Lemma 2.5.7 and obtain

$$
\begin{aligned}
|I^H \boldsymbol{u}|_{a,T}^2 &\leq C|T|^{-1} \|\boldsymbol{u}\|_{[L^2(\omega_T)]^d}^2 \max_{(p,m) \in \mathcal{D}_H(T)} |\phi_m^{p,\mathrm{H}}|_{a,\Omega}^2 \\
&\leq C|T|^{-1} |\boldsymbol{u}|_{\varepsilon,\omega_T}^2 \max_{(p,m) \in \mathcal{D}_H(T)} H_p^{2-d} |\phi_m^{p,\mathrm{H}}|_{a,\Omega}^2 \\
&\leq C\gamma(\lambda,\mu) |\boldsymbol{u}|_{a,\Omega}^2 .
\end{aligned}
$$

If ω_T touches $\Gamma_D \subset \partial\Omega$ in a single node or edge (3D), an additional element can be added to ω_T and the previous estimate can be applied. $\qquad \square$

In the proof of the next lemma (Lemma 6.3.3), we are dealing with vector-valued functions which are not piecewise linear on $\mathcal{T}_h$. Therefore, we require the vector-valued nodal interpolant $I^h : [H^1(\Omega)]^d \to \mathcal{V}^h$ which projects the quadratic functions onto $\mathcal{V}^h$. The interpolant is defined by

$$
I^h \boldsymbol{v} = \sum_{j \in \bar{\mathcal{N}}_h} \sum_{k=1}^{d} v_k(x^j) \varphi_k^{j,\mathrm{h}},
$$

where any basis function $\varphi_k^{j,h}$ of $\mathcal{V}^h$ is defined according to (2.10). First, we introduce an indicator which defines a measure for the coefficient robustness w.r.t. the partitioning into overlapping subdomains $\{\Omega_i,\ i = 1,\ldots,N\}$.

Definition 6.3.3. (Partitioning robustness indicator) *Let the overlap parameter δ_i be as in Assumption 6.2.1. For a particular partition of unity $\{\chi_i\}$ (see Definition 6.2.3), let*

$$\pi(\lambda,\mu,\{\chi_i\}) := \max_{i=1}^{N} \left\{ \delta_i^2 \| \max\{2\mu, 2\mu + d\lambda\}\, |\nabla\chi_i|^2 \|_{L^\infty(\Omega)} \right\}.$$

*Then, the **partitioning robustness indicator** is defined by*

$$\pi(\lambda,\mu) := \inf_{\{\chi_i\}\in\Pi(\{\Omega_i\})} \pi(\lambda,\mu,\{\chi_i\}). \tag{6.6}$$

Lemma 6.3.3. *Let Assumption 6.2.1 hold and let $\boldsymbol{v}^h \in \mathcal{V}^h$. Then for all $i = 1,\ldots,N$,*

$$
\begin{aligned}
|I^h(\chi_i\boldsymbol{v}^h)|_{a,\Omega}^2 &\leq C\| \max\{2\mu, 2\mu + d\lambda\}|\nabla\chi_i|^2\|_{L^\infty(\Omega_i)} \|\boldsymbol{v}^h\|_{[L^2(\Omega_i\setminus\Omega_i^\circ)]^d}^2 + |\boldsymbol{v}^h|_{a,\Omega_i}^2 \\
&= C\frac{\pi(\lambda,\mu,\{\chi_i\})}{\delta_i^2}\|\boldsymbol{v}^h\|_{[L^2(\Omega_i\setminus\Omega_i^\circ)]^d}^2 + |\boldsymbol{v}^h|_{a,\Omega_i}^2 .
\end{aligned}
$$

Proof. Let $\tau \in \mathfrak{T}_h$, and let $\chi_i(\tau)$ be the value of χ_i at the centroid of τ. For $x \in \tau$,

$$
\begin{aligned}
|I^h(\chi_i\boldsymbol{v}^h)(x)| &= |I^h((\chi_i - \chi_i(\tau))\boldsymbol{v}^h)(x) + \chi_i(\tau)\boldsymbol{v}^h(x)| \\
&\leq |I^h((\chi_i - \chi_i(\tau)\boldsymbol{v}^h)(x)| + |\boldsymbol{v}^h(x)|.
\end{aligned}
$$

Since $|\boldsymbol{u}|_{a,\tau}^2 \leq \max\{2\mu, 2\mu + d\lambda\}\,|\boldsymbol{u}|_{\varepsilon,\tau}^2\ \forall \boldsymbol{u} \in [H^1(\tau)]^d$ for an isotropic material (see section 6.3.1), we obtain

$$|I^h(\chi_i\boldsymbol{v}^h)|_{a,\tau}^2 \leq \max\{2\mu, 2\mu + d\lambda\}\,|I^h((\chi_i - \chi_i(\tau))\boldsymbol{v}^h)|_{\varepsilon,\tau}^2 + |\boldsymbol{v}^h|_{a,\tau}^2. \tag{6.7}$$

Let h_τ denote the diameter of τ. Using the shape regularity of $\mathfrak{T}_h$, we get

$$
\begin{aligned}
|I^h((\chi_i - \chi_i(\tau))\boldsymbol{v}^h)(x)| &= \Big| \sum_{j\in\mathcal{N}_h(\tau)} (\chi_i(x^j) - \chi_i(\tau))\, \boldsymbol{v}^h(x^j)\, \varphi^{j,h}(x) \Big| \\
&\leq \sum_{j\in\mathcal{N}_h(\tau)} |\chi_i(x^j) - \chi_i(\tau)|\, |\boldsymbol{v}^h(x^j)| \\
&\leq Ch_\tau \|\nabla\chi_i\|_{L^\infty(\tau)} \sum_{j\in\mathcal{N}_h(\tau)} |\boldsymbol{v}^h(x^j)| \\
&\leq Ch_\tau^{1-d/2}\|\nabla\chi_i\|_{L^\infty(\tau)}\|\boldsymbol{v}^h\|_{[L^2(\tau)]^d}.
\end{aligned}
\tag{6.8}
$$

Furthermore, we have by an inverse inequality (cf. [36]) and the shape regularity,

$$|I^h((\chi_i - \chi_i(\tau))\boldsymbol{v}^h)|_{\varepsilon,\tau} \le Ch_\tau^{-1}\|I^h((\chi_i - \chi_i(\tau))\boldsymbol{v}^h)\|_{[L^2(\tau)]^d}. \qquad (6.9)$$

Now, we combine equation (6.7) with equation (6.9). Using $|\tau| \sim h_\tau^d$, together with equation (6.8), we conclude,

$$
\begin{aligned}
|I^h(\chi_i\boldsymbol{v}^h)|_{a,\tau}^2 &\le C\max\{2\mu, 2\mu + d\lambda\}\, h_\tau^{-2}\|I^h((\chi_i - \chi_i(\tau))\boldsymbol{v}^h)\|_{[L^2(\tau)]^d}^2 + |\boldsymbol{v}^h|_{a,\tau}^2 \\
&\le C\max\{2\mu, 2\mu + d\lambda\}\, \|\nabla\chi_i\|_{L^\infty(\tau)}^2\|\boldsymbol{v}^h\|_{[L^2(\tau)]^d}^2 + |\boldsymbol{v}^h|_{a,\tau}^2.
\end{aligned}
$$

Summing over all $\tau \subset \Omega_i$ and using that $\nabla\chi_i = 0$ in $\Omega_i \setminus \Omega_i^\circ$ finishes the proof. $\qquad\square$

Before we state the main convergence result in Theorem 6.4.1, we need the following lemma, which can be found for scalar-valued functions in [45]. It is a generalization of [97, Lemma 3.10] and carries over to the case of vector-valued functions by component-wise application.

Lemma 6.3.4. *Let $\delta_i \le H_i \le \rho_i$ and let $\boldsymbol{u} \in [H^1(\Omega_{i,H_i})]^d$, $i = 1, \ldots, N$. Then it holds,*

$$\|\boldsymbol{u}\|_{[L^2(\Omega_{i,\delta_i})]^d}^2 \le C\delta_i^2\bigg((1 + \frac{H_i}{\delta_i})|\boldsymbol{u}|_{[H^1(\Omega_{i,H_i})]^d}^2 + \frac{1}{H_i\delta_i}\|\boldsymbol{u}\|_{[L^2(\Omega_{i,H_i})]^d}^2\bigg).$$

Proof. Using the shape regularity of the finite partiton $\{\Omega_i\}$, Ω_{i,δ_i} can be covered by a suitable set of Lipschitz polyhedra, that admit the application of Friedrich's inequality (cf. [97, Corollary A.15]). Summing over the finite set of polyhedra, we obtain

$$
\begin{aligned}
\|\boldsymbol{u}\|_{[L^2(\Omega_{i,\delta_i})]^d}^2 &\le C\left(\delta_i^2|\boldsymbol{u}|_{[H^1(\Omega_{i,\delta_i})]^d}^2 + \delta_i\|\boldsymbol{u}\|_{[L^2(\partial\Omega_i)]^d}^2\right) \\
&\le C\left(\delta_i^2|\boldsymbol{u}|_{[H^1(\Omega_{i,H_i})]^d}^2 + \delta_i\|\boldsymbol{u}\|_{[L^2(\partial\Omega_i)]^d}^2\right). \qquad (6.10)
\end{aligned}
$$

To bound the second term in equation (6.10), we cover Ω_{i,H_i} by a suitable set of polyhedra. Applying the trace theorem (cf. [97, Lemma A.6]) to such a polyhedron D, together with a scaling argument, we obtain

$$\|\boldsymbol{u}\|_{[L^2(\partial D)]^d}^2 \le C\left(H_i^{-1}\|\boldsymbol{u}\|_{[L^2(D)]^d}^2 + H_i|\boldsymbol{u}|_{[H^1(D)]^d}^2\right).$$

The result follows when summing over all polyhedra D and substituting into the right-hand side of equation (6.10). $\qquad\square$

Based on Lemma 6.3.4, we can prove a result which involves the semi-norm in (6.3).

Lemma 6.3.5. *Let $\delta_i \leq H_i \leq \rho_i$ and let $\boldsymbol{u} \in [H^1(\Omega_{i,H_i})]^d$, $i = 1, \ldots, N$. Then it holds,*

$$\|\boldsymbol{u}\|^2_{[L^2(\Omega_{i,\delta_i})]^d} \;\leq\; C\delta_i^2 \bigg(\Big(1 + \frac{H_i}{\delta_i}\Big) |\boldsymbol{u}|^2_{\varepsilon,(\Omega_{i,H_i})} + \frac{1}{H_i\delta_i} \|\boldsymbol{u}\|^2_{[L^2(\Omega_{i,H_i})]^d} \bigg).$$

Proof. We cover Ω_{i,H_i} by a suitable finite set of polyhedra. We denote such a polyhedron by D. Using Korn inequality in Lemma 2.5.4, the equivalence of norms in finite dimensional spaces and a scaling argument, it exists a constant C_D which only depends on the shape of D, such that

$$|\boldsymbol{u}|^2_{[H^1(D)]^d} \leq C_D \big(|\boldsymbol{u}|^2_{\varepsilon,D} + \mathrm{diam}(D)^{-2} \|\boldsymbol{u}\|^2_{[L^2(D)]^d} \big).$$

Summing over the finite set of polyhedra with $\mathrm{diam}(D) = H_i$ and using Lemma 6.3.4, we get

$$\|\boldsymbol{u}\|^2_{[L^2(\Omega_{i,\delta_i})]^d} \;\leq\; C\delta_i^2 \bigg(\Big(1 + \frac{H_i}{\delta_i}\Big) |\boldsymbol{u}|^2_{\varepsilon,(\Omega_{i,H_i})} + \Big(\frac{1}{H_i^2} + \frac{2}{\delta_i H_i}\Big) \|\boldsymbol{u}\|^2_{[L^2(\Omega_{i,H_i})]^d} \bigg).$$

Since $H_i \geq \delta_i$ by assumption, we obtain $\delta_i^{-1} H_i^{-1} \geq H_i^{-2}$ and the result follows. $\qquad \square$

6.4 Convergence Results

The following theorem provides the basis for the main convergence result in this chapter. Together with Theorem 6.4.2, it states a coefficient explicit condition number bound of the additive Schwarz preconditioned linear system.

Theorem 6.4.1. *Under Assumption 6.2.1, 6.2.2 and 6.2.3, for all $\boldsymbol{u}^h \in \mathcal{V}^h$, there exists a decomposition*

$$\boldsymbol{u}^h = \sum_{i=0}^{N} \boldsymbol{u}^i \quad with \quad \boldsymbol{u}^0 \in \mathcal{V}_0^H, \; \boldsymbol{u}^i \in \mathcal{V}^h(\Omega_i), \; i = 1, \ldots, N, \tag{6.11}$$

such that

$$\sum_{i=0}^{N} a(\boldsymbol{u}^i, \boldsymbol{u}^i) \leq C_0^2 \, a(\boldsymbol{u}^h, \boldsymbol{u}^h), \tag{6.12}$$

with

$$C_0^2 \leq C \bigg(\pi(\lambda, \mu) \, \gamma(0,1) \, \max_{i=1}^{N} \Big(1 + \frac{H_i}{\delta_i}\Big) \, + \, \gamma(\lambda, \mu) \bigg),$$

and the constant C is independent of mesh and material parameters.

Proof. Let $\{\chi_i\} \in \Pi(\{\Omega_i\})$ be any partition of unity. Define

$$\boldsymbol{u}^0 := I^H \boldsymbol{u}^h \quad \text{and} \quad \boldsymbol{u}^i = I^h(\chi_i(\boldsymbol{u}^h - \boldsymbol{u}^0)),$$

where I^H is the quasi-interpolant defined in Definition 6.3.1. Then, by Definition 6.2.3, we have $\sum_{i=1}^N \boldsymbol{u}^i = \boldsymbol{u}^h - \boldsymbol{u}^0$ and equation (6.11) follows. From Lemma 6.3.2 and the shape regularity of the coarse mesh $\mathcal{T}_H$, we obtain

$$|\boldsymbol{u}^0|_{a,\Omega}^2 = \sum_{T \in \mathcal{T}_H} |I^H \boldsymbol{u}^h|_{a,T}^2 \leq C\gamma(\lambda, \mu) \sum_{T \in \mathcal{T}_H} |\boldsymbol{u}^h|_{a,\omega_T}^2 \leq C\gamma(\lambda, \mu) |\boldsymbol{u}^h|_{a,\Omega}^2.$$

Recalling the definition of $\pi(\lambda, \mu, \{\chi_i\})$ and using Lemma 6.3.3, it follows for $i = 1, \ldots, N$,

$$|\boldsymbol{u}^i|_{a,\Omega}^2 \leq C\pi(\lambda, \mu, \{\chi_i\}) \frac{1}{\delta_i^2} \|\boldsymbol{u}^h - \boldsymbol{u}^0\|_{[L^2(\Omega_i, \delta_i)]^d}^2 + |\boldsymbol{u}^h - \boldsymbol{u}^0|_{a,\Omega_i}^2. \tag{6.13}$$

Furthermore, using Lemma 6.3.5, we obtain for $\delta_i \leq H_i$,

$$\|\boldsymbol{u}^h - \boldsymbol{u}^0\|_{[L^2(\Omega_i, \delta_i)]^d}^2 \leq C\delta_i^2 \left(\left(1 + \frac{H_i}{\delta_i}\right) |\boldsymbol{u}^h - \boldsymbol{u}^0|_{\varepsilon, \Omega_i}^2 + \frac{1}{H_i \delta_i} \|\boldsymbol{u}^h - \boldsymbol{u}^0\|_{[L^2(\Omega_i)]^d}^2 \right). \tag{6.14}$$

This estimate trivially holds if $\delta_i > H_i$. Inserting (6.14) in (6.13), we obtain

$$|\boldsymbol{u}^i|_{a,\Omega}^2 \leq C\pi(\lambda, \mu, \{\chi_i\}) \left(\left(1 + \frac{H_i}{\delta_i}\right) |\boldsymbol{u}^h - \boldsymbol{u}^0|_{\varepsilon, \Omega_i}^2 + \frac{1}{H_i \delta_i} \|\boldsymbol{u}^h - \boldsymbol{u}^0\|_{[L^2(\Omega_i)]^d}^2 \right)$$
$$+ |\boldsymbol{u}^h - \boldsymbol{u}^0|_{a,\Omega_i}^2. \tag{6.15}$$

Using the triangle inequality $|\boldsymbol{u}^h - \boldsymbol{u}^0|_{\varepsilon, \Omega_i}^2 \leq 2(|\boldsymbol{u}^h|_{\varepsilon, \Omega_i}^2 + |\boldsymbol{u}^0|_{\varepsilon, \Omega_i}^2)$ and Lemma 6.3.2 of the quasi-interpolant, we obtain

$$|\boldsymbol{u}^h - \boldsymbol{u}^0|_{\varepsilon, \Omega_i}^2 \leq C\gamma(0, 1) \sum_{T \in \mathcal{T}_H(\Omega_i)} |\boldsymbol{u}^h|_{\varepsilon, \omega_T}^2,$$

and

$$|\boldsymbol{u}^h - \boldsymbol{u}^0|_{a,\Omega_i}^2 \leq C\gamma(\lambda, \mu) \sum_{T \in \mathcal{T}_H(\Omega_i)} |\boldsymbol{u}^h|_{a,\omega_T}^2.$$

Furthermore, due to Lemma 6.3.1, we obtain

$$\|\boldsymbol{u}^h - \boldsymbol{u}^0\|^2_{[L^2(\Omega)]^d} \leq \sum_{T \in \mathcal{T}_H(\Omega_i)} \|\boldsymbol{u}^h - \boldsymbol{u}^0\|^2_{[L^2(T)]^d} \leq CH_i^2 \sum_{T \in \mathcal{T}_H(\Omega_i)} |\boldsymbol{u}^h|^2_{\varepsilon,\omega_T}.$$

We substitute the last estimates into (6.15), take the sum over the subdomains and use the assumption $|\cdot|_{\varepsilon,\Omega} \leq |\cdot|_{a,\Omega}$ (see section 6.3.1), to obtain

$$\sum_{i=0}^{N} |\boldsymbol{u}^i|^2_{a,\Omega} \leq C \left(\pi(\lambda, \mu, \{\chi_i\}) \, \gamma(0,1) \, \max_{i=1}^{N} \left(1 + \frac{H_i}{\delta_i}\right) \, + \, \gamma(\lambda, \mu) \right) |\boldsymbol{u}^h|^2_{a,\Omega}.$$

The estimate holds for any partition of unity $\{\chi_i\} \in \Pi(\{\chi_i\})$. Recalling the definition of the partitioning robustness indicator $\pi(\lambda, \mu)$, the result follows. $\qquad\square$

Theorem 6.4.2. (Condition number bound) *Let Assumption 6.2.1, 6.2.2 and 6.2.3 hold. Then, the condition number of the preconditioned linear system $M_{\mathrm{AS}}^{-1}A$ is bounded by*

$$\kappa(M_{\mathrm{AS}}^{-1}A) \leq C \left(\pi(\lambda, \mu) \, \gamma(0,1) \, \max_{i=1}^{N} \left(1 + \frac{H_i}{\delta_i}\right) \, + \, \gamma(\lambda, \mu) \right),$$

with a constant C independent of mesh parameters H_i and h, overlap parameters δ_i and material coefficients λ and μ.

Proof. According to Theorem 6.2.1, it holds $\lambda_{\max}(M_{\mathrm{AS}}^{-1}A) \leq N_C + 1$. Furthermore, from Theorem 6.2.2 and Theorem 6.4.1, we conclude that $\lambda_{\min}(M_{\mathrm{AS}}^{-1}A) \geq C_0^{-2}$. Thus, Theorem 6.4.2 follows immediately since $\kappa(M_{\mathrm{AS}}^{-1}A) = \lambda_{\max}(M_{\mathrm{AS}}^{-1}A)/\lambda_{\min}(M_{\mathrm{AS}}^{-1}A)$. $\quad\square$

Before we proceed with investigating the classes of problems for which the robustness indicator of the particular multiscale coarse spaces is well behaved, we note that these results are also applicable when the stiffness tensor is not isotropic.

Remark 6.4.1. *The definitions of the coarse space robustness indicator as well as the partitioning robustness indicator are based on the Lamé coefficients λ and μ. As such, the convergence result shown in Theorem 6.4.1 is only valid for isotropic linear elasticity. However, it can be easily extended to the bilinear form defined in equation (6.2) with anisotropic stiffness tensor $\boldsymbol{C}$. The coarse space robustness indicator $\gamma(\lambda, \mu) =: \tilde{\gamma}(\boldsymbol{C})$ only needs an adaption in its notation, i.e. $\gamma(0,1) = \tilde{\gamma}(\boldsymbol{I})$. The partitioning robustness indicator $\pi(\lambda, \mu)$ needs the following adaption. In Definition 6.3.3 and in the proof of Lemma 6.3.3, $\max\{2\mu, 2\mu + d\lambda\}$ needs to be replaced by the largest eigenvalue $c_{\max}$ of the stiffness tensor as mentioned in section 6.3.1. Note that, by*

assumption, such an upper bound is available locally in each element $\tau \in \mathfrak{T}_h$ such that $(\boldsymbol{C} : \boldsymbol{\varepsilon}(\boldsymbol{v})) : \boldsymbol{\varepsilon}(\boldsymbol{v}) \leq c_{\max}(\tau)\,\boldsymbol{\varepsilon}(\boldsymbol{v}) : \boldsymbol{\varepsilon}(\boldsymbol{v})$ a.e. for all $v \in [H^1(\tau)]^d$. W.l.o.g., we also require the minimal eigenvalue of $\boldsymbol{C}$ to be larger than 1.

Assuming that the overlap δ_i of the subdomain $\Omega_i, i = 1, \ldots, N$, and its neighbors is large enough such that each high contrast inclusion lies in at least one subdomain, the partitioning robustness indicator $\pi(\lambda, \mu)$ is well behaved, i.e. it is bounded independently of the magnitude of the coefficient jumps. However, to obtain a robust two-level method, the coarse space robustness indicator $\gamma(\lambda, \mu)$ implies the construction of basis functions with minimal energy.

6.5 Coarsening Strategies

In the next section we present numerical experiments in 3D using the multiscale coarsening strategies introduced in the previous chapters. Next to the vector-valued (i) linear coarse spaces, we also apply (ii) multiscale finite element coarse spaces with linear and oscillatory boundary conditions as well as (iii) energy minimizing coarse spaces for linear elasticity. Having summarized the construction of the multiscale coarse spaces in chapter 3, 4 and 5 in detail, in the following, we discuss how their coarse space robustness indicators $\gamma(\lambda, \mu)$ behave in terms of the heterogeneities in the PDE coefficients λ and μ. In section 6.6, we then show numerically that the robustness of each coarse space is correctly predicted by the novel coefficient robustness indicators, they clearly indicate why the developed multiscale coarsening strategies should be preferred over standard vector-valued piecewise linear coarse spaces.

6.5.1 Linear Coarsening

Let $\phi_m^{p,\mathrm{H}} = \phi_m^{p,\mathrm{L}}$ be a vector-valued piecewise linear coarse basis function on $\mathfrak{T}_H$. Its values are uniquely determined by the nodal constraints $\phi_{mk}^{p,\mathrm{L}}(x^q) = \delta_{pq}\,\delta_{mk}$, $p \in \bar{\mathcal{N}}_H$, $k \in \{1, \ldots, 3\}$, given in Assumption 6.2.2 **(C1)**. Assumptions 6.2.2 **(C2)** - **(C3)** follow immediately, while **(C4)** and **(C5)** hold since the space of rigid body modes $\mathcal{RBM}(\bar{\Omega})$ is a subspace of the space of piecewise linear vector-valued functions. It can be verified that

$$\left|\phi_m^{p,\mathrm{L}}\right|_a^2 = \int_{\omega_p} 2\mu\,\varepsilon^2(\phi_m^{p,\mathrm{L}}) + \lambda(\nabla \cdot \phi_m^{p,\mathrm{L}})^2\,dx \,\sim\, H_p^{-2} \sum_{\tau \subset \bar{\omega}_p} \int_\tau 4\mu + \lambda\,dx, \qquad (6.16)$$

where H_p is the local coarse mesh diameter. Thus, the coarse space robustness indicator $\gamma^{\mathrm{L}}(\lambda, \mu)$ is unbounded if λ or $\mu \to \infty$ in some $\tau \in \mathcal{T}_h$. This explains the poor performance when linear coarsening is used when large coefficient jumps occur.

6.5.2 Multiscale Coarsening with Linear Boundary Conditions

The multiscale coarse space with vector-valued linear boundary conditions performs much better than linear coarsening when coefficient jumps occur in the interior of coarse elements (see chapter 3). An important feature of multiscale-FE coarse spaces is their energy minimizing property in the interior of coarse elements. It follows from the definition of a linear multiscale-FE basis function $\phi_m^{p,\mathrm{MsL}}$ in $T \in \mathcal{T}_H$,

$$
\begin{aligned}
a_T(\phi_m^{p,\mathrm{MsL}}, \boldsymbol{v}^h) &= 0 && \forall \, \boldsymbol{v}^h \in \mathcal{V}^h(T) \\
\phi_m^{p,\mathrm{MsL}} &= \phi_m^{p,\mathrm{L}} && \text{on } \partial T,
\end{aligned}
$$

that

$$
\left|\phi_m^{p,\mathrm{MsL}}\right|_{a,T} \leq \left|\psi\right|_{a,T} \quad \forall \, \psi \in \mathcal{V}^h(T) \quad \text{with} \quad \psi = \phi_m^{p,\mathrm{L}} \text{ on } \partial T. \tag{6.17}
$$

Thus, it holds $\gamma^{\mathrm{MsL}}(\lambda, \mu) \leq \gamma^{\mathrm{L}}(\lambda, \mu)$. The property in (6.17) allows that the coarse space robustness indicator $\gamma^{\mathrm{MsL}}(\lambda, \mu)$ can be bounded independently of the material coefficients if coefficient jumps appear in the interior of coarse elements.

According to the analysis in chapter 3, it is clear that the coarse space $\mathcal{V}^{\mathrm{MsL}}$ satisfies Assumption 6.2.2, *(C1)* - *(C5)*. Assumption *(C1)* follows since $\phi_m^{p,\mathrm{MsL}}$ coincides with a vector-valued linear coarse basis function on ∂T, *(C4)* and *(C5)* hold since the PDE-harmonic extension of vector-valued linear boundary data to the interior of coarse elements guarantees that the rigid body modes are preserved.

Remark 6.5.1. *For scalar elliptic PDEs, it its shown in [45] that the coarse space robustness indicator γ^{MsL} is bounded independently of the material contrast assuming that the high contrast inclusions have a distance to coarse element boundaries of at least one layer of fine elements $\tau \in \mathcal{T}_h$. The argument used in the proof in [45] can also be applied to linear elasticity. That is, we can construct a function ψ which coincides with $\phi_m^{p,\mathrm{L}}$ on ∂T and vanishes outside the near boundary strip of width $\Delta_{\lambda,\mu} \geq h$ in which λ and μ appear to be small. The energy of this function ψ is bounded independently of the high contrast coefficients since the constructed function is zero there where the PDE coefficients are large. Using the energy minimizing property of the multiscale coarse*

space in equation (6.17) *yields the bound for* $\gamma^{\mathrm{MsL}}(\lambda, \mu)$. *Note that the bound we obtain by following these arguments might be pessimistic as it depends on the smallest distance of the high contrast inclusions in* $T \in \mathcal{T}_H$ *to the element boundary* ∂T *by* $\Delta_{\lambda,\mu}^{-2}$.

We may conclude that $\gamma^{\mathrm{MsL}}(\lambda, \mu)$ remains bounded if λ and μ are small in the strip of width proportional to H_T near the boundaries ∂T of coarse elements $T \in \mathcal{T}_H$. The linear multiscale basis allows robust two-level convergence of the additive Schwarz preconditioned system, given that the coarse mesh can be constructed such that large coefficient variations appear exclusively in the interior of coarse elements. Robustness may be lost as soon as high contrast regions touch or cross coarse element boundaries. Since a basis function $\phi_m^{p,\mathrm{MsL}}$ is linear on ∂T, we know from equation (6.16) that $\gamma^{\mathrm{MsL}}(\lambda, \mu)$ grows unboundedly as soon as $\lambda \to \infty$ or $\mu \to \infty$ in some $\tau \in \mathcal{T}_h$ which touches ∂T, $T \in T_H$.

6.5.3 Multiscale Coarsening with Oscillatory Boundary Conditions

As we have seen in chapter 4, this dependence may be overcome by adapting the boundary data to the underlying heterogeneities. The oscillatory multiscale basis function $\phi_m^{p,\mathrm{MsO}}$ is defined such that for each $T \in \mathcal{T}_H$,

$$
\begin{aligned}
a_T(\phi_m^{p,\mathrm{MsL}}, \boldsymbol{v}^h) &= 0 & \forall\, \boldsymbol{v}^h \in \mathcal{V}^h(T) \\
\phi_m^{p,\mathrm{MsL}} &= \eta_m^{p,T} & \text{on } \partial T,
\end{aligned}
\tag{6.18}
$$

where the "oscillatory boundary data"

$$
\eta_m^{p,T} \;:\; \partial T \to \mathbb{R}^3
$$

are constructed following Algorithm 4.1 by solving reduced problems on the edges and faces of coarse elements.

The oscillatory multiscale finite element method hierarchically applies the local energy minimizing property in (6.17). More precisely, computing subproblems on the edges and faces of coarse elements yields boundary data which also obey a minimal energy property (w.r.t. the reduced operator) on a k-dimensional ($k < d$) manifold, similar to that in (6.17). For most out of all possible scenarios of coefficient distributions, we may deduce that $\gamma^{\mathrm{MsO}} \leq \gamma^{\mathrm{MsL}}$.

6. CONVERGENCE ANALYSIS

The boundary conditions of the oscillatory multiscale finite element basis are imposed in (4.3) such that the nodal constraints in Assumption 6.2.2 *(C1)* are satisfied. Following the analysis in chapter 4, Assumptions 6.2.2, *(C2)* - *(C4)* are also fulfilled. As mentioned in section 4.5, not all the rigid body rotations can be extracted from solving lower-dimensional problems on the coarse element boundaries, the multiscale coarse space with oscillatory boundary conditions satisfies Assumption 6.2.2 *(C5)* approximately.

Considering the scalar elliptic case, it its shown in [45] that the coarse space robustness indicator γ^{MsO} can be bounded independently of the contrast in the material parameters for certain classes of heterogeneous problems. A proof is provided when high contrast regions can be characterized as a union of disjoint "islands". The proof is quite technical and is presented for problems in 2D under a few assumptions [45, Assumption 4.3]. It applies the energy minimizing property by constructing a particular finite element function for which an energy bound is presented. The function is obtained by (i) extending the oscillatory boundary data (by a linear function) to the interior of high contrast regions which touch the coarse element boundary, (ii) extending the resulting function to the remaining part of the element interior using the trace-theorem and further by (iii) applying a H^1-stable quasi-interpolant to obtain a piecewise linear function which preserves the boundary values which are obtained in (i). While some of these assumptions which are required in the proof ([45, Assumption 4.3]) are of purely technical nature, one of them reveals the class of problems for which an energy bound cannot be obtained.

To specify this restriction in more detail, we consider a high contrast region Υ, a subset of $T \subset \mathcal{T}_H$ which shall be simply connected and touch the boundary ∂T. We denote by $\Upsilon \mid_{\partial T}$ the intersection of the high contrast region with ∂T. The assumption stated in [45, Assumption 4.3] says that $\Upsilon \mid_{\partial T}$ must be simply connected on ∂T. Indeed, if the latter is not satisfied, the energy of the basis function may not be bounded.

To see this, we examine a scenario in 3D where the high contrast region touches two faces of the tetrahedral element, without touching the edge which connects these two faces. Hence, $\Upsilon \mid_{\partial T}$ is not simply connected (on ∂T). Depending on the precise boundary values on $\Upsilon \mid_{\partial T}$, extending the boundary data from the two faces to the coarse element interior may introduce a large gradient in the oscillatory multiscale-FE basis function between the two faces inside the high contrast region Υ. In this case, the energy of

the multiscale-FE basis function may depend explicitly on the material coefficient in Υ. Inversely, if $\Upsilon \mid_{\partial T}$ is simply connected, the oscillatory boundary data may be such that their gradient is low on $\Upsilon \mid_{\partial T}$ (this typically holds for scalar elliptic PDEs and elasticity problems due to the energy minimizing property w.r.t. the restricted PDE on ∂T), the boundary values on the two faces are almost constant and do not introduce large gradients in the basis functions when extended to the coarse element interior.

For linear elasticity problems and variations in the Young's modulus, a similar strategy can be used. In 2D, the energy of the basis can be approximated by applying the concept provided for scalar problems separately to each component of the vector-field in $\mathbb{R}^2$. However, in $\mathbb{R}^3$, such an estimate may be too pessimistic. This difficulty appears in 3D on the faces of coarse elements since the boundary data on a face may prescribe a rotation of a stiff inclusion which touches the interior of a face but none of the edges. The pessimistic energy estimate in such a scenario can be avoided by measuring the energy of the finite element function in the high contrast regions directly in the energy-norm, which introduces further technicalities.

Remark 6.5.2. *To summarize, we shall say that energy bounds similar to the ones proven for scalar elliptic PDEs in [45] can be achieved also for elasticity problems with variations in the Young's modulus. Restrictions similar to them in [45, Assumption 4.3] apply. The requirement of $\Upsilon \mid_{\partial T}$ (intersection of high contrast region with the coarse element boundary) to be simply connected can be quite restrictive in 3D when tetrahedral elements are used, especially in the vicinity of sharp edges and corners. This specific circumstance does not hold exclusively for linear elasticity problems but applies to scalar elliptic problems as well. In the context of the energy bound we may conclude that hexahedral coarse meshes may be preferred as they reduce the amount of element boundaries which are introduced when tetrahedral coarse meshes are used.*

6.5.4 Energy Minimizing Coarsening

The explicit dependence of the coarse space robustness indicator in equation (6.5) on the energy of the basis functions encourages the construction of basis function with minimal energy as presented in chapter 5. The energy minimizing coarse basis function $\phi_m^{p,\mathrm{H}} = \phi_m^{p,\mathrm{EM}}$ is defined such that

$$\sum_{p \in \bar{\mathcal{N}}_H} \left| \phi_m^{p,\mathrm{EM}} \right|_{a,\Omega}^2 \to \min, \quad \text{subject to} \quad \sum_{p \in \bar{\mathcal{N}}_H} \phi_{mk}^{p,\mathrm{EM}} = \delta_{mk} \quad k = 1, 2, 3.$$

The coarse space satisfies Assumption 6.2.2, **(C1) - (C4)**. In general, the global rotations are not preserved exactly and thus, assumption **(C5)** is fulfilled approximately. It is proven in Lemma 5.5.1 that the coarse space presented here is locally PDE-harmonic in the interior of coarse elements. As such, it also has a local energy minimizing property in the interior of coarse elements. However, the boundary conditions of the energy minimizing coarse basis functions are not explicitely given, "optimal boundary conditions" are computed implicitly by solving the global Lagrange multiplier system in equation (5.7) for each $m \in \{1, 2, 3\}$.

This implies that for the construction of the boundary values of the energy minimizing basis, not only the local coefficient distribution (e.g. on ∂T) is taken into account. Instead, the main difference to the oscillatory multiscale finite element basis is that the coefficient distribution is considered at least in a small neighborhood of the supports of a particular basis function. We may point out here that this circumstance is confirmed by the robustness of the one-level additive Schwarz preconditioner for the Lagrange multiplier system in section 5.7. The local corrections in a small neighbourhood of $\bar{\omega}_p$ (see Figure 5.1) ensure a robust construction of the boundary values for the energy minimizing basis functions.

Provided that high contrast regions are small compared to the coarse mesh diameter, the coarse space robustness indicator $\gamma^{\mathrm{EM}}(\lambda, \mu)$ is in most cases well behaved. It holds the relation $c^{-1}\gamma^{\mathrm{EM}}(\lambda, \mu) \leq \gamma^{\mathrm{MsO}}(\lambda, \mu)$, where a small constant $c \geq 1$ in the first inequality may be required since the coarse basis is defined by minimizing the sum of their energies and not their maximum as it appears in the coarse space robustness indicator.

6.6 Numerical Results

In this section, we show numerically the sharpness of the theoretical bounds given in Theorem 6.4.2. We give a series of examples involving binary composites and apply the developed multiscale coarsening strategies within the two-level additive Schwarz preconditioner. We perform the simulations on domains $\bar{\Omega} = [0, 1] \times [0, 1] \times [0, L], L > 0$, with regular fine and coarse triangular mesh $\mathcal{T}_h$ and $\mathcal{T}_H$ of uniform mesh size h and H, respectively. According to the description in chapter 2.3.2, both meshes are constructed from an initial voxel geometry ($1/h \times 1/h \times H/h$ voxels), where each voxel

is further decomposed into five tetrahedra. If not mentioned otherwise, the overlapping subdomains $\Omega_i, i = 1, \ldots, N$, are chosen to consist of a coarse element $T \in \mathcal{T}_H$, extended by a few layers of fine elements $\tau \in \mathcal{T}_h$. The overlap width $\delta > 0$ is specified as a multiple of h.

We show condition numbers as well as iteration numbers of the PCG algorithm. The stopping criterion is to reduce the preconditioned initial residual by six orders of magnitude. The estimated condition numbers $\kappa(M_{AS}^{-1}A)$ are computed based on the three term recurrence which is implicitly formed by the coefficients within the PCG algorithm (cf. [89]).

We consider different heterogeneous media, each of which consists of a matrix material with small inclusions. If not mentioned otherwise, the coefficients of the matrix material are chosen to be $\mu_{\mathrm{mat}} = 1$ and $\lambda_{\mathrm{mat}} = \frac{2}{3}$ in the rest of this section. Keeping the coefficients of the matrix material fixed, we perform tests in which we either vary the stiffness of the inclusions or we let them approach the incompressible limit. Note that the latter is not in contradiction with Remark 2.2.1 as the matrix material itself is not incompressible. To indicate variations in the material stiffness, we denote by Δ_E the ratio between stiff or soft inclusions and the matrix material, i.e. the material coefficients are such that $\mu_{\mathrm{inc}} = \Delta_E \mu_{\mathrm{mat}}$ and $\lambda_{\mathrm{inc}} = \Delta_E \lambda_{\mathrm{mat}}$. Note that this is equivalent to varying the Young's modulus of the inclusions while the Poisson number remains unchanged. Letting $\lambda_{\mathrm{inc}} \to \infty$, we test the performance of the preconditioners when the inclusions tend to become incompressible, i.e. $\nu \to \frac{1}{2}$ (cf. the relation between λ, μ and E, ν in equation (2.5)).

In a first numerical test, we assume that the discontinuities in the material coefficients are isolated, such that the material jumps occur only in the interior of coarse elements. Figure 6.3 shows such a binary composite (medium 1) with one tetrahedral inclusion inside each coarse tetrahedron. The inclusions in the interior are of the same form as the coarse elements in which they appear and have a distance to the coarse element boundaries of two layers of fine elements. First, we use linear coarsening and observe the condition number of the preconditioned matrix under variations in the material coefficients. The coefficients of the inclusions vary as shown in Table 6.1. Indicated is the condition number of the preconditioned matrix and the robustness indicator $\gamma^{\mathrm{L}}(\lambda, \mu)$ for the linear coarse space. Table 6.1 (a) corresponds to increasing the Young's modulus of the inclusions, while in Table 6.1 (b), the Poisson number ν of the inclusions
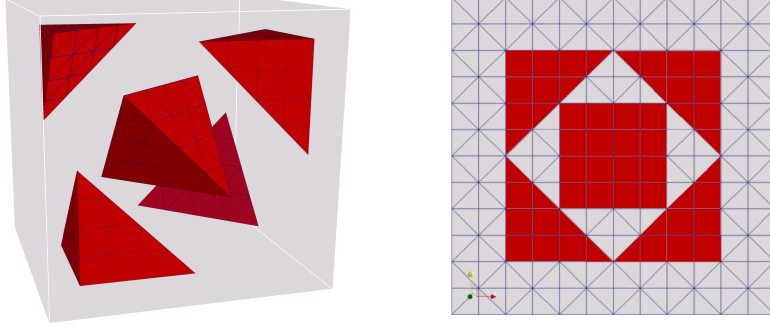
Figure 6.3: Medium 1: binary composite; matrix material (grey) and tetrahedral inclusions (red) in the interior of the coarse elements; discretization in $12 \times 12 \times 12$ voxels; each voxel is decomposed into 5 tetrahedra; 3D view (left) and 2D projection with fine mesh, showing the position of the inclusions (right);

approach the incompressible limit ($\nu \to \frac{1}{2}$). The coarse space robustness indicator is unbounded and indicates the loss of robustness of the linear coarse space with increasing contrast. It holds $\gamma^{\mathrm{L}}(\lambda, \mu) \to \infty$ for $\lambda_{\mathrm{inc}} \to \infty$ or $\mu_{\mathrm{inc}} \to \infty$ and the condition number increases with the contrast in the material parameters.

Δ_E	$\kappa(M_{AS}^{-1}A)$	$\gamma^{\mathrm{L}}(\lambda, \mu)$
10^0	40	$5.0 \cdot 10^0$
10^3	546	$1.9 \cdot 10^2$
10^6	2240	$1.85 \cdot 10^5$
10^9	2240	$1.85 \cdot 10^8$

(a)

λ_{inc}	$\kappa(M_{AS}^{-1}A)$	$\gamma^{\mathrm{L}}(\lambda, \mu)$
10^0	40	$5.0 \cdot 10^0$
10^3	220	$4.2 \cdot 10^1$
10^6	1870	$3.7 \cdot 10^4$
10^9	1890	$3.7 \cdot 10^7$

(b)

Table 6.1: Condition numbers of the preconditioned matrix on medium 1 with linear coarsening; $h = 1/240$, $H = 12h$, $\delta = 2h$; (a): $\lambda_{\mathrm{mat}} = 1$; (b): $\lambda_{\mathrm{mat}} = \mu_{\mathrm{inc}} = 1$

We repeat this experiment and replace the vector-valued linear coarse space with the multiscale-FE coarse space. Note that on medium 1, the multiscale-FE coarse spaces with linear and oscillatory boundary conditions coincide since the medium appears homogeneous on the faces and edges of coarse elements. Inhomogeneities occur only in the interior of coarse elements. Table 6.2 shows the condition number of the preconditioned matrix using the multiscale finite element coarse basis, the material coefficients coincide with the ones presented for the vector-valued linear coarse space in Table 6.1. Since the inclusions in medium 1 have a distance to the coarse element boundaries of at least one layer of fine elements, the multiscale-FE basis is bounded in energy as the material contrast increases. This is reflected by the coarse space robustness indicator,

Δ_E	$\kappa(M_{AS}^{-1}A)$	$\gamma^{\mathrm{MsL}}(\lambda, \mu)$
10^0	40	5.0
10^3	42	5.9
10^6	42	6.0
10^9	42	6.0

(a)

λ_{inc}	$\kappa(M_{AS}^{-1}A)$	$\gamma^{\mathrm{MsL}}(\lambda, \mu)$
10^0	40.0	5.0
10^3	44.5	5.2
10^6	44.5	5.2
10^9	44.5	5.2

(b)

Table 6.2: Condition numbers of the preconditioned matrix on medium 1 with multiscale-FE coarsening; $h = 1/240$, $H = 12h$, $\delta = 2h$; (a): $\lambda_{\mathrm{mat}} = 1$; (b): $\lambda_{\mathrm{mat}} = \mu_{\mathrm{inc}} = 1$

it holds $\gamma^{\mathrm{MsL}}(\lambda, \mu) \leq C$ independent of λ_{inc} and μ_{inc}. We see that $\gamma^{\mathrm{MsL}}(\lambda, \mu)$ correctly indicates the robustness of the method. Note that, representing λ and μ by the equivalent counterparts E and ν, the condition number of the preconditioned system is bounded independently of variations in the Young's modulus as well as the Poisson ratio of the inclusions which may even approach the incompressible limit $\nu_{\mathrm{inc}} \to \frac{1}{2}$. Now, we observe the sharpness of the bound in Theorem 6.4.2 w.r.t. the partitioning robustness indicator $\pi(\lambda, \mu)$, defined in equation (6.6). Therefore, we consider different choices of the overlap width of the subdomains $\{\Omega_i, i = 1, \ldots, N\}$ on medium 2 where the discontinuities in the material coefficients are not isolated, but occur on any of the coarse element boundaries. Figure 6.4 shows such a binary composite with inclusions positioned in an alternating structured ordering.
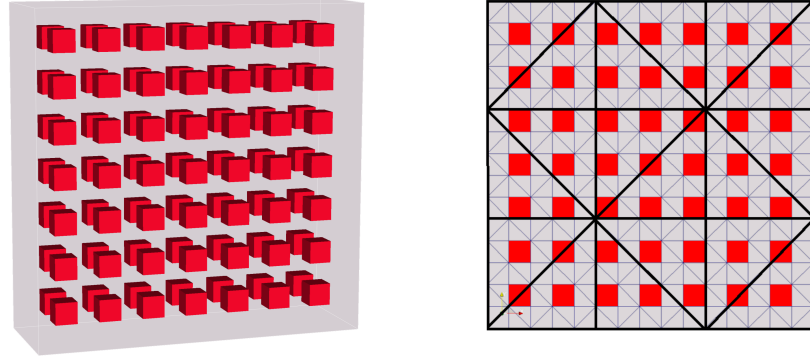
Figure 6.4: Medium 2: binary composite; matrix material (grey) and $1 \times 1 \times 1$ inclusions (red); Discretization with $15 \times 15 \times 5$ voxels (left), 2D projection with fine & coarse mesh (right); inclusions touch the boundaries of coarse tetrahedral elements

In a first experiment, we choose each $\Omega_i, i = 1, \ldots, N$ to have a minimal overlap $\delta = 1h$ with its neighbours. Table 6.3 shows the condition numbers of the preconditioned matrix for different coarsening strategies and $\Delta_E \to \infty$. If $\delta = 1h$, any partition

Δ_E	LIN	MsL	EM	$\gamma^{\mathrm{EM}}(\lambda, \mu)$
10^0	$3.8 \cdot 10^1$	$3.8 \cdot 10^1$	$5.8 \cdot 10^1$	5.3
10^3	$2.1 \cdot 10^3$	$2.2 \cdot 10^3$	$2.2 \cdot 10^3$	11.1
10^6	$1.8 \cdot 10^6$	$1.9 \cdot 10^6$	$2.0 \cdot 10^6$	11.2
10^9	$1.3 \cdot 10^9$	$1.2 \cdot 10^9$	$1.3 \cdot 10^9$	11.2

Table 6.3: Condition number of preconditioned matrix on medium 2: $h = 1/225$, $H = 5h$, $\delta = 1h$

of unity $\{\chi_i, i = 1, \ldots, N\}$ subordinate to the covering $\{\Omega_i, i = 1, \ldots, N\}$ has high gradients at some high contrast regions along the coarse element boundaries. The partitioning robustness indicator remains unbounded, we have $\pi(\lambda, \mu) = O(\Delta_E)$. For any coarsening strategy, the condition numbers shown in Table 6.3 grow with the material contrast. The small overlap width deteriorates convergence and the condition number is dominated by the partitioning robustness indicator, even for the energy minimizing coarse space for which the coarse space robustness indicator $\gamma^{\mathrm{EM}}(\lambda, \mu)$ is bounded.

We repeat the experiment by increasing the overlap width of the subdomains from $\delta = 1h$ to $\delta = 2h$. Table 6.4 shows the condition numbers of the preconditioned matrix for increasing contrast $\Delta_E \to \infty$. For $\delta = 2h$, there exists a partition of unity $\{\chi_i, i = 1, \ldots, N\}$ subordinate to the covering $\{\Omega_i, i = 1, \ldots, N\}$ that allows low gradients in any area where λ or μ is large and the partitioning robustness indicator $\pi(\lambda, \mu)$ remains bounded independently of the contrast. We see that the condition numbers in Table 6.4 are determined by the coarse space robustness indicators.

Δ_E	LIN	MsL	EM	$\gamma^{\mathrm{EM}}(\lambda, \mu)$
10^0	16	16	18	5.3
10^3	716	407	25	11.1
10^6	2560	2550	26	11.2
10^9	2560	2580	26	11.2

Table 6.4: Condition number of preconditioned matrix for medium 2: $h = 1/225$, $H = 5h$, $\delta = 2h$

Linear and multiscale-FE coarse space with linear boundary conditions are unbounded in energy. According to equation (6.16), any inclusion has a high (coefficient dependent)

Δ_E	$\gamma^{\mathrm{L}}(\lambda, \mu)$	$\gamma^{\mathrm{MsL}}(\lambda, \mu)$	$\gamma^{\mathrm{EM}}(\lambda, \mu)$
10^0	$4.6 \cdot 10^0$	$4.6 \cdot 10^0$	5.3
10^3	$4.7 \cdot 10^2$	$2.8 \cdot 10^2$	11.1
10^6	$4.6 \cdot 10^5$	$2.7 \cdot 10^5$	11.2
10^9	$4.6 \cdot 10^8$	$2.7 \cdot 10^8$	11.2

Table 6.5: Coarse space robustness indicators for linear, multiscale-FE and energy minimizing coarse space on medium 2

contribution to the energy of the vector-valued linear basis. For the linear multiscale-FE coarse space, only inclusions which touch the coarse element boundaries contribute to the total energy with a factor proportional to the material coefficient. Inclusions in the interior of coarse elements are captured properly. Only the energy minimizing coarse space ensures a contrast independent bound of the energy. Table 6.5 summarizes the robustness indicators for linear, linear multiscale-FE and energy minimizing coarse space.

For the third medium, we do not impose any restriction on the position of the small inclusions and consider a binary medium whose inclusions are uniformly distributed (see Figure 6.5. Table 6.6 shows the condition numbers for different contrasts Δ_E
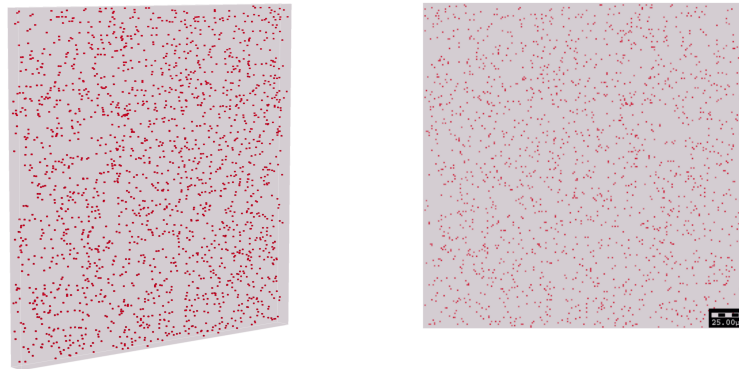
Figure 6.5: Medium 3: binary composite discretized with $240 \times 240 \times 12$ voxels; matrix material (grey) and $1 \times 1 \times 1$ inclusions (red) uniformly distributed; 3D view (left) and 2D projection showing the position of the inclusions (right)

which varies over several orders of magnitude. The overlapping subdomains are formed by the interior of a union of coarse elements, such that they coincide with the supports of the basis functions. This leads to an overlap width $\delta = O(H)$, which is often referred

Δ_E	LIN	MsL	EM	$\gamma^{\mathrm{EM}}(\lambda, \mu)$
10^0	4.4	4.4	4.4	5.5
10^3	19.3	8.4	4.8	5.7
10^6	414	373	5.0	5.8
10^9	427	465	5.0	5.8

Table 6.6: Condition numbers on medium 3; $h = 1/240$, $H = 12h$, generous overlap; linear, multiscale-FE and energy minimizing coarsening for different Δ_E

to as a *generous overlap*. Again, $\gamma^{\mathrm{EM}}(\lambda, \mu)$ correctly indicates the robustness of the energy minimizing coarse space for the randomly distributed inclusions.

In the next set of numerical tests we investigate the robustness of the multiscale-FE basis with oscillatory boundary conditions on medium 4 in Figure 6.6. The medium contains a coarse block of $7 \times 7 \times 7$ voxels which alternates its orientation. The distribution of the inclusions is shown in more detail in Figure 6.7. At each slice in the plane normal to X_3, the position of the inclusions above and below this level are indicated with dark and shaded red, respectively. The material parameters of the matrix material are given by $\lambda_{\mathrm{mat}} = \mu_{\mathrm{mat}} = 1$, for the inclusions we have $\lambda_{\mathrm{inc}} = \mu_{\mathrm{inc}} = \Delta_E$.
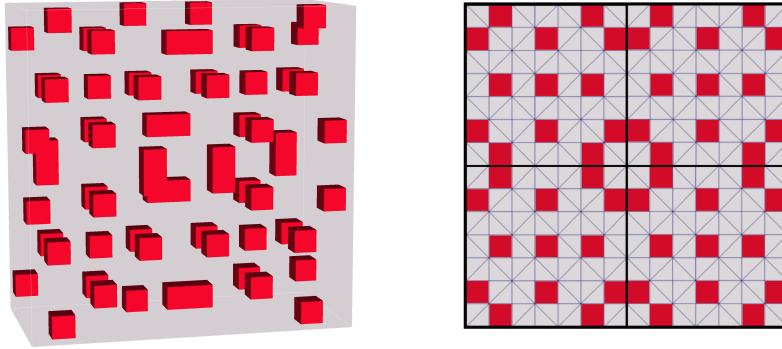
Figure 6.6: Medium 4: binary composite; matrix material (grey) and $1 \times 1 \times 1$ inclusions (red); discretization in $14 \times 14 \times 7$ voxels (left); 2D projection onto the (X_1, X_2)-plane with position of the inclusion (right); each coarse block is decomposed in 5 tetrahedrons; inclusions touch the boundaries of coarse tetrahedral elements

The results show that the multiscale finite element coarse space with oscillatory boundary conditions gives coefficient-independent condition numbers. The PDE-harmonic extension of the oscillatory boundary data to the interior of the coarse elements allow the energy of the basis functions to be bounded and $\gamma^{\mathrm{MsO}}(\lambda, \mu)$ correctly predicts the
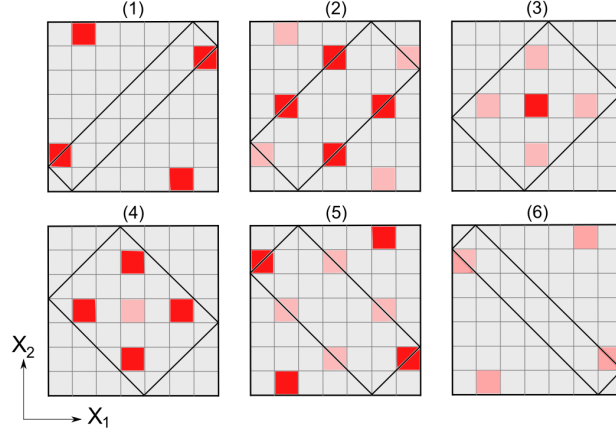
Figure 6.7: 2D slices (at $X_3 = l\,h$, $l \in \{1, \ldots, 6\}$) of a coarse block of $7 \times 7 \times 7$ voxels of medium 4; boundaries of coarse tetrahedral elements (black), matrix material (grey) and $1 \times 1 \times 1$ inclusions (red); inclusions touch the slice from below (shaded red) or top (dark red).

robustness of the preconditioner.

Δ_E	LIN	MsL	MsO	γ^{MsO}
10^0	25	25	25	4.8
10^3	426	233	25	6.8
10^6	965	955	25	6.9
10^9	970	955	25	6.9

Table 6.7: Condition number of preconditioned matrix on medium 4: $H = 7h$, $\delta = 2h$

6.7 Conclusions

In this work, we present a novel analysis for two-level additive Schwarz domain decomposition preconditioners for multiscale problems which arise from the finite element discretization of the PDE system of linear elasticity. Of main interest in our analysis is the application to highly heterogeneous, particle reinforced composite materials in three spatial dimensions. For scalar elliptic PDEs of multiscale character, such an analysis is already provided by Graham, Lechner and Scheichl in [45]. The work presented here can be seen as an extension of their work from scalar elliptic PDEs to the PDE system of linear elasticity. We present coefficient-explicit bounds for the condition number of the two-level additive Schwarz preconditioned linear system. These estimates give

sharper bounds than existing ones, without requiring that the coefficients are resolved by the coarse mesh. The bounds show a dependence of the condition number on the energy of the coarse basis functions, the coarse mesh and the overlap parameters. The coarse space is assumed to contain the rigid body modes and can be considered as a generalization of the space of vector-valued piecewise linear functions on a coarse tri-angulation. The sharpness of the theoretical findings is demonstrated numerically by performing tests on binary media using linear, multiscale-FE and energy minimizing coarse spaces. The results show also that, using an oscillatory multiscale finite element coarse space, robustness w.r.t. variations in the material coefficients can be achieved not only for the class of problems where inclusions of high stiffness are isolated in the interior of coarse elements, but also when inclusions cross coarse element boundaries.

7

Parallelization: Application to Multi-Phase Elastic Composites

As we can conclude from the model problems considered in the previous chapters, energy minimizing coarse spaces are robust for a larger class of problems than e.g. the multiscale finite element coarse space with vector-valued linear boundary conditions. The latter shows only poor performance when inclusions of high stiffness touch coarse element bondaries. In return, setting up the energy minimizing basis functions is, due to the global problems which need to be solved, computationally more costly and shows only poor scalability in a parallel implementation. The computation of the multiscale finite element basis requires only local problems to be solved and is as such parallelizable with optimal scaling properties. According to the considerations in chapter 4 and chapter 6, the poor robustness properties of the linear multiscale-FE coarse space can be circumvented to some extent by constructing boundary-values for the multiscale finite element basis functions which are better adapted to the heterogeneities in the PDE coefficients. Moreover, a coarse hexahedral mesh should be preferred over tetrahedral coarse meshes as it significantly reduces the number of edges and faces, which is essential for the robustness of the oscillatory multiscale finite element basis. This requires no further adaptions of Algorithm 4.1 presented in section 4.3.

In this chapter we combine the results presented in the previous chapters to perform material simulations on large heterogeneous multi-phase composites. More precisely, we present an efficient, scalable and memory saving MPI (message passing interface, cf. [39]) parallel implementation of the Preconditioned Conjugate Gradient algorithm,

using the two-level additive Schwarz preconditioner with coarse space given by the oscillatory multiscale finite element basis on a coarse hexahedral mesh. We investigate the scalability of the implementation as well as the robustness of the preconditioner on different test problems and give an application to large composites which are discretized by more than 10^8 degrees of freedom.

One of the main challenges in the implementation are restrictions of the computer architecture in the number of computational nodes itself and, of even greater importance, the resticted memory capacity at each particular node. The implementation of the MPI-parallelized method for distributed memory architectures needs to be adapted to these constraints. The key requirements are

- Efficiency and good parallel scalability on up to 2^7 processors;

- Memory saving implementation;

The latter is achieved by reassembling local stiffness matrices, which decreases the required memory as the global stiffness matrix in (2.14) is stored only on local subsets of the entire domain Ω. Before facing these issues in more detail in section 7.3, we state the overall setting in section 7.1 and summarize the main components of the parallelization in section 7.2. Numerical results are given in section 7.4, followed by the finalizing conclusions in section 7.5.

7.1 Preliminaries

We are again in the setting as stated in chapter 2 and use the discretization provided in section 2.2. Particularly, we apply the tetrahedral fine mesh $\mathfrak{T}_h$ in the form as introduced in section 2.3.2. However, within this chapter, we replace the coarse tetrahedral elements and use a hexahedral coarse mesh $\mathfrak{T}_H$ for the construction of the basis functions instead. The coarse elements, denoted by $T \in \mathfrak{T}_H$, are formed by an agglomeration of fine elements $\tau \in \mathfrak{T}_h$ to coarse blocks of size $H \times H \times H$. We then construct the multiscale finite element basis with oscillatory boundary conditions as in chapter 4 by following Algorithm 4.1 for a hexahedral coarse mesh.

We use exactly the same method in parallel than we used before in the sequential version, no specific variations in the PCG algorithm are pursued. Also, we apply the classical two-level additive Schwarz preconditioner in the form presented in (2.23).

Other variants such as restricted additive Schwarz (RAS) as introduced in [20] are sometimes preferred due to a better parallel scaling behaviour. However, the RAS preconditioner is not symmetric and cannot be used within the CG algorithm. It can be combined with other Krylov subscape methods such as GMRES [89], which requires extra memory for storing additional vectors which are not required for the CG method.

7.2 Aspects of the Parallelization

We summarize in detail the main components which are affected by the parallelization. Starting with a brief summary of the overall ingredients, the details on the parallel PCG method and the two-level additive Schwarz preconditioner follow subsequently.

7.2.1 Overview

1. **Distribution of the mesh:** The global regular fine mesh (see section 2.3.2) is distributed into a set of $\mathfrak{P}$ non-overlapping meshes on a set of (closed) sub-structures $\{\mathring{\Omega}_\mathfrak{p}, \mathfrak{p} = 1, \ldots, \mathfrak{P}\}$, $\bigcup_{\mathfrak{p}=1}^{\mathfrak{P}} \mathring{\Omega}_\mathfrak{p} = \bar{\Omega}$, each of which is assigned to one of the processes $\mathfrak{p} \in \{1, \ldots, \mathfrak{P}\}$. Furthermore, each process $\mathfrak{p} \in \{1, \ldots, \mathfrak{P}\}$ receives the set of fine tetrahedral elements in the overlapping subdomain $\Omega_\mathfrak{p}$, which is obtained by extending the substructure $\mathring{\Omega}_\mathfrak{p}$ by $\frac{\delta}{h} > 0$ voxel-layers of fine elements. We assume that the mesh can be distributed such that $\mathring{\Omega}_\mathfrak{p}$ does not cut coarse hexahedral elements. The hexahedra are formed by agglomerating fine tetrahedral elements $\tau \in \mathcal{T}_h(\mathring{\Omega}_\mathfrak{p})$ to coarse blocks of size $H \times H \times H$ as described in section 2.3.2. We denote the coarse mesh on process $\mathfrak{p}$ by $\mathcal{T}_H(\mathring{\Omega}_\mathfrak{p})$.

2. **Computing the basis functions:** The computation of the multiscale-FE basis functions with oscillatory boundary conditions requires the solution of local problems within each hexahedral element $T \in \mathcal{T}_H(\mathring{\Omega}_\mathfrak{p})$, $\mathfrak{p} \in \{1, \ldots, \mathfrak{P}\}$. For the computation of the boundary values on $\partial \mathcal{T}_H$ (see Algorithm 4.1), averaging the material coefficients on the adjacent fine elements requires material information on elements $\tau \in \mathcal{T}_h \supset \mathcal{T}_h(\mathring{\Omega}_\mathfrak{p})$ which touch ∂T with at least two of their vertices. If $\partial \mathcal{T}_H \cap \partial \mathring{\Omega}_\mathfrak{p} \neq \emptyset$, this also requires the material parameters on elements outside of $\mathring{\Omega}_\mathfrak{p}$. However, the information can be found locally on process $\mathfrak{p}$ since the overlapping subdomain $\Omega_\mathfrak{p}$ extends the substructure $\mathring{\Omega}_\mathfrak{p}$ by at least one layer of fine elements. Hence, no parallel communication is required for the determination of

the material coefficients within the fine elements adjacent to $\partial \overset{\square}{\Omega}_{\mathfrak{p}}$. The computation of the oscillatory multiscale finite element basis functions in (4.1) and (4.2) on $\mathcal{T}_H(\overset{\square}{\Omega}_{\mathfrak{p}})$ can be done fully in parallel.

3. **Parallel PCG:** The vectors and matrices used within the (P)CG algorithm have to be distributed on the non-overlapping mesh on $\overset{\square}{\Omega}_{\mathfrak{p}}$, $\mathfrak{p} \in \{1, \ldots, \mathfrak{P}\}$. Within each CG iteration, degrees of freedom at the interfaces need to be communicated between the parallel processes. A scalable implementation depends on an efficient parallelization of the (P)CG algorithm. Details on its parallelization are given in section 7.2.2.

4. **Two-Level preconditioning:** The two-level additive Schwarz preconditioner in (2.23) is applied once in each PCG iteration. It requires the exchange of information in the entire overlap between processes of neighboring subdomains and a global correction. Details on this procedure are stated in section 7.2.3.

Next, we address details concerning the implementation of the PCG algorithm in parallel. The CG algorithm and the two-level preconditioner are considered separately.

7.2.2 Parallel Preconditioned CG

The concepts of the parallelization of the PCG method which we present next can be found also in [28]. For $\mathfrak{p} \in \{1, \ldots, \mathfrak{P}\}$, let $R_{\overset{\square}{\Omega}_{\mathfrak{p}}}$ denote the matrix which restricts a (global) vector defined on $\mathcal{T}_h(\bar{\Omega})$ to a vector defined on $\mathcal{T}_h(\overset{\square}{\Omega}_{\mathfrak{p}})$, where $\bigcup_{\mathfrak{p}=1}^{\mathfrak{P}} \overset{\square}{\Omega}_{\mathfrak{p}} = \bar{\Omega}$ with $\overset{\square}{\Omega}_{\mathfrak{p}}$ being a closed subset of $\bar{\Omega}$ as described above. The parallelization of algorithms resulting from a finite element discretization with a non-overlapping distribution of the global mesh $\mathcal{T}_h$ typically involves two types of parallel vectors. Within the CG algorithm, we need to distinguish between *distributed* and *accumulated* vectors.

Definition 7.2.1 (Accumulated vector). *[28] Let $\mathbf{v}_{\mathfrak{p}}$ be the information of a global vector $\mathbf{v}$ which is stored on process $\mathfrak{p}$. Then the vector $\mathbf{v}$ is said to be (stored) accumulated, if*

$$\mathbf{v}_{\mathfrak{p}} = R_{\overset{\square}{\Omega}_{\mathfrak{p}}} \mathbf{v}$$

for any $\mathfrak{p} \in \{1, \ldots, \mathfrak{P}\}$. That is, each process contains the full information of the degrees of freedom on the interfaces of the non-overlapping substructures.

Definition 7.2.2 (Distributed vector). *[28] Let $\mathfrak{p} \in \{1, \ldots, \mathfrak{P}\}$ and let $\mathfrak{u}_\mathfrak{p}$ be the information of a global vector $\mathfrak{u}$ which is stored on process $\mathfrak{p}$. Then the vector $\mathfrak{u}$ is said to be (stored) distributed, if*

$$\mathfrak{u} = \sum_{\mathfrak{p}=1}^{\mathfrak{P}} R_{\square \atop \Omega_\mathfrak{p}}^{\top} \mathfrak{u}_\mathfrak{p}.$$

That is, each process contains only a part of the information of the degrees of freedom which lie on the interfaces of the non-overlapping substructures.

Distributed vectors are e.g. obtained by an elementwise assembling of a vector over a non-overlapping set of elements which are stored locally on each process. A typical example of such a distributed vector is the right-hand side $\mathbf{f}$ in equation (2.14), which is assembled in parallel over the fine elements $\tau \in \mathcal{T}_h(\overset{\square}{\Omega}_\mathfrak{p})$ according to equation (2.18). Any distributed vector can be easily transformed into an accumulated vector. The transformation requires communication, values of degrees of freedom at the interfaces need to be accumulated over processes which contain information of the particular degree of freedom. As it is important for the parallel implemention to distinguish between the two introduced types of vectors, we make the following convention. For the rest of this chapter, we denote a global vector by $\mathfrak{u}$ if it is stored accumulated on the parallel processes, while the vector is indicated by $\mathbf{u}$ when being stored in a distributed manner. The same differentiation can be applied to matrices. The global stiffness matrix A can be assembled in parallel without communication by assembling the local stiffness matrices $A_{\square \atop \Omega_\mathfrak{p}}$ according to section 2.2.4 over the non-overlapping set of elements $\tau \in \mathcal{T}_h(\overset{\square}{\Omega}_\mathfrak{p})$ which are stored locally on process $\mathfrak{p} \in \{1, \ldots, \mathfrak{P}\}$. Thus, the matrix A can be classified as a *distributed matrix* in the sense that $A = \sum_{\mathfrak{p}=1}^{\mathfrak{P}} R_{\square \atop \Omega_\mathfrak{p}}^{\top} A_{\square \atop \Omega_\mathfrak{p}} R_{\square \atop \Omega_\mathfrak{p}}$.

To keep the amount of communication in each iteration of the parallel PCG-algorithm (see Algorithm 7.1) as low as possible, the vectors $\mathbf{r}, \mathbf{v}, \mathbf{f}$ are stored in parallel as distributed vectors while the vectors $\mathfrak{u}, \mathfrak{p}, \mathfrak{z}$ are treated as accumulated vectors.

Now, we take a deeper look at the particular steps of the CG algorithm. Applying a scalar product between a distributed vector $\mathbf{r}$ and an accumulated vector $\mathfrak{z}$ yields [28]

$$\langle \mathbf{r}, \mathfrak{z} \rangle = \langle \sum_{\mathfrak{p}=1}^{\mathfrak{P}} R_{\square \atop \Omega_\mathfrak{p}}^{\top} \mathbf{r}_\mathfrak{p}, \mathfrak{z} \rangle = \sum_{\mathfrak{p}=1}^{\mathfrak{P}} \langle \mathbf{r}_\mathfrak{p}, R_{\square \atop \Omega_\mathfrak{p}} \mathfrak{z} \rangle = \sum_{\mathfrak{p}=1}^{\mathfrak{P}} \langle \mathbf{r}_\mathfrak{p}, \mathfrak{z}_\mathfrak{p} \rangle.$$

7. PARALLELIZATION: APPLICATION TO MULTI-PHASE ELASTIC COMPOSITES

Algorithm 7.1: The Preconditioned Conjugate Gradient Algorithm [28]

    Require: initial guess $\mathfrak{u}_0$, stopping tolerance $\epsilon > 0$, max. # of iterations m_{it}

    Return: (approximated) solution of $A\mathfrak{u} = \mathbf{f}$

   ① $\mathbf{r}_0 := \mathbf{f} - A\mathfrak{u}_0$

   ② $\mathfrak{z}_0 := M_{\mathrm{AS}}^{-1}\mathbf{r}_0$

   ③ $\mathfrak{p}_0 := \mathfrak{z}_0$

   ④ $\sigma_0 := \langle \mathbf{r}_0, \mathfrak{z}_0 \rangle$

   ⑤ $k := 0$

   while $k < m_{\mathrm{it}}$ *and* $\sqrt{\sigma_k/\sigma_0} > \epsilon$ **do**

      ⑥ $\mathbf{v}_k := A\mathfrak{p}_k$

      ⑦ $\alpha_k := \frac{\sigma_k}{\langle \mathfrak{p}_k, \mathbf{v}_k \rangle}$

      ⑧ $\mathfrak{u}_{k+1} := \mathfrak{u}_k + \alpha_k \mathfrak{p}_k$

      ⑨ $\mathbf{r}_{k+1} := \mathbf{r}_k - \alpha_k \mathbf{v}_k$

      ⑩ $\mathfrak{z}_{k+1} := M_{\mathrm{AS}}^{-1}\mathbf{r}_{k+1}$

      ⑪ $\sigma_{k+1} := \langle \mathbf{r}_{k+1}, \mathfrak{z}_{k+1} \rangle$

      ⑫ $\beta_k := \frac{\sigma_{k+1}}{\sigma_k}$

      ⑬ $\sigma_{k+1} := \sigma_k$

      ⑭ $\mathfrak{p}_{k+1} := \mathfrak{z}_{k+1} + \beta_k \mathfrak{p}_k$

      ⑮ $k := k + 1$

   end

That is, the scalar products can be calculated locally on $\overset{\square}{\Omega}_{\mathfrak{p}}$, $\mathfrak{p} \in \{1, \ldots, \mathfrak{P}\}$, and their sum needs to be accumulated and distributed to all processes. Thus, due to the combination of an accumulated with a distributed vector, the application of the scalar product in ④, ⑦ and ⑪ of Algorithm 7.1 requires only one `MPI_ALLREDUCE` (see [39, 47]) for a real value. The application of the preconditioner in the CG algorithm in ② and ⑩ takes as input a distributed vector and returns an accumulated vector and thus, requires communication between processes. The application of the two-level additive Schwarz preconditioner is presented in more detail below. All other operations including the `daxpy` (see e.g. [44]) operation in ⑧, ⑨ and ⑭ as well as the matrix-vector multiplication in ① and ⑥ do not require further communication. The latter

is true since the multiplication of a distributed matrix with an accumulated vector gives a distributed vector, which can be seen from (cf. also [28])

$$Au = \sum_{\mathfrak{p}=1}^{\mathfrak{P}} R_{\Omega_{\mathfrak{p}}}^{\top} A_{\Omega_{\mathfrak{p}}} R_{\Omega_{\mathfrak{p}}} \mathfrak{u} = \sum_{\mathfrak{p}=1}^{\mathfrak{P}} R_{\Omega_{\mathfrak{p}}}^{\top} A_{\Omega_{\mathfrak{p}}} \mathfrak{u}_{\mathfrak{p}} = \sum_{\mathfrak{p}=1}^{\mathfrak{P}} R_{\Omega_{\mathfrak{p}}}^{\top} \mathbf{r}_{\mathfrak{p}} = \mathbf{r},$$

where $\mathbf{r}_{\mathfrak{p}} := \overset{\square}{A}_{\mathfrak{p}} \mathfrak{u}_{\mathfrak{p}}$. Summarized, we conclude that the parallel PCG algorithm requires (i) two `MPI_ALLREDUCE` operations within each PCG-iteration and (ii) communication within the application of the preconditioner itself.

7.2.3 Two-Level Additive Schwarz Preconditioning in Parallel

Here we address the application of the classical two-level Schwarz preconditioner in its additive version, i.e. in the form presented in (2.23). The preconditioner combines local corrections on the overlapping subdomains and a coarse grid correction. In the following, we analyse their parallelization separately.

Parallel One-Level Additive Schwarz

We are given a set of overlapping subdomains $\{\Omega_{\mathfrak{p}}, \mathfrak{p} = 1, \ldots, \mathfrak{P}\}$ which are obtained by extending the non-overlapping distribution of the regular mesh $\mathcal{T}_h(\overset{\square}{\Omega}_{\mathfrak{p}})$ by a few layers of fine elements. We assume that $\Omega_{\mathfrak{p}} \backslash \partial\Omega$ is open. Let $R_{\Omega_{\mathfrak{p}}}$ be the restriction operator of a vector corresponding to degrees of freedom on the fine mesh from $\bar{\Omega} \backslash \Gamma_D$ to $\Omega_{\mathfrak{p}}$. The one-level additive Schwarz preconditioner on the subdomains reads $\sum_{\mathfrak{p}=1}^{\mathfrak{P}} R_{\Omega_{\mathfrak{p}}}^{\top} A_{\Omega_{\mathfrak{p}}}^{-1} R_{\Omega_{\mathfrak{p}}}$. Given the overlapping distribution of the mesh with $\Omega_{\mathfrak{p}} \backslash \partial\Omega$ open, the computation of the local submatrices $A_{\Omega_{\mathfrak{p}}}, i = 1, \ldots, \mathfrak{P}$ can be done in parallel since the global degrees of freedom outside of $\Omega_{\mathfrak{p}}$, which includes $\partial\Omega_{\mathfrak{p}}$, can be considered as homogeneous Dirichlet degrees of freedom and thus, they may not enter the linear system. Only the application of the one-level preconditioner to a vector requires communication. Before the local corrections, as a part of the additive Schwarz preconditioner in step ② and ⑩ of Algorithm 7.1, can be applied to a distributed vector $\mathbf{r}$, communication between neighboring subdomains is required. Due to the relation

$$\Omega_{\mathfrak{p}} = \left(\bigcup_{\mathfrak{q}=1}^{\mathfrak{P}} (\Omega_{\mathfrak{p}} \backslash \overset{\square}{\Omega}_{\mathfrak{p}}) \cap \overset{\square}{\Omega}_{\mathfrak{q}} \right) \cup \overset{\square}{\Omega}_{\mathfrak{p}},$$

7. PARALLELIZATION: APPLICATION TO MULTI-PHASE ELASTIC COMPOSITES

a parallel application of an distributed vector $\mathbf{r}$ to $R_{\Omega_{\mathfrak{p}}}$ can be written as

$$\mathfrak{r}_{\mathfrak{p}}^{\text{extd}} = \bigg(\underbrace{\sum_{\mathfrak{q}=1}^{\mathfrak{P}} R_{(\Omega_{\mathfrak{p}} \backslash \overset{\square}{\Omega}_{\mathfrak{p}}) \cap \overset{\square}{\Omega}_{\mathfrak{q}}}}_{\text{DOFs outside of } \overset{\square}{\Omega}_{\mathfrak{p}}} + \underbrace{\sum_{\mathfrak{p}=1}^{\mathfrak{P}} R_{\overset{\square}{\Omega}_{\mathfrak{p}}}}_{\text{DOFs on } \overset{\square}{\Omega}_{\mathfrak{p}}} \bigg) \mathbf{r}. \tag{7.1}$$

Here, $R_{(\Omega_{\mathfrak{p}} \backslash \overset{\square}{\Omega}_{\mathfrak{p}}) \cap \overset{\square}{\Omega}_{\mathfrak{q}}}$ denotes the restriction matrix of a vector defined on $\mathcal{T}_h(\bar{\Omega})$ to $\mathcal{T}_h((\Omega_{\mathfrak{p}} \backslash \overset{\square}{\Omega}_{\mathfrak{p}}) \cap \overset{\square}{\Omega}_{\mathfrak{q}})$. Applying the first term in equation (7.1) to $\mathbf{r}$ requires communication of degrees of freedom in the overlapping regions of $\Omega_{\mathfrak{p}}$ with the neighboring substructures $\overset{\square}{\Omega}_{\mathfrak{q}}$. The second term is obtained by a vector-accumulation of degrees of freedom at the interfaces of the non-overlapping distribution of the mesh. Since $A_{\Omega_{\mathfrak{p}}}$ can be assembled in parallel on process $\mathfrak{p}$, the action $\mathfrak{s}_{\mathfrak{p}}^{\text{extd}} := A_{\Omega_{\mathfrak{p}}}^{-1} \mathfrak{r}_{\mathfrak{p}}^{\text{extd}}$ can be easily applied and leaves flexibility in choosing the solver for the local problems. Finally, we obtain the accumulated vector $\mathfrak{r}^{1\text{L}}$ with $\mathfrak{r}_{\mathfrak{p}}^{1\text{L}} = R_{\overset{\square}{\Omega}_{\mathfrak{p}}} \mathfrak{r}^{1\text{L}}$ by

$$\mathfrak{r}_{\mathfrak{p}}^{1\text{L}} = R_{\overset{\square}{\Omega}_{\mathfrak{p}}} \mathfrak{r}^{1\text{L}} = R_{\overset{\square}{\Omega}_{\mathfrak{p}}} \sum_{\mathfrak{q}=1}^{\mathfrak{P}} R_{\Omega_{\mathfrak{q}}}^{\top} \mathfrak{s}_{\mathfrak{q}}^{\text{extd}} = \sum_{\mathfrak{q}=1}^{\mathfrak{P}} R_{\overset{\square}{\Omega}_{\mathfrak{p}}} R_{\Omega_{\mathfrak{q}}}^{\top} \mathfrak{s}_{\mathfrak{q}}^{\text{extd}}. \tag{7.2}$$

Thus, process $\mathfrak{p}$ collects and accumulates the values of degrees of freedom on $\overset{\square}{\Omega}_{\mathfrak{p}}$ from overlapping regions $\Omega_{\mathfrak{q}}, q \neq p$ of other processes. The resulting vector $\mathfrak{r}^{1\text{L}}$ is accumulated, as desired in step ② and ⑩ of Algorithm 7.1. Thus, applying the one-level additive Schwarz preconditioner requires communication twice to transfer information between the overlapping regions of neighboring subdomains.

Parallel Coarse Grid Correction

In the following we describe the parallel application of a coarse grid correction $\mathfrak{R}_H^{\top} A_H^{-1} \mathfrak{R}_H$ to a distributed vector $\mathbf{r}$. We define by $R_{\overset{\square}{\Omega}_{\mathfrak{p}}^H}$ the restriction matrix of a vector defined on $\mathcal{T}_H(\bar{\Omega})$ on the coarse triangulation to $\mathcal{T}_H(\overset{\square}{\Omega}_{\mathfrak{p}})$. Here we use the assumption that the distribution of the non-overlapping substructures $\{\overset{\square}{\Omega}_{\mathfrak{p}}, \mathfrak{p} = 1, \ldots, \mathfrak{P}\}$, is such that any coarse element $T \in \mathcal{T}_H(\bar{\Omega})$ is fully contained in exactly one substructure $\overset{\square}{\Omega}_{\mathfrak{q}}$ for some

$\mathfrak{q} \in 1 \ldots, \mathfrak{P}$. The coarse stiffness matrix A_H can be computed in parallel by (cf. [28])

$$
\begin{aligned}
A_H &= \mathfrak{R}_H A \mathfrak{R}_H^\top \\
&= \sum_{\mathfrak{p}=1}^{\mathfrak{P}} \mathfrak{R}_H (R_{\square_{\Omega_\mathfrak{p}}}^\top A_{\square_{\Omega_\mathfrak{p}}} R_{\square_{\Omega_\mathfrak{p}}}) \mathfrak{R}_H^\top \\
&= \sum_{\mathfrak{p}=1}^{\mathfrak{P}} R_{\square_{\Omega_\mathfrak{p}^H}}^\top R_{\square_{\Omega_\mathfrak{p}^H}} (\mathfrak{R}_H R_{\square_{\Omega_\mathfrak{p}}}^\top A_{\square_{\Omega_\mathfrak{p}}} R_{\square_{\Omega_\mathfrak{p}}} \mathfrak{R}_H^\top) R_{\square_{\Omega_\mathfrak{p}^H}}^\top R_{\square_{\Omega_\mathfrak{p}^H}} \\
&= \sum_{\mathfrak{p}=1}^{\mathfrak{P}} R_{\square_{\Omega_\mathfrak{p}^H}}^\top (R_{\square_{\Omega_\mathfrak{p}^H}} \mathfrak{R}_H R_{\square_{\Omega_\mathfrak{p}}}^\top) A_{\square_{\Omega_\mathfrak{p}}} (R_{\square_{\Omega_\mathfrak{p}^H}} \mathfrak{R}_H R_{\square_{\Omega_\mathfrak{p}}}^\top)^\top R_{\square_{\Omega_\mathfrak{p}^H}} \\
&=: \sum_{\mathfrak{p}=1}^{\mathfrak{P}} R_{\square_{\Omega_\mathfrak{p}^H}}^\top A_{\square_{\Omega_\mathfrak{p}^H}} R_{\square_{\Omega_\mathfrak{p}^H}}.
\end{aligned}
\tag{7.3}
$$

In the third equality we used that $R_{\square_{\Omega_\mathfrak{p}^H}}^\top R_{\square_{\Omega_\mathfrak{p}^H}} = I_{\square_{\Omega_\mathfrak{p}^H}}$ (identity on $\mathrm{range}(R_{\square_{\Omega_\mathfrak{p}^H}}^\top)$), which underlies some general restrictions. However, the restrictions do not apply to the regular mesh and its distribution considered here, we refer to [28] for more details. As mentioned before in section 7.2.1, the basis functions can be computed locally within the coarse hexahedral elements $T \in \mathcal{T}_H(\overset{\square}{\Omega}_\mathfrak{p})$, $\mathfrak{p} = 1, \ldots, \mathfrak{P}$. As a consequence, since $R_{\square_{\Omega_\mathfrak{p}^H}} \mathfrak{R}_H R_{\square_{\Omega_\mathfrak{p}}}^\top$ contains values of the basis functions restricted to $\overset{\square}{\Omega}_\mathfrak{p}$, computing the global stiffness matrix $A_{\square_{\Omega_\mathfrak{p}^H}}$ in the form of equation (7.3) can be done in parallel without communication. Furthermore, the application of the distributed vector $\mathbf{r}$ to the restricted matrix $\mathfrak{R}_H$ can be applied in parallel by $\mathbf{r}_\mathfrak{p}^\mathrm{H} = R_{\square_{\Omega_\mathfrak{p}^H}} \mathfrak{R}_H R_{\square_{\Omega_\mathfrak{p}}}^\top \mathbf{r}_\mathfrak{p}$. We accumulate the global stiffness matrix A_H and the coarse residual vector $\mathfrak{r}^H = \sum_{\mathfrak{p}=1}^{\mathfrak{P}} R_{\square_{\Omega_\mathfrak{p}^H}}^\top \mathbf{r}_\mathfrak{p}^\mathrm{H}$ on process $\mathfrak{p} = 1$ by collecting information of coarse degrees of freedom from all other processes $\mathfrak{p} = 2, \ldots, \mathfrak{P}$. The coarse solve $A_H^{-1} \mathfrak{s}^H = \mathfrak{r}^H$ is applied locally on process $\mathfrak{p} = 1$ using a direct sequential solver for the coarse linear system. The result $\mathfrak{s}^H$ is then distributed to the other processes and yields the vector $\mathfrak{s}_\mathfrak{p}^H = R_{\square_{\Omega_\mathfrak{p}^H}} \mathfrak{s}^H$ which is stored accumulated. Finally, from the coarse grid correction, we obtain the accumulated vector $\mathfrak{r}_\mathfrak{p}^{2\mathrm{L}} := R_{\square_{\Omega_\mathfrak{p}}} \mathfrak{R}_H^\top R_{\square_{\Omega_\mathfrak{p}^H}}^\top \mathfrak{s}_\mathfrak{p}^H$. The latter step does not require further communication. The result is added to $\mathfrak{r}_\mathfrak{p}^{1\mathrm{L}}$ which we obtain in (7.2) from the correction on local subdomains. Thus, the coarse grid correction needs communication in the way that (i) the data is collected on a single process, solved sequentially and (ii) the result is distributed to all processes.

7.3   Details on the Implementation

We divide the initial fine mesh into overlapping subdomains of cuboidal form. Each subdomain $\Omega_{\mathfrak{p}}$ consists of a substructure $\overset{\square}{\Omega}_{\mathfrak{p}}$ and their extension by $\frac{\delta}{h}$ layers of fine elements (layers in terms of the underlying voxel structure). Moreover, each substructure $\overset{\square}{\Omega}_{\mathfrak{p}}$ allows a further decomposition into hexahedral coarse elements $T \in \mathcal{T}_H(\overset{\square}{\Omega}_{\mathfrak{p}})$. Given that the number of coarse elements stored on process $\mathfrak{p}$ is large, we typically have $H \ll \text{diam}(\Omega_{\mathfrak{p}})$. To ensure that the size of the coarse elements $T \in \mathcal{T}_H(\overset{\square}{\Omega}_{\mathfrak{p}})$ is comparable to the diameter of the overlapping subdomains used in the additive Schwarz method, we further decompose $\Omega_{\mathfrak{p}}$ into a set of overlapping subdomains

$$\Omega_{\mathfrak{p}} = \bigcup_{\ell=1}^{S_{\mathfrak{p}}} \Omega_{\mathfrak{p}\ell},$$

where $\bar{\Omega}_{\mathfrak{p}\ell}$ is obtained by extending $T_\ell \in \mathcal{T}_H(\overset{\square}{\Omega}_{\mathfrak{p}})$ by $\frac{\delta}{h}$ layers of fine elements. The coarse mesh diameter H can be large enough such that the coarse linear system has a reasonably low number of degrees of freedom, allowing the application of a direct sequential solver. Specifically, we use the PARDISO Intel MKL library [85]. Advantages of introducing the additional level of subdomains are:

1. Memory requirements: For memory saving purposes, we do not store the full matrices $A_{\Omega_{\mathfrak{p}}}$ or $A_{\overset{\square}{\Omega}_{\mathfrak{p}}}$ on process $\mathfrak{p}$. Instead, we reassemble the local matrices $A_{\Omega_{\mathfrak{p}\ell}}$ or A_{T_ℓ} on $\Omega_{\mathfrak{p}\ell} \subset \Omega_{\mathfrak{p}}$ and $T_\ell \subset \overset{\square}{\Omega}_{\mathfrak{p}}$, respectively.

2. Scalability: keeping the ratio $\frac{H}{\delta}$ fixed, the overlap width δ can be reduced while decreasing the coarse mesh diameter H. A smaller overlap parameter δ increases the ratio between local computations and parallel communication for the benefit of a better parallel scalability.

3. Mesh parameters: As the condition number bound in 6.4.2 depends linearly on $1 + \frac{H}{\delta}$ and δ shall be small, choosing $H \ll \text{diam}(\overset{\square}{\Omega}_{\mathfrak{p}})$ allows a lower number of total PCG-iterations.

4. Flexibility: The substructuring allows a better control of the mesh parameters which may otherwise be predicted by the initial geometry and the number of processes used. Hence, the further decomposition introduces additional flexibility.

7.4 Numerical Results

For the parallel two-level preconditioner with oscillatory multiscale finite element coarse space, we perform numerical experiments testing the robustness of the method as well as the scalability of the implementation. Furthermore, we apply the developed method for a parallel simulation on a real composite microstructure.

7.4.1 Robustness w.r.t. Material Parameters

In the first set of numerical tests we observe the robustness of the oscillatory multiscale finite element coarse space w.r.t. variations in the material parameters. To confirm the argument that the two-level Schwarz preconditioner with the coarse space developed within this chapter should be preferred over the oscillatory multiscale-FE coarse space on a tetrahedral coarse mesh, we perform tests on the binary medium consisting of the matrix material with uniformly distributed inclusions in Figure 7.1. On that medium
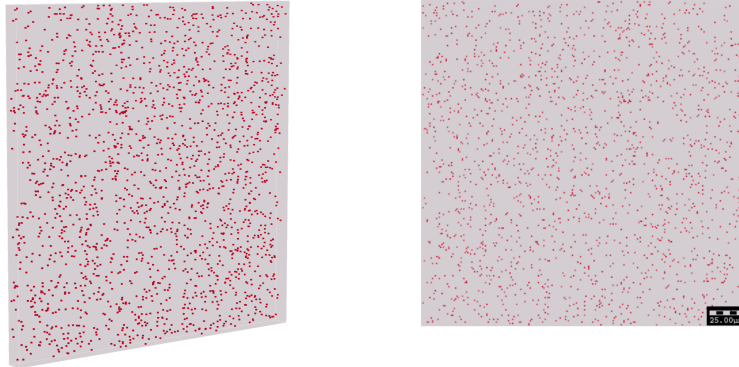

Figure 7.1: Binary composite discretized with $240 \times 240 \times 12$ voxels; matrix material (grey) and $1 \times 1 \times 1$ inclusions (red) uniformly distributed; 3D view (left) and 2D projection showing the position of the inclusions (right)

we performed tests before in section 6.6. Specifically, for the problem in Table 6.6, the vector-valued linear and the linear multiscale finite element coarse space are not robust for variations in the Young's modulus of the inclusions. Robustness is achieved only for the energy minimizing coarse space.

Here, we apply the multiscale finite element coarse space with oscillatory boundary conditions to the medium in Figure 7.1. Once we use coarse elements in the form of tetrahedra, once a hexahedral coarse mesh is used. A sparse direct solver of the

7. PARALLELIZATION: APPLICATION TO MULTI-PHASE ELASTIC COMPOSITES

	tetrahedral mesh $\mathcal{T}_H$			hexahedral mesh $\mathcal{T}_H$		
Δ_E	n_{it}	$\kappa(M_{AS}^{-1}A)$	$\gamma^{\mathrm{MsO}}(\lambda,\mu)$	n_{it}	$\kappa(M_{AS}^{-1}A)$	$\gamma^{\mathrm{MsO}}(\lambda,\mu)$
10^0	34	$4.0 \cdot 10^1$	$5.0 \cdot 10^0$	16	9.0	2.1
10^3	61	$2.9 \cdot 10^2$	$1.6 \cdot 10^1$	16	9.5	2.1
10^6	297	$6.9 \cdot 10^3$	$1.3 \cdot 10^4$	16	9.5	2.1
10^9	810	$4.0 \cdot 10^6$	$1.3 \cdot 10^7$	16	9.5	2.1

Table 7.1: Iteration numbers n_{it}, condition numbers $\kappa(M_{AS}^{-1}A)$ and coarse space robustness indicator $\gamma^{\mathrm{MsO}}(\lambda,\mu)$ for the medium in Figure 6.5; geometry: $1/h$ x $1/h$ x H/h, $h = 1/240$, $H = 12h$, $\delta = 2h$; oscillatory multiscale-FE coarse space with tetrahedral and hexahedral coarse mesh under variation of the contrast Δ_E

PARDISO Intel MKL library [85] is applied to compute the local subproblems and the coarse problem which arise within the algorithm. The material parameters for the matrix material are given by $\lambda_{\mathrm{mat}} = \mu_{\mathrm{mat}} = 1$. Table 7.1 shows iteration and condition numbers as well as the coarse space robustness indicator for different contrasts $\Delta_E = \lambda_{\mathrm{inc}}/\lambda_{\mathrm{mat}} = \mu_{\mathrm{inc}}/\mu_{\mathrm{mat}}$. Table 7.2 shows similar results under variations in the parameter λ_{inc}, while $\mu_{\mathrm{inc}} = 1$. The iteration numbers shown are to reduce the preconditioned initial residual by six orders of magnitude. The results in Table 7.1 and 7.2

	tetrahedral mesh $\mathcal{T}_H$			hexahedral mesh $\mathcal{T}_H$		
λ_{inc}	n_{it}	$\kappa(M_{AS}^{-1}A)$	$\gamma^{\mathrm{MsO}}(\lambda,\mu)$	n_{it}	$\kappa(M_{AS}^{-1}A)$	$\gamma^{\mathrm{MsO}}(\lambda,\mu)$
10^0	34	$4.0 \cdot 10^1$	$5.0 \cdot 10^0$	16	9.0	2.1
10^3	40	$5.5 \cdot 10^1$	$5.7 \cdot 10^0$	16	9.5	2.1
10^6	109	$4.2 \cdot 10^2$	$1.0 \cdot 10^3$	16	9.5	2.1
10^9	215	$1.9 \cdot 10^3$	$1.0 \cdot 10^6$	16	9.5	2.1

Table 7.2: Iteration numbers n_{it}, condition numbers $\kappa(M_{AS}^{-1}A)$ and coarse space robustness indicator $\gamma^{\mathrm{MsO}}(\lambda,\mu)$ for the medium in Figure 6.5; geometry: $1/h$ x $1/h$ x H/h, $h = 1/240$, $H = 12h$, $\delta = 2h$; oscillatory multiscale-FE coarse space with tetrahedral and hexahedral coarse mesh for different values of λ_{inc}

show that the robustness of the oscillatory multiscale-FE coarse space is clearly influenced by the choice of the coarse mesh. In the vicinity of sharp edges on the tetrahedral mesh, inclusions are positioned such that they touch three edges of a tetrahedron, but not the coarse node which touches these edges. This leads to an increase of the energy of the basis. We refer to Remark 6.5.2 for more details. The situation is different on the hexahedral mesh, robustness is achieved for any variation in the Lamé coefficients.

7.4.2 Robustness w.r.t. Mesh Parameters

In the following test we observe the sharpness of the bound in Theorem 6.4.2 w.r.t. the mesh parameter H and the overlap parameter δ. Table 7.3 shows the condition number for a simulation on a domain $\bar{\Omega} = [0,1]^3$ with fine mesh parameter $h = 1/128$. The coarse mesh parameter H and the overlap width δ take different values while $\lambda = 1$ and $\mu = 1$ are constant. A direct sparse solver (PARDISO [85]) is used to solve the coarse

$H \setminus \delta$	$1h$	$2h$	$4h$	$8h$	$16h$
$2h$	$8,91$	-	-	-	-
$4h$	$13,9$	$8,32$	-	-	-
$8h$	$23,5$	$12,3$	$8,35$	-	-
$16h$	$45,8$	$23,1$	$11,9$	$8,34$	-
$32h$	$74,8$	$37,7$	$19,2$	$8,8$	$8,25$

Table 7.3: Condition numbers $\kappa(M_{AS}^{-1}A)$ for different values of H and δ; geometry: $1/h$ x $1/h$ x $1/h$, $h = 1/128$; $\lambda = \mu = 1$

linear system in all cases except for $H = 2h$ and $H = 4h$, where the coarse system is solved using a fixed number of 20 V-cycles using SAMG (cf. [23]) as an approximate linear solver. For the corrections on the subdomains, 10 SAMG V-cycle iterations are applied. The condition numbers indicate their dependence on the ratio $1 + \frac{H}{\delta}$ as expected from the bound in Theorem 6.4.2.

7.4.3 Scaling Efficiency

In the next numerical test we examine the (strong) scalability of the implementation of the developed preconditioner. We explore the times for computations on the medium in Figure 7.2 for different numbers of processes. We calculate the speedup and the parallel efficiency using $\mathfrak{P}$ processes by $S_{\mathfrak{P}} := \frac{T_1}{T_{\mathfrak{P}}}$ and $E_{\mathfrak{P}} := \frac{S_{\mathfrak{P}}}{\mathfrak{P}}$, respectively. We consider the medium in Figure 7.2, discretized with $384 \times 72 \times 72$ voxels. The material parameters are chosen to $E_{\mathrm{mat}} = 10\mathrm{MPa}$, $E_{\mathrm{inc}} = 300\mathrm{MPa}$ and $\nu_{\mathrm{mat}} = \nu_{\mathrm{inc}} = 0.2$. Table 7.4 shows the run times for the parallel computations on a total of up to $\mathfrak{P} = 32$ processors. The non-overlapping distribution of the mesh onto the parallel processes is such that each process receives a block of size $384/\mathfrak{P} \times 72 \times 72$ voxels. The mesh diameter is chosen to be $H = 12h$ and the overlap width equals $\delta = 2h$. The tests are performed on a shared memory architecture with 8 quad-core AMD Opteron processors. Inexact local
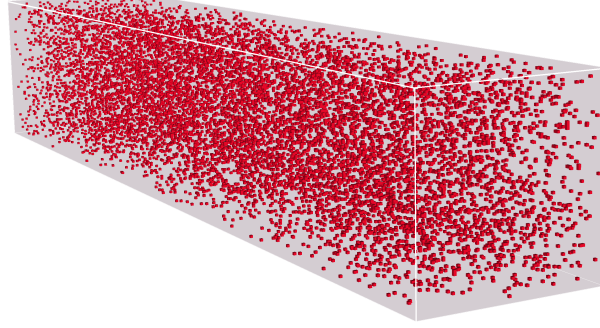
Figure 7.2: Voxel geometry discretized with $384{\times}72{\times}72$ voxels; inclusions (red) randomly distributed

$\mathfrak{P}$	setup precond.		solve	total		
	$T_\mathfrak{P}$	$E_\mathfrak{P}$	$T_\mathfrak{P}$	$T_\mathfrak{P}$	$S_\mathfrak{P}$	$E_\mathfrak{P}$
1	4870	1.00	18800	23670	1.00	1.00
2	2370	1.02	9090	11460	2.06	1.03
4	1190	1.02	4640	5830	4.06	1.01
8	610	1.00	2400	3010	7.86	0.98
16	299	1.01	1250	1549	15.3	0.96
32	153	0.99	720	873	27.1	0.85

Table 7.4: Scalability (time $T_\mathfrak{P}$ in seconds) of the parallel algorithm for the medium in Figure 7.2; $H = 12h$, $\delta = 2h$;

solves (10 V-cycles) are applied for the correction on local subdomains. A total of 14 iterations are performed to reduce the initial residual by four orders of magnitude. The basis functions are computed using SAMG as an approximate solver (initial residual reduced by 10^{-8}).

As summarized in section 7.2.1, the setup of the preconditioner or more precisely, the construction of the oscillatory multiscale-FE basis, requires no communication. This is in agreement with the results in Table 7.4, optimal scaling properties are obtained also for larger numbers of parallel processes. According to section 7.2.3, communication is required within each PCG iteration to exchange information of degrees of freedom locally between neighboring subdomains as well as globally when applying the scalar products or solving the coarse problem. We see from Table 7.4 that the implementation allows a good overall scalability, the large workload on any processor ensures that the local computation dominates the latency due to parallel communication.

7.4.4   Application to Multi-Phase Elastic Composites

Now, we apply the developed preconditioner to a elastic microstructure which is discretized with more than 200 Mio degrees of freedom. The composite consists of a steel matrix material which is enriched by nearly incompressible rubber inclusions. Figure 7.3 shows the material and the uniformly distributed inclusions which are identified by different colours, depending on their specific shape (ellipsoids or circles) and diameter ($6h - 24h$). The Young's modulus E as well as the Poisson ratio ν for steel and rubber
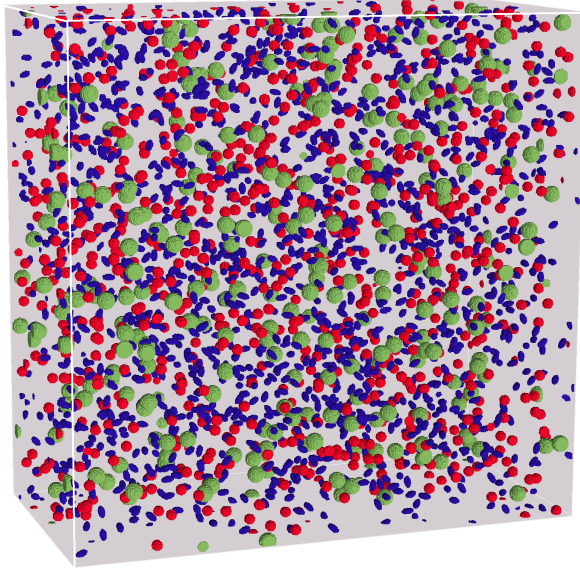

Figure 7.3: Composite microstructure: discretized with $512 \times 512 \times 256$ voxels (≈ 200 Mio DOFs); rubber inclusions of different shape and diameter distributed in steel matrix

are given in Table 7.5. The mesh parameters are $h = 1/512$, $H = 32h$, and the overlap width is $\delta = 4h$. The computation is performed on $\mathfrak{P} = 16$ processes.

The linear systems from the computation of the multiscale finite element basis functions are solved using SAMG (V-Cycle & PCG: reducing initial residual by 10^{-8}). Specifically, for each $T \in \mathcal{T}_H$, the discrete linear system according to the problem in (4.1) is assembled once, the right-hand sides are determind by the oscillatory boundary values in (4.2) and are computed using a direct sparse solver (PARDISO) for the discrete problems on the faces of T. We also apply SAMG as an approximate solver to the subdomain problems (10 V-cycles). As a result, we need 15 iterations to reduce the initial preconditioned residual by 4 orders of magnitude and require $t = 7.6 \cdot 10^4$ seconds

7. PARALLELIZATION: APPLICATION TO MULTI-PHASE ELASTIC COMPOSITES

Young's modulus		Poisson ratio		
E_{steel}	$=$ 210 GPa	ν_{steel}	$=$	0.3
E_{rubber}	$=$ 13.43 MPa	ν_{rubber}	$=$	0.4776

Table 7.5: Young's Modulus and Poisson ratio for the composite in Figure 7.3

for the overall computation. The condition number of the preconditioned linear system is estimated to $\kappa(M_{AS}^{-1}A) = 20.4$.

The total memory consumption and the savings by not storing the entire global stiffness matrix in parallel at a time can be analyzed as follows. Storing a global vector of length $2 \cdot 10^8$ requires approximately 1.6 GB (`double`) or 0.8 GB (`integer`) of memory on the 64bit infrastructure. Within the PCG algorithm, 6 global vectors are stored on the non-overlapping distribution of the fine mesh (see Algorithm 7.1). Storing the restriction operator $\mathfrak{R}_H$ in compact sparse row (CSR) format (cf. [89]) is equivalent to storing approximately 24 double and 24 integer vectors of length $2 \cdot 10^8$. Additionally, global vectors are required which allow to efficiently switch between the global and local numbering of degrees of freedom. Such a vector is e.g. required when applying the operator $R_{\Omega_{\mathfrak{p}\ell}}$ on process $\mathfrak{p}$, which restricts global degrees of freedom in $\Omega_{\mathfrak{p}}$ to local degrees of freedom in $\Omega_{\mathfrak{p}\ell}$. Its entries are initially set to a negative number. When a local computation is performed, say on $\Omega_{\mathfrak{p}\ell}$, the entries in the global index which correspond to degrees of freedom in $\Omega_{\mathfrak{p}\ell}$ are replaced by the number of their degree of freedom in the local numbering within $\mathcal{V}^h(\Omega_{\mathfrak{p}\ell})$. After the computation, the modified global entries are reset to the negative number and the vector can be used in an equal manner for a computation on the other subdomains.

Each process initially receives 21 Mio tetrahedral fine elements of the substructure of $32 \times 512 \times 256$ voxels. Additionally, the fine elements $\tau \in \mathcal{T}_h$ in the four adjacent voxel-layers are stored locally. Hence, 335 Mio elements from the non-overlapping distribution of the mesh and additionally 78 Mio elements in the overlaps are required. To each element, the global index-number of the four vertices are stored which gives a total of $1.6 \cdot 10^9$ integer values. Also, about 87 Mio fine mesh nodes are stored on the parallel processes, each of which contains the coordinates in the three spatial dimensions ($2.6 \cdot 10^8$ double values).

Alltogether, this leads to a total consumption of approximately 80 GB of memory. Slightly more memory is required e.g. to perform the local computations, for storing the material information of fine elements or for storing the table *AE_element* (see section 2.3.2) as a boolean matrix (cf. [102]).

To estimate the memory savings by not storing the global stiffness matrix, we deduce the sparsity pattern of the matrix A from the structure of the fine mesh in section 2.3.2. Each node $x^j \in \Sigma_h$ is connected over an edge to either 6 or 26 (alternating) other nodes of $\mathcal{T}_h$. In average, with $d = 3$ degrees of freedom stored at each node, we obtain an average number of 51 non-zero entries per row in the sparse stiffness matrix. Hence, storing the matrix A in CSR-format has an approximate memory consumption which is equivalent to storing 51 double and 51 integer vectors of length $2 \cdot 10^8$ and requires more than 122 GB.

Given the 80+ GB memory consumption from before, we save more than 50% by not storing the entire stiffness matrix A on the parallel processes. Assembling only the upper triangular part of the symmetric matrix might slightly reduce the total gain, however, additional memory would be required also for the matrices $A_{\Omega_{\mathfrak{p}}}$, $\Omega_{\mathfrak{p}} \supset \overset{\square}{\Omega}_{\mathfrak{p}}$, $\mathfrak{p} = 1 \ldots, \mathfrak{P}$, or possibly for their approximate inverses.

7.5   Conclusions

We present a distributed memory (MPI) parallel implementation of the PCG-accelerated two-level additive Schwarz method. The coarse space is constructed on a hexahedral coarse mesh by the multiscale finite element method with oscillatory boundary conditions. In the implementation, the only parallel tool we use is the Open MPI message passing library [84]. We give details of the parallel algorithm and provide adaptions of the sequential algorithm. The particular steps which require communication are discused in detail.

We perform numerical experiments on heterogeneous media testing the scaling efficiency of the algorithm and the robustness of the presented method. For the latter, the results clearly demonstrate that the construction of the oscillatory multiscale finite element basis on a hexahedral rather than a tetrahedral coarse mesh is beneficial for the robustness of the overall method. The strong scalability of the algorithm is tested on a microstructure using up to 32 parallel processes. It shows very good scaling properties,

not only for the construction of the multiscale finite element basis, but also in the PCG method itself. Furthermore, computations on a heterogeneous microstructure are presented leading to a problem with more than 200 Mio degrees of freedom.

Given the good scalability and robustness results, we shortly discuss possible extensions in the implementation:

- In order to obtain the parallel mesh distribution as discussed in section 7.2.1, the material numbers of the entire voxel structure are initially accessible to any process. Then, process $\mathfrak{p} \in \{1, \ldots, \mathfrak{P}\}$ constructs the mesh exclusively on the substructure $\overset{\square}{\Omega}_{\mathfrak{p}}$, extended by $\frac{\delta}{h}$ layers of fine elements. Also, the parallel implementation allows a decomposition of the global geometry only in the direction of one spatial coordinate. Other approaches are conceivable, such as a purely distributed mesh generation (see e.g. [2]) or by pre-processing the microstructure such that each process initially receives only a subset of the overall domain.

- For the coarse grid correction, a sequential solver is applied to solve the coarse linear system on a single process. This requires global communication when collecting the coarse residual vector and distributing the solution vector to the other processes. The global communication can be replaced by local communications when a parallel sparse direct solver is used (see e.g. [48]).

- Saving memory by not storing the full stiffness matrix A goes to the expense of the efficiency of the overall algorithm. Local matrices need to be reassembled twice per PCG iteration, once for the application of a matrix-vector multiplication, once to apply the correction on a local subdomain. Fast assembling processes need to be developed by using the regular structure of the underlying mesh to allow a faster application and thus, to improve the overall efficiency. The regular structure may also allow the application of a sparse solver which is adapted to the grid in an optimal manner. Using the structure of the grid to apply a direct solver for the corrections on local subdomains may be beneficial for the stability and the efficiency of the method.

8

Discussion

In this thesis, we study two-level additive Schwarz domain decomposition preconditioners for finite element discretizations of multiscale problems in linear elasticity. Of main interest in our analysis is the application to highly heterogeneous composite materials in three spatial dimensions. The underlying composites typically combine multiscale features, having highly oscillating material coefficients on very small scales which make the discrete systems hard to solve.

Efficient iterative solution methods perform a good portion of the total computation on grid levels coarser than the fine discretization. Provided that the coefficient variations can be resolved by the coarse(st) grid, such methods allow to robustly solve the discrete linear systems with iteration numbers independent of the PDE coefficients. However, as coefficient variations in the multiscale problems considered here appear even on very small scales, they cannot be resolved by coarser grids.

In the framework of this thesis, multiscale coarsening strategies are developed which guarantee optimal robustness properties for large classes of heterogeneous problems, even if variations in the PDE coefficients of the elastic tensor cannot be resolved by a coarse mesh. Therefore, we extend the linear and oscillatory multiscale finite element method as formulated by Hou and Wu [53] to the system of linear elasticity. We apply the coarse spaces in the context of two-level overlapping domain decomposition preconditioners. For isolated inclusions of high contrast in the interior of coarse mesh elements, the condition number of the additive Schwarz preconditioned system does not depend on variations in Young's modulus and the Poisson ratio when the linear multiscale finite element coarse space is applied. By using oscillatory boundary condi-

tions for the multiscale finite element basis, the method is robust also in cases where stiff inclusions cross or touch coarse element boundaries. Furthermore, energy minimizing coarse spaces are developed and their robustness properties are studied on various multiscale test problems.

This is followed by a comprehensive analysis of two-level additive Schwarz domain decomposition preconditioners for the multiscale elasticity problems. For scalar elliptic PDEs of multiscale character, such an analysis is provided by Graham, Lechner and Scheichl in [45]. The work which we present here includes an extension of the work in [45] from scalar elliptic PDEs to the PDE system of linear elasticity. We present coefficient-explicit bounds for the condition number of the two-level additive Schwarz preconditioned linear system. These estimates give sharper bounds than existing ones (see section 1.2) and do not require that the coarse mesh resolves the material coefficients. The bounds show a dependence of the condition number on the energy of the coarse basis functions, the coefficient distribution, the coarse mesh and the overlap parameters. Furthermore, the developed estimates provide a concept for the construction of coarse spaces which can lead to preconditioners which are robust w.r.t. discontinuities in the Young's modulus and the Poisson ratio of the underlying composite.

The theoretical analysis included allows the detailed examination of the coarse space robustness properties of the developed multiscale coarse spaces. Numerical tests on binary media using the multiscale finite element and energy minimizing coarse spaces confirm the theoretical findings. Furthermore, we present a parallel and memory saving implementation of the developed methods and perform calculations on a 3D microstructure which is discretized with more than 200 Mio degrees of freedom.

The methods developed within the thesis may also be used in other interesting applications including computations on stochastic geometries as well as for solving nonlinear (e.g. hyperelastic, plastic) or time dependent (viscoelastic) problems.

Bibliography

[1] R. A. ADAMS AND J. F. FOURNIER, *Sobolev Spaces*, Academic Press, Inc, 2 ed., 2003.

[2] H. ANDRÄ, O. GLUCHSHENKO, E. IVANOV, AND A. KUDRYAVTSEV, *Automatic parallel generation of tetrahedral grids by using a domain decomposition approach*, Comp. Math Math Phys, 48 (2008), pp. 1367–1375.

[3] O. AXELSSON AND V. A. BARKER, *Finite element solution of boundary value problems: Theory and computation*, Academic Press, Inc, 1984.

[4] I. BABUŠKA, G. CALOZ, AND J. E. OSBORN, *Special finite element methods for a class of second order elliptic problems with rough coefficients*, SIAM J. Numer. Anal., 31 (1994), pp. 945–981.

[5] I. BABUŠKA, U. BANERJEE, AND J. E. OSBORN, *Survey of meshless and generalized finite element methods: A unified approach*, Acta Numerica, 12 (2003), pp. 1–125.

[6] A. H. BAKER, T. KOLEV, AND U. M. YANG, *Improving algebraic multigrid interpolation operators for linear elasticity problems*, Numer. Linear Algebr., 17 (2010), pp. 495–517.

[7] G. A. BLISS, *Lectures on the calculus of variations*, University of Chicago Press, 1963.

[8] J. BONET AND R. WOOD, *Nonlinear continuum mechanics for the finite element analysis*, Cambridge University Press, 2 ed., 1997.

BIBLIOGRAPHY

[9] D. BRAESS, *Finite elements: Theory, fast solvers and applications in solid mechanics*, Cambridge University Press, 3 ed., 2007.

[10] A. BRANDT, *Algebraic multigrid theory: The symmetric case*, Appl. Math. Comput., 19 (1986), pp. 23–56.

[11] A. BRANDT, S. F. MCCORMICK, AND J. W. RUGE, *Algebraic multigrid (AMG) for automatic multigrid solution with application to geodetic computations*, Institute for Computational Studies, Colorado State University, 1982.

[12] A. BRANDT, S. F. MCCORMICK, AND J. W. RUGE, *Algebraic multigrid (AMG) for sparse matrix equations*, in Sparsity and its Applications, Cambridge University Press, 1984, pp. 257–284.

[13] M. BREZINA, A. J. CLEARY, R. D. FALGOUT, V. E. HENSON, J. E. JONES, T. A. MANTEUFFEL, S. F. MCCORMICK, AND J. W. RUGE, *Algebraic multigrid based on element interpolation (AMGe)*, SIAM J. Sci. Comput., 22 (2000), pp. 1570–1592.

[14] F. BREZZI AND M. FORTIN, *Mixed and hybrid finite element methods*, Springer, 1991.

[15] M. BUCK, O. ILIEV, AND H. ANDRÄ, *Domain decomposition preconditioners for multiscale problems in linear elasticity.* submitted.

[16] M. BUCK, O. ILIEV, AND H. ANDRÄ, *Multiscale coarsening for linear elasticity by energy minimization*, in Numerical Solution of Partial Differential Equations: Theory, Algorithms and their Applications, Springer Proceedings in Mathematics & Statistics, 45 (2013), pp. 21–44.

[17] M. BUCK, O. ILIEV, AND H. ANDRÄ, *Multiscale finite elements for linear elasticity: Oscillatory boundary conditions.* Submitted to Proceedings of the 21st Intern. Confer. on Domain Decomposition Methods, July 2012, Rennes, France.

[18] M. BUCK, O. ILIEV, AND H. ANDRÄ, *Multiscale finite element coarse spaces for the analysis of linear elastic composites*, Tech. Rep. 2012-212, Fraunhofer ITWM, 2012.

[19] M. Buck, O. Iliev, and H. Andrä, *Multiscale finite element coarse spaces for the application to linear elasticity*, Cent. Eur. J. Math., 11 (2013), pp. 680–701.

[20] X. C. Cai and M. Sarkis, *A restricted additive schwarz preconditioner for general sparse linear systems*, SIAM J. Sci. Comput., 21 (1999), pp. 239–247.

[21] C. C. Chu, I. G. Graham, and T. Y. Hou, *A new multiscale finite element method for high-contrast elliptic interface problems*, Math. Comput., 79 (2010), pp. 1915–1955.

[22] P. G. Ciarlet, *Mathematical elasticity, II. Theory of plates*, vol. 27 of Studies in Mathematics and its Applications, Elsevier, Amsterdam, 1997.

[23] T. Clees, *AMG strategies for PDE systems with applications in industrial semiconductor simulation*, PhD thesis, University of Cologne, Faculty of Mathematics, 2005.

[24] P. Clément, *Approximation by finite element functions using local regularization*, RAIRO Anal. Numer., R-2 (1975), pp. 77–84.

[25] C. M. Dafermos, *Some remarks on Korn's inequality*, Angew. Math. Phys., 19 (1968), pp. 913–920.

[26] C. Dohrmann, A. Klawonn, and O. Widlund, *A family of energy minimizing coarse spaces for overlapping Schwarz preconditioners*, in Domain Decomposition Methods in Science and Engineering XVII, Springer Lect. Notes Comp. Sci., vol. 60, 2008, pp. 247–254.

[27] C. R. Dohrmann and O. B. Widlund, *Hybrid domain decomposition algorithms for compressible and almost incompressible elasticity*, Int. J. Numer. Meth. Eng., 82 (2010), pp. 157–183.

[28] C. C. Douglas, G. Haase, and U. Langer, *A tutorial on elliptic PDE Solvers and their parallelization*, Series Software, Environments, and Tools, SIAM, 2003.

[29] M. Dryja, M. V. Sarkis, and O. B. Widlund, *Multilevel schwarz methods for elliptic problems with discontinuous coefficients in three dimensions*, Numer. Math., 72 (1996), pp. 313–348.

[30] R. G. Duran and M. A. Muschietti, *The Korn inequality for Jones domains*, Electron. J. Diff. Eqns., 127 (2004), pp. 1–10.

[31] L. J. Durlofsky, Y. Efendiev, and V. Ginting, *An adaptive local-global multiscale finite volume element method for two-phase flow simulations*, Adv. Water. Resour., 30 (2007), pp. 576–588.

[32] Y. Efendiev, J. Galvis, R. Lazarov, and J. Willems, *Robust domain decomposition preconditioners for abstract symmetric positive definite bilinear forms*, Math. Model. Numer. Anal., 46 (2012), pp. 1175–1199.

[33] Y. Efendiev, J. Galvis, and P. S. Vassilevski, *Spectral element agglomerate algebraic multigrid methods for elliptic problems with high-contrast coefficients*, in Domain Decomposition Methods in Science and Engineering XIX, 2011, pp. 407–414.

[34] Y. Efendiev and T. Y. Hou, *Multiscale finite element methods, theory and applications*, Surveys and Tutorials in the Applied Mathematical Sciences, Springer, 4 ed., 2009.

[35] Y. Efendiev, J.Galvis, and T. Hou, *Generalized multiscale finite element methods (GMsFEM)*. submitted.

[36] A. Ern and J. L. Guermond, *Theory and practice of finite elements*, vol. 159 of Applied Mathematical Sciences, 2004.

[37] R. S. Falk, *Non-conforming finite element methods for the equations of linear elasticity*, Math. Comp., 57 (1991), pp. 529–550.

[38] B. Fiedler, F. Gojny, M. Wichmann, M. Nolte, and K. Schulte, *Fundamental aspects of nano-reinforced composites*, Compos. Sci. Technol, 66 (2006), pp. 3115–3125.

[39] M. P. I. Forum, *MPI: A Message-Passing Interface Standard*, High Performance Computing Center Stuttgart, 2.2 ed., 2009.

[40] K. O. Friedrichs, *On the boundary value problems of the theory of elasticity and Korn's inequality*, Ann. of Math., 48 (1947), pp. 441–471.

[41] J. GALVIS AND Y. EFENDIEV, *Domain decomposition preconditioners for multi-scale flows in high-contrast media*, Multiscale Model. Simul., 8 (2010), pp. 1461–1483.

[42] J. GALVIS AND Y. EFENDIEV, *Domain decomposition preconditioners for mul-tiscale flows in high-contrast media: reduced dimension coarse spaces*, Multiscale Model. Simul., 8 (2010), pp. 1621–1644.

[43] GEODICT, *http://www.geodict.com*.

[44] G. H. GOLUB AND C. V. LOAN, *Matrix Computations*, The Johns Hopkins University Press, 3 ed., 1996.

[45] I. G. GRAHAM, P. O. LECHNER, AND R. SCHEICHL, *Domain decomposition for multiscale PDEs*, Numer. Math., 106 (2007), pp. 589–626.

[46] I. G. GRAHAM AND R. SCHEICHL, *Robust domain decomposition algorithms for multiscale PDEs*, Numer. Methods Partial Differ. Equ., 23 (2007), pp. 859–878.

[47] W. GROPP, E. LUSK, AND R. THAKUR, *Using MPI-2: advanced features of the message-passing interface*, Scientific and Engineering Computation, 2 ed., 1999.

[48] W. D. GROPP AND D. E. KEYES, *Domain decomposition methods in computa-tional fluid dynamics*, International journal for numerical methods in fluids, 14 (1992), pp. 147–165.

[49] W. HACKBUSCH, *Multi-Grid Methods and Applications*, Springer Series in Com-putational Mathematics, 2 ed., 2003.

[50] I. HIAVAČEK AND J. NEČAS, *On inequalities of Korn's type, II: Applications to linear elasticity*, Arch. Rational Mech. Anal., 36 (1970), pp. 305–334.

[51] C. O. HORGAN, *Korn's inequalities and their applications in continuum mechan-ics*, SIAM Rev., 37 (1995), pp. 491–511.

[52] C. O. HORGAN AND L. E. PAYNE, *On inequalities of Korn, Friedrichs and Babuka-Aziz*, Arch. Rational Mech. Anal., 82 (1983), pp. 165–179.

[53] T. Y. Hou and X. H. Wu, *A multiscale finite element method for elliptic problems in composite materials and porous media*, J. Comput. Phys., 134 (1997), pp. 169–189.

[54] T. Y. Hou and X. H. Wu, *A multiscale finite element method for PDEs with oscillatory coefficients*, Note Num. Fl., 70 (1999), pp. 58–69.

[55] T. Y. Hou, X. H. Wu, and Z. Cai, *Convergence of a multiscale finite element method for elliptic problems with rapidly oscillating coefficients*, Math. Comp., 68 (1999), pp. 913–943.

[56] T. Hughes, G. Feijo, L. Mazzei, and J. B. Quincy, *The variational multiscale method a paradigm for computational mechanics*, Comput. Meth. Appl. Mech. Engrg., 166 (1998), pp. 3–24.

[57] T. J. R. Hughes, *The finite element method: Linear static and dynamic finite element analysis*, Prentice-Hall, Inc., 1987.

[58] O. Iliev, R. Lazarov, and J. Willems, *Variational multiscale finite element method for flows in highly porous media*, Multiscale Model. Simul., 9 (2011), pp. 1350–1372.

[59] A. Janka, *Algebraic domain decomposition solver for linear elasticity*, Appl. Math-Czech, 44 (1999), pp. 435–458.

[60] B. Ji and H. Gao, *Mechanical properties of nanostructure of biological materials*, J. Mech. Phys. Solids, 52 (2004), pp. 1963–1990.

[61] J. E. Jones and P. S. Vassilevski, *AMGe based on element agglomeration*, SIAM J. Sci. Comput., 23 (2001), pp. 109–133.

[62] P. W. Jones, *Quasiconformal mappings and extendability of functions in Sobolev spaces*, Acta Math., 147 (1981), pp. 71–88.

[63] E. Karer, *Subspace correction methods for linear elasticity*, PhD thesis, University of Linz, 2011.

[64] E. KARER AND J. K. KRAUS, *Algebraic multigrid for finite element elasticity equations: Determination of nodal dependence via edge matrices and two-level convergence*, Int. J. Numer. Meth. Engng., 83 (2010), pp. 642–670.

[65] A. KLAWONN AND O. A. RHEINBACH, *Robust FETI-DP methods for heterogeneous three dimensional elasticity problems*, Comput. Method. Appl. M., 196 (2007), pp. 1400–1414.

[66] A. KLAWONN AND O. A. RHEINBACH, *A parallel implementation of dual-primal FETI methods for three-dimensional linear elasticity using a transformation of basis*, SIAM J. Sci. Comput., 28 (2009), pp. 1886–1906.

[67] A. KLAWONN AND O. B. WIDLUND, *Dual-Primal FETI methods for linear elasticity*, Comm. Pure Appl. Math., 59 (2006), pp. 1523–1572.

[68] T. KOLEV AND S. MARGENOV, *AMLI preconditioning of pure displacement non-conforming elasticity FEM systems*, in Second International Conference on Numerical Analysis and Its Applications, Numerical Analysis and its Applications, 2001, pp. 339–367.

[69] T. V. KOLEV AND P. S. VASSILEVSKI, *AMG by element agglomeration and constrained energy minimization interpolation*, Numer. Linear Algebr. Appl., 13 (2006), pp. 771–788.

[70] V. A. KONDRATIEV AND O. A. OLEINIK, *On Korn's inequalities*, C. R. Acad. Sci. Paris, 308 (1989), pp. 483–487.

[71] V. A. KONDRATIEV AND O. A. OLEINIK, *On the dependence of the constant in Korn's inequality on parameters characterizing the geometry of the region*, Russ. Math. Surv., 44 (1989), pp. 187–195.

[72] A. KORN, *Die Eigenschwingungen eines elastischen Körpers mit ruhender Oberfläche*, Akad der Wissensch., Munich, Math. -phys. Kl., 36 (1906), pp. 351–401.

[73] A. KORN, *Über einige Ungleichungen, welche in der Theorie der elastischen und elektrischen Schwingungen eine Rolle spielen*, (1909), pp. 706–724.

[74] J. K. KRAUS, *Algebraic multigrid based on computational molecules, II: Linear elasticity problems*, SIAM J. Sci. Comput., 30 (2008), pp. 505–524.

[75] J. K. KRAUS AND S. MARGENOV, *Robust algebraic multilevel methods and algorithms*, De Gruyter, Berlin, 2009.

[76] J. K. KRAUS AND J. SCHICHO, *Algebraic multigrid based on computational molecules I: Scalar elliptic problems*, Computing, 77 (2006), pp. 57–75.

[77] T. LEVI-CIVITA, *The Absolute Differential Calculus*, Dover Publications, 1977.

[78] J. MANDEL, M. BREZINA, AND P. VANĚK, *Energy optimization of algebraic multigrid bases*, Computing, 62 (1999), pp. 205–228.

[79] T. MATHEW, *Domain decomposition methods for the numerical solution of partial differential equations*, vol. 61, Springer, 2008.

[80] S. F. MCCORMIC, *Multigrid Methods*, Frontiers in Applied Mathematics, 3 ed., 1987.

[81] R. MILLWARD, *A new adaptive multiscale finite element method with applications to high contrast interface problems*, PhD thesis, University of Bath, 2011.

[82] A. N. NORRIS, *Euler-rodrigues and Cayley formulas for rotation of elasticity tensors*, Math. Mech. Solids, 13 (2008), pp. 465–498.

[83] L. N. OLSON, J. B. SCHRODER, AND R. S. TUMINARO, *A general interpolation strategy for algebraic multigrid using energy minimization*, SIAM J. Sci. Comput., 33 (2011), pp. 966–991.

[84] OPEN MPI MESSAGE PASSING LIBRARY, *http://www.open-mpi.org*.

[85] PARDISO SOLVER PROJECT, *http://www.pardiso-project.org*.

[86] C. PECHSTEIN AND R. SCHEICHL, *Analysis of FETI methods for multiscale PDEs*, Numer. Math., 111 (2008), pp. 293–333.

[87] C. PECHSTEIN AND R. SCHEICHL, *Analysis of FETI methods for multiscale PDEs, part II: interface variation*, Numer. Math., 118 (2011), pp. 485–529.

[88] W. PRESS, S. TEUKOLSKY, W. VETTERLING, AND B. FLANNERY, *Numerical recipes: The art of scientific computing*, Cambridge University Press, 3 ed., 1986.

[89] Y. SAAD, *Iterative methods for sparse linear systems*, SIAM, 2 ed., 2003.

[90] M. SARKIS, *Partition of unity coarse spaces: Enhanced versions, discontinuous coefficients and applications to elasticity*, in Domain Decomposition Methods in Science and Engineering XIV, Springer Lect. Notes Comp. Sci., 2003, pp. 149–158.

[91] R. SCHEICHL, P. S. VASSILEVSKI, AND L. T. ZIKATANOV, *Weak approximation properties of elliptic projections with functional constraints*, Multiscale Model. Simul., 9 (2011), pp. 1677–1699.

[92] R. SCHEICHL, P. S. VASSILEVSKI, AND L. T. ZIKATANOV, *Multilevel methods for elliptic problems with highly varying coefficients on nonaligned coarse grids*, SIAM J. Numer. Anal., 50 (2012), pp. 1675–1694.

[93] V. SCHULZ, H. ANDRÄ, AND K. SCHMIDT, *Robuste Netzgenerierung zur Mikro-FE-Analyse mikrostrukturierter Materialien*, in NAFEMS Magazin, vol. 2, 2007, pp. 28–30.

[94] B. F. SMITH, *Domain decomposition algorithms for the partial differential equations of linear elasticity*, PhD thesis, Courant Institute of Mathematical Sciences, New York University, 1990.

[95] N. SPILLANE, V. DOLEAN, P. HAURET, F. NATAF, C. PECHSTEIN, AND R. SCHEICHL, *Abstract robust coarse spaces for systems of PDEs via generalized eigenproblems in the overlaps*, Tech. Rep. 2011-07, University of Linz, Institute of Computational Mathematics, 2011.

[96] E. T. THOSTENSON, Z. REN, AND T. W. CHOU, *Advances in the science and technology of carbon nanotubes and their composites: a review*, Compos. Sci. Technol., 61 (2001), pp. 1899–1912.

[97] A. TOSELLI AND O. B. WIDLUND, *Domain decomposition methods, algorithms and theory*, Springer, 2005.

[98] J. Van lent, R. Scheichl, and I. G. Graham, *Energy-minimizing coarse spaces for two-level Schwarz methods for multiscale PDEs*, Numer. Linear Algebra Appl., 16 (2009), pp. 775–799.

[99] P. Vaněk, *Acceleration of convergence of a two-level algorithm by smoothing transfer operator*, Appl. of Math., 37 (1992), pp. 265–274.

[100] P. Vaněk, M. Brezina, and R. Tezaur, *Fast multigrid solver*, Appl. Math., 40 (1995), pp. 1–20.

[101] P. Vaněk, M. Brezina, and R. Tezaur, *Two-grid method for linear elasticity on unstructured meshes*, SIAM J. Sci. Comput., 21 (1999), pp. 900–923.

[102] P. S. Vassilevski, *Multilevel block factorization preconditioners: Matrix-based anal ysis and algorithms for solving finite element equations*, Springer, New York, 2008.

[103] P. S. Vassilevski, *General constrained energy minimizing interpolation mappings for AMG*, SIAM J. Sci. Comput., 32 (2010).

[104] P. S. Vassilevski and L. Zikatanov, *Multiple vector preserving interpolation mappings in algebraic multigrid*, SIAM J. Matrix Anal. A., 27 (2006), pp. 1040–1055.

[105] W. Wan, T. F. Chan, and B. Smith, *An energy-minimizing interpolation for robust multigrid methods*, SIAM J. Sci. Comput., 21 (2000), pp. 1632–1649.

[106] E. Weinan and B. Engquist, *The heterogeneous multi-scale methods*, Comm. Math. Sci., 1 (2003), pp. 87–133.

[107] E. Weinan, B. Engquist, X. Li, W. Ren, and E. Vanden-Eijnden, *Heterogeneous multiscale methods: A review*, Communications in Computational Physics, 2 (2007), pp. 367–450.

[108] J. Willems, *Robust multilevel methods for general symmetric positive definite operators*, Tech. Rep. 2012-06, RICAM Institute for Computational and Applied Mathematics, 2012.

[109] J. WILLEMS, *Spectral coarse spaces in robust two-level methods*, Tech. Rep. 2012-20, RICAM Institute for Computational and Applied Mathematics, 2013.

[110] J. XU AND L. T. ZIKATANOV, *On an energy minimizing basis in algebraic multigrid methods*, Comput. Vis. Sci., 7 (2004), pp. 121–127.

[111] Y. ZHU AND A. BRANDT, *An efficient multigrid method for the simulation of high resolution elastic solids*, ACM Trans. Graph., 29 (2010), pp. 1–18.

Academic Career

04/2010-06/2013:   PhD student at Fraunhofer Institute for Industrial Mathematics (ITWM), Department Flow and Material Simulation and University of Kaiserslautern, Department of Mathematics, Kaiserslautern (Germany)

10/2011-12/2011:   Special Semester on Multiscale Simulation & Analysis in Energy and the Environment, RICAM, Linz (Austria)

06/2010-09/2010:   Internship at Lawrence Livermore National Laboratory, Livermore (USA)

10/2009-03/2010:   Project Studies in Advanced Technology at Fraunhofer ITWM

10/2004-08/2009:   Master's degree in Mathematics, University of Kaiserslautern

Akademischer Werdegang

04/2010-06/2013:   Promotion am Fraunhofer Institut für Techno- und Wirtschaftsmathematik (ITWM), Abteilung Strömungs- und Materialsimulation und Technische Universität Kaiserslautern, Fachbereich Mathematik

10/2011-12/2011:   Special Semester on Multiscale Simulation & Analysis in Energy and the Environment, RICAM, Linz (Österreich)

06/2010-09/2010:   Forschungsaufenthalt am Lawrence Livermore National Laboratory, Livermore (USA)

10/2009-03/2010:   "Project Studies in Advanced Technology" am Fraunhofer ITWM

10/2004-08/2009:   Diplom in Mathematik an der Technischen Universität Kaiserslautern